SELF-ASSEMBLY, ORGANOGELATION AND PHOTOPHYSICAL PROPERTIES OF C_3-SYMMETRICAL DISCOTIC MOLECULES

THESIS SUBMITTED TO

COCHIN UNIVERSITY OF SCIENCE AND TECHNOLOGY

IN PARTIAL FULFILMENT OF THE REQUIREMENTS FOR THE DEGREE OF

DOCTOR OF PHILOSOPHY IN CHEMISTRY

UNDER THE FACULTY OF SCIENCE

By

SANDEEP A.

Under the Supervision of

Dr. A. Ajayaghosh

Photosciences and Photonics
Chemical Sciences and Technology Division
CSIR–National Institute for Interdisciplinary Science and Technology (CSIR–NIIST)
Thiruvananthapuram-695 019, Kerala

May 2017

Dedicated to

My Family

DECLARATION

I hereby declare that the Ph.D. thesis entitled: "**SELF-ASSEMBLY, ORGANOGELATION AND PHOTOPHYSICAL PROPERTIES OF C_3-SYMMETRICAL DISCOTIC MOLECULES**" is an independent work carried out by me at the Photosciences and Photonics Section, Chemical Sciences and Technology Division of the CSIR-National Institute for Interdisciplinary Science and Technology (CSIR-NIIST), Trivandrum, under the supervision of Dr. A. Ajayaghosh and the same has not been submitted elsewhere for a degree, diploma or title.

In keeping with the general practice of reporting scientific observations, due acknowledgement has been made wherever the work described is based on the findings of other investigators.

(SANDEEP A.)

राष्ट्रीय अंतर्विषयी विज्ञान तथा प्रौद्योगिकी संस्थान
वैज्ञानिक तथा औद्योगिक अनुसंधान परिषद्
इंडस्ट्रियल इस्टेट पी.ओ., पाप्पनंकोड, तिरुवनंतपुरम, भारत–695 019
CSIR-NATIONAL INSTITUTE FOR INTERDISCIPLINARY SCIENCE & TECHNOLOGY (CSIR-NIIST)
Council of Scientific & Industrial Research
Industrial Estate P.O., Pappanamcode, Thiruvananthapuram, India-695 019
डॉ. ए. अजयघोष एफएनए, एफटीडब्ल्यूएस
निदेशक
Dr. A. Ajayaghosh FNA, FTWAS
Director

May 09, 2017

CERTIFICATE

This is to certify that the work embodied in the Ph.D. thesis entitled "**SELF-ASSEMBLY, ORGANOGELATION AND PHOTOPHYSICAL PROPERTIES OF C_3-SYMMETRICAL DISCOTIC MOLECULES**" has been carried out by **Mr. Sandeep A**. under my supervision and guidance at the Photosciences and Photonics, Chemical Sciences and Technology Division of the CSIR-National Institute for Interdisciplinary Science and Technology (CSIR-NIIST), Trivandrum and the same has not been submitted elsewhere for a degree. All the relevant corrections, modifications and recommendations suggested by the audience and the doctoral committee members during the pre-synopsis seminar of **Mr. Sandeep A**. have also been incorporated in the thesis.

(A. Ajayaghosh)

Thesis Supervisor

ACKNOWLEDGEMENTS

I have great pleasure in placing on record my deep sense of gratitude to Dr. A. Ajayaghosh, my thesis supervisor, for suggesting me the research problem and for his guidance, support and encouragement, leading to the successful completion of this work.

I would like to express my sincere thanks to Professor M. V. George for his constant support during the tenure of this work.

I wish to thank Dr. Suresh Das, and Dr. Gangan Prathap, former Directors of CSIR-NIIST, Thiruvananthapuram for providing me the necessary facilities for carrying out the work.

I sincerely thank Dr. K. R. Gopidas, Dr. D. Ramaiah, Dr. J. D. Sudha, Dr. Joshy Joseph, Dr. K. N. Narayanan Unni, Dr. Biswapriya Deb, Dr. V. Karunakaran, Dr. K. Yoosaf, and Dr. C. Vijayakumar, present and former Scientists of the Photosciences and Photonics, for all the help and support extended to me.

I am extremely thankful to Dr. Vakayil K. Praveen, for his help, support, encouragement and care.

I would like to thank Dr. S. Prathapan, Associate Professor, Department of Applied Chemistry, CUSAT, Cochin for his support and help.

My sincere thanks are also due to:

Dr. S. Seki, Osaka University, Japan for photoelectron yield spectroscopy analyses.

Dr. D. S. Shankar Rao and Dr. S. Krishna Prasad, Centre for Nano and Soft Matter Sciences, Banglore for temperature dependent XRD measurements.

I thank all the members of the Photosciences and Photonics and in particular, Dr. Santhosh S. Babu, Dr. S. Mahesh, Dr. S. Sreejith, Dr. S. Srinivasan, Dr. K. P. Divya, Dr. S. Prasanthkumar, Dr. Anesh G., Dr. Krishnan Kartha, Dr. Anees P., Mr. Thirumalai K., Mr. Vishnu S., Mr. Sandeep C., Mr. Vedanarayan B., Mr. Rahul Dev M., Ms. Divya Susan Philips, Mr. Samrat Ghosh, Mr. Arindam Mal, Mr. Hifsudeen M., Mr. Satyajit Das, Mr. Gourab Das, Dr. Rakesh K. M, Dr. Manas Panda and members of other divisions of NIIST for their help

and support. I would like to thank Mr. Robert Philip, Mr. Chandrakanth C. K, Ms. S. Viji, Ms. Soumini Mathew, Mr. Adarsh, Mr. P. Preethanuj, Mr. T. Arun, Mr. Saran P., and Mr. R. Gokul for technical assistance and general help.

A special word of thanks to my friends, Mr. Kiran J. S., Mr. Kiran Mohan, Dr. Hari Shankar, Dr. Anish P. Sivadas, Dr. Sankar Sasidharan, Dr. R. Ramakrishnan, Dr. Manu, Dr. Nandajan P. C., Dr. Biju Francis, Mr. Sudheesh K. V., Mr. Shanmugasundaram M., Mr. Prakash S. P., Mr. Mahesh M., Mr. Manuraj Mohan and Ms. Vijitha I. for their endless love and support.

Words are inadequate to express my gratitude to my parents, brothers and sister-in-laws, who constantly stood as a source of encouragement. I am also indebted and deeply grateful to my wife Mrs. Meenu M. T. for her love and my in-laws for their support. I take this opportunity to pay respect to all my teachers who guided me.

I sincerely thank Council of Scientific and Industrial Research (CSIR), and DST, Government of India for financial assistance.

Sandeep A.

CONTENTS

PREFACE

Molecular self-assembly is one of the most viable approaches to create supramolecular architectures of different size, shape and properties. Among the various molecular systems studied for this purpose, benzene-1,3,5-tricarboxamide (BTA) is one of the widely used C_3-symmetrical systems. The unique feature in the self-assembly process of BTAs is the formation of one-dimensional (1D) columnar mesophase, which transports charge and excitons anisotropically over a considerable distance. The controlled gel formation along with its luminescent properties allows the study of different self-assembly mechanism and its further use in different applications such as chemosensing, organic electronics, etc. The present thesis has been divided into four chapters out of which the first chapter gives an overview of the self-assembly of the molecules that were constructed using BTA core and were recently reported in the literature. In addition, the specific objectives of the present thesis were also briefly described at the end of this chapter.

Synthesis, characterization and photophysical properties of the C_3-symmetrical molecules ***C*$_3$OPV1**, ***C*$_3$OPV2** and ***C*$_3$OPV3** form the subject matter of the second chapter. All the three molecules form self-assembly through an isodesmic pathway with different aggregate stabilities. Out of these molecules, only ***C*$_3$OPV1**, with nine alkyl chains could show the liquid crystalline properties. Upon cooling from isotropic melt, ***C*$_3$OPV1** formed columnar phase with 2-d rectangular lattice and retained the liquid crystalline phase even at room temperature. At lower temperature the conformational stabilization of the peripheral alkyl chains occurs and the three-

fold H-bonding interaction between the adjacent molecules in the column leads to packing of the molecules in such a way that there is an angle of twist between them. As the number of alkyl chains at the periphery decreases, the LC property disappears. When one of the alkyl chains is knocked out from each OPV unit, the total number of alkyl chain decreases to six. ***C*$_3$OPV2**, molecule with alkyl chains at 3,4-positions is able to gelate organic solvents and ***C*$_3$OPV3**, molecule with alkyl chains at 3,5-positions neither forms gel nor show any LC properties. The lack of gelation property of ***C*$_3$OPV1** and ***C*$_3$OPV3** can be rationalized on the basis of their morphology. Gelation is basically the entrapment of solvents inside a three-dimensional (3D) matrix of interconnected network of fibers. Morphological studies revealed that ***C*$_3$OPV2** is capable of forming interconnected network of fibers. However, the other two molecules, i.e., ***C*$_3$OPV1** and ***C*$_3$OPV3** were unable to form 1D assembly. The spherical particles are formed in the case of ***C*$_3$OPV1** and ***C*$_3$OPV3** and could not entrap solvent molecules. Therefore gelation was not observed.

The sensing properties of ***C*$_3$OPV1** and ***C*$_3$OPV2** are discussed in *Part a* of Chapter 3. A fluorescence approach has been described for the sensing of DNT in the vapor phase. For this purpose, two C_3-symmetrical molecule based on oligo(*p*-phenylenevinylene), ***C*$_3$OPV1**, and ***C*$_3$OPV2**, have been utilized. Upon self-assembly, **C$_3$OPV1** and **C$_3$OPV2** form spherical particles and interconnected fibrillar networks, respectively. In the solution state, a very week fluorescence quenching was observed in the presence of TNT for both the molecules. This observation implies that the TNT is not an efficient quencher for ***C*$_3$OPV1** and ***C*$_3$OPV2** in the isotropic solution and hence is not suitable for the detection of TNT. Both the molecules were able to respond

towards the vapors of nitroaromatic compounds by quenching the fluorophore emission. The response of ***C*$_3$OPV2** aggregates towards nitroaromatic analytes such as nitrobenzene (NB), *o*-nitrotoluene (ONT), 2,4,6-trinitrotoluene (TNT), etc. were carried out. All these analytes respond to the ***C*$_3$OPV2** aggregates emission, but with different extent of fluorescence quenching. Among the nitroaromatics tested, nitrobenzene showed fastest fluorescence quenching in which about 49% quenching was observed in first 20 seconds. *o*-Nitrotoluene showed almost 40% fluorescence quenching. Trinitrotoluene (TNT) showed faster response with 24% fluorescence quenching in 20 seconds than dinitrotoluene (DNT) that showed only 16 % quenching. The difference in quenching efficiency of the ***C*$_3$OPV2** towards the vapors of the various aromatic analytes depends on the electron accepting ability and the vapor pressure of the analyte. The morphology also plays an important role in determining the efficiency of fluorescence quenching. Better excited state energy migration is observed in the case of 1D nanofibre over spherical particles. Therefore, ***C*$_3$OPV2**, which forms fiber morphology, shows efficient fluorescence quenching when compared to ***C*$_3$OPV1**, which forms spherical particles.

Part b of Chapter 3 discusses the synthesis, characterization, photophysical and sensing properties of ***C*$_3$PBI**, a perylenebisimide based C_3-symmetrical molecule. The molecule is synthesized by a multistep synthetic strategy and the self-assembly properties have been studied in detail. ***C*$_3$PBI** forms aggregate in toluene and form nanofibers. The entangled nanofibers form a mesh like porous morphology when drop-cast on a surface with bright red fluorescence. This mesh like porous morphology assists the expedient adsorption of amine vapors on its surface. The

electronic property of the molecule in the film state was then measured and the HOMO-LUMO energy levels were calculated. A gap around 2.13 eV was calculated with HOMO at -6.4 eV and LUMO at -4.27 eV. The energy levels of the ***C*$_3$PBI** and aniline (analyte) suggests favorable electron transfer from aniline to the photoexcited ***C*$_3$PBI** and hence the red emission of ***C*$_3$PBI** gets quenched. Depending upon the electron density and the vapor pressure of amines, different amines give different responses.

Detection of different life threatening volatile organic compounds (VOCs) such as carcinogenic molecules is an active area of research. In Chapter 4, we report the use of supercoiled supramolecular polymeric fibers of self-sorted donor–acceptor molecules as "turn-off/turn-on" fluorescent sensors for the detection of carcinogenic VOCs. For this purpose, an oligo(*p*-phenylenevinylene) based C_3-symmetrical donor molecule, ***C*$_3$OPV2**, and a perylenebisimide based acceptor molecule, ***C*$_3$PBI**, have been used. When these two molecules were mixed together in toluene, in contrast to the usual charge transfer (CT) stacking, supramolecular fibers of self-sorted stacks were formed at the molecular level, primarily driven by their distinct self-assembly pathways. However, CT interaction at the macroscopic level allows these fibers to bundle together to form supercoiled ropes. An interfacial photoinduced electron transfer process from the donor to the acceptor fibers leads to an initial fluorescence quenching, which could be reactivated by exposure to strong donor or acceptor type VOCs to regenerate the respective fluorescence of the individual molecular stacks. Thus, strong donors could regenerate the green fluorescence of ***C*$_3$OPV2** stacks and strong acceptors could reactivate the red fluorescence of ***C*$_3$PBI** stacks. These supercoiled supramolecular ropes of self-sorted donor–acceptor stacks provide a

simple tool for the detection of donor- or acceptor-type VOCs of biological relevance, using a “turn-off/turn-on” fluorescence mechanism as demonstrated by the sensing of *o*-toluidine, which has been reported as a lung cancer marker.

In summary, this thesis describes the design, synthesis and properties of a few C_3-symmetrical systems. The self-assembly, co-assembly and photophysical properties of these C_3-symmetrical systems and their applications in sensing of volatile organic compounds are investigated and discussed.

Chapter 1

Benzene-1,3,5-Tricarboxamide Based C_3-Symmetric Systems: Self-Assembly, Properties and Applications

1.1. Abstract

Molecular self-assembly is one of the most viable approaches to create supramolecular architectures of different size, shape and properties. Among the various molecular systems studied for this purpose, benzene-1,3,5-tricarboxamide (BTA) is one of the widely used C_3-symmetrical systems. The unique feature in the self-assembly process of BTAs is the formation of one-dimensional (1D) columnar mesophase, which transports charge and excitons anisotropically over a considerable distance. The 1D self-assembly of BTAs is stabilized by three-fold H-bonding that mostly results in the formation of nanometer sized rod-like or fiber-like structures. The controlled gel formation along with luminescent properties allows the study of different self-assembly mechanism and its further use in different applications such as chemosensing, organic electronics, etc. This chapter summarizes the study on a range of supramolecules that were constructed using BTA core and were recently reported in the literature. In the last part of this chapter, the origin, objective, scope and the approach of the present thesis is discussed.

1.2. Introduction

The recent advancement of supramolecular chemistry has brought-up numerous ordered superstructures with tunable property that have great applications in switching materials, sensors and optoelectronic devices.[1] Driven by non-covalent interactions, the spontaneous self-organization of small molecules to supramolecules to macroscopic soft materials with well-defined morphological features has been a topic of prime interest in the area of chemistry, biology, and material science.[2-4] Several types of noncovalent interactions such as ion-ion, ion-dipole, dipole-dipole, H-bonding, π-π stacking, cation-π, anion-π and van der Waals forces, can be used to build these superstructures. One can achieve these supramolecular superstructures by judicious design of small molecules with specific functionalities that are capable of building intermolecular interactions in different dimensions. These superstructures have enormous importance in the area of material science, specifically in the area of optoelectronics and sensory materials.[1,5] For example, in the case of organic electronic devices, the π-π stacking of the molecules has to be optimal for the efficient charge transport along the supramolecular stacks.[6]

Different examples of supramolecular assemblies such as micelles, colloids, dendrimers, liposomes, gels and liquid crystals have been reported in the literature. Among these soft materials, liquid crystals and supramolecular gels are gaining increasing attention from the fundamental as well as technological viewpoints. Liquid crystal is a state of matter that has properties in between conventional liquid materials and solid crystals. As a result, a liquid crystal may flow like a liquid despite its molecules are oriented in a crystal-like manner. This unique combination

of molecular order and material fluidity in a single entity has opened up a broad range of applications in optoelectronics, especially in display technology. A schematic representation of molecular arrangement in the crystalline solids, liquids and liquid crystals are given below (Figure 1.1). The fundamental requirement for any organic molecule to exhibit liquid crystalline mesophase is shape anisotropy.[7,8] A typical molecule exhibiting liquid crystalline phases generally contains a rigid central core, which is usually an aromatic moiety functionalized with flexible groups such as alkyl chains at the periphery.

FIGURE 1.1. Schematic representations of molecular arrangements in solids, liquid crystals and liquids.

Liquid crystalline phases share some of the properties of isotropic liquids and anisotropic crystalline solids. Although the molecules in this phase exhibit some positional and orientational order, they also behave as fluids. Owing to their dynamic nature, photochemically, thermally or mechanically induced structural changes of liquid crystals can be used for the construction of stimuli-responsive multifunctional materials.[9]

Molecular order is one of the most important parameters that governs the performance of organic semiconductors in devices.[6a,10] Accordingly, liquid crystals can potentially be used for electron, hole, ion, molecular transporting, sensory, optical and bioactive materials.[10] They can also act as tunable solvents for the dispersion of nanomaterials.[11] Being an anisotropic media, liquid crystals provide a very good support for the self-assembly of nanomaterials into larger organized structures in multiple dimensions.[12]

Supramolecular gels on the other hand are soft materials formed by a low molecular weight organic compound usually by the formation of three-dimensional (3D) networks of entangled supramolecular fibers in which a large volume of solvents are trapped by capillary action.[13,14] Most of the earlier reports on supramolecular gelators are serendipitous. However, the continued effort over the years have helped chemist to have a better understanding of the requirements of gelator design. The following features are important in the design of new organogelators: (i) formation of 1D aggregates via an anisotropic growth process, (ii) intertwining of these 1D aggregates to form a 3D network-like structures, and (iii) the prevention of crystallization or precipitation of the self-assembled aggregates through a delicate balance between order and disorder (Figure 1.2).[15] Supramolecular gels have been used for a variety of applications, which include the use of gels as a scaffold for excitation energy transfer, as templates for aligning metal nanoparticles and for the generation of conducting nanowires and ribbons.[16,17] Conducting nanowires prepared by gelation of organic molecules are potential candidates for organic electronics.[18] Moreover, conducting gels can be utilized as

actuators and capacitors.[19-21] Molecular π-gelators were used as active materials in organic field effect transistors (OFETs).[18] Some of the molecules show changes in the photophysical properties such as fluorescence during gelation and these properties can be used for imaging and sensing of various types of analytes such as anions, metal ions, explosives, volatile organic compounds, etc.[22-25]

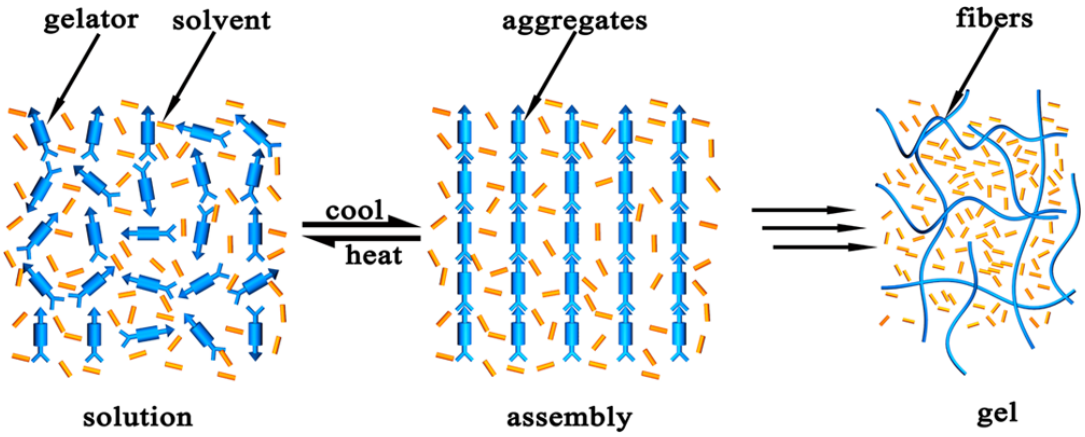

FIGURE 1.2. Schematic representation of the self-assembly of low molecular weight gelators into 1D aggregates and the subsequent formation of a 3D entangled network. (Adapted with permission from ref. 15. Copyright 2014 American Chemical Society.)

The organic chromophore that could form gel in organic solvents and having thermotropic mesomorphic behavior are gaining much attention in recent years, because they can combine the properties of liquid crystals such as molecular order with that of 3D fibrillar network formation. To achieve a gel/mesomorphic state, a balance is required between the tendency of the molecules to dissolve/melt and to aggregate. The shape of the molecule has also been found to have an important role on the formation of liquid crystalline gelators. It is rather difficult to find a rod shaped molecule that forms organogels exhibiting thermotropic mesomorphic

behavior, whereas this could be achieved with some wedge-shaped or disc shaped molecules.

1.3. Benzene-1,3,5-Tricarboxamides

Benzene-1,3,5-tricarboxamides (BTAs) have attracted considerable attention owing to their capability to form multiple H-bonded assemblies through three amide groups.[26] Under appropriate experimental conditions, 1D growth of the monomers into H-bonded supramolecular polymers is achieved. Various studies have been conducted to unravel the mechanism of the self-assembly behavior, and the origin of the cooperativity in these systems. These studies have contributed enormously towards the rational design of BTA derivatives for the preparation of self-assembled functional materials with desired properties. In certain cases, BTA derivatives with core benzene ring exhibited liquid crystalline property, which are more commonly known as discotic mesogens. In 1988, Matsunaga and co-workers synthesized the first BTA based discotic mesogen comprising of linear alkyl side chains (*n*-hexyl and higher homologues) that displayed thermotropic liquid crystalline behavior over a broad temperature range.[27]

1.3.1. Design and Synthesis of BTAs

BTA molecule consists of a benzene ring in which the amide functional groups are present at 1, 3 and 5th positions. The amide group can be attached to the benzene ring either via the carbonyl group yielding C=O centered (**1**) or through the nitrogen atom yielding *N*-centered (**2**) BTA (Chart 1.1). The substituents on amide groups of the BTA can be aromatic or aliphatic groups. If the groups attached to the benzene

ring are identical, then the molecule will have C_3 symmetry. Unsymmetrical BTAs are also possible if any one of the three substituents on the amide groups is different.

In 1915, Curtius and co-workers first reported the synthesis of BTA molecule using benzene-1,3,5-tricarboxylic acid as the starting material.[28] The triphenyl substituted BTA, **3** (Chart 1.1) was prepared by treating aniline with benzene-1,3,5-tricarbonyl azide that were obtained from the corresponding tri-ester derivative. However, because of the explosive nature of the triazide derivative, it was not possible to prepare large-scale quantity of BTA's by this procedure.

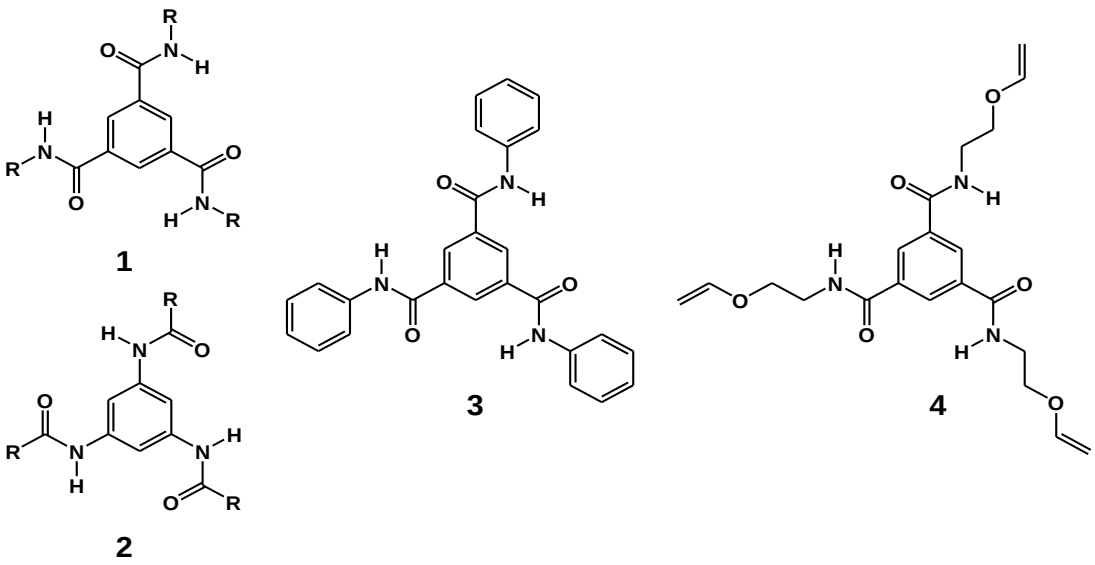

CHART 1.1. General chemical structures of C=O (**1**) and *N*-centered (**2**) BTA molecules (where R can be aliphatic or aromatic), the chemical structures of **3** and **4** are also given.

Later in 1954, Rohm and Haas reported a facile route for the preparation of *tris*(vinyloxyethyl) BTA analogue, **4**, (Chart 1.1) starting from trimethyl benzene-1,3,5-tricarboxylate and 2-vinyloxyethylamine.[29] The requirement of high reaction temperature and rather long reaction time is the main drawback of this method. In fact, in order to prepare C=O centered BTA, the most accepted synthetic strategy is

the reaction of benzene-1,3,5-tricarbonyl trichloride with the corresponding amine in presence of a base.[30] However, direct functionalization of benzene-1,3,5-tricarboxylic acid with the appropriate amine by using suitable coupling agents is also frequently applied. The crystal structure of simple BTA derivatives revealed the formation of helical supramolecular columnar structures in the solid state as a result of the threefold H-bonding between the amides of consecutive discs (Figure 1.3).

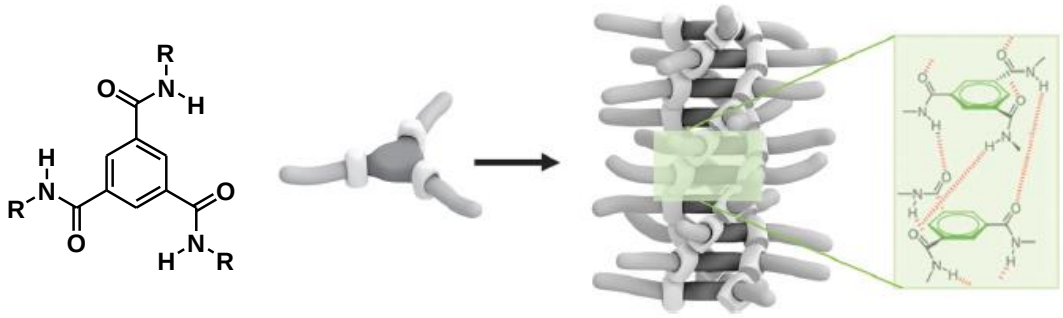

FIGURE 1.3. Schematic representation of benzene-1,3,5-tricarboxamide self-assembly into helical 1D aggregates, which are stabilized by threefold intermolecular H-bonding, where R can be aliphatic or aromatic. (Adapted with permission from ref. 26. Copyright 2012 The Royal Society of Chemistry.)

BTA molecules with R-groups such as alkyl,[27,31] phenyl,[32-34] pyridyl,[35] bipyridyl,[36,37] porphyrinyl,[38] triphenylyl,[39] oligo(*p*-phenylenevinylene),[40] amino acid,[41-46] dipeptide,[47] oligo(peptide),[48] oligo(ethyleneoxy),[49,50] and benzocrown ethers[51] have been prepared. These derivatives have been utilized in various applications ranging from organogels,[52] hydrogels,[33,51,53] liquid crystals,[27] nanostructured materials,[54] magnetic resonance imaging (MRI) contrast reagents,[55] nucleating agents for polymers,[56] metal complexation reagents,[54] and microcapsules for drug delivery.[57] The potential application of the BTA derivatives are decided by the nature of the side chains attached to it. For example, high melting crystalline

solids, which crystallize as fiber-like needles were prepared from BTAs comprising bulky, aliphatic side chains. These unique feature make BTAs an effective nucleating agents for isotactic polypropylene (Figure 1.4a).[56,58] In contrast, long alkyl side chains induce thermotropic liquid crystalline behavior (Figure 1.4b)[30,59] and branched alkyl side chains facilitate organogel behavior (Figure 1.4c).[52] Compatibility with water was achieved by introducing charged Gd(III) complexes at the periphery,[43] or ethyleneoxide based side chains[50] or acidic groups.[33,41] While BTAs are stable, also under aqueous conditions, the introduction of water-labile groups leads to the formation of microcapsules that hydrolyze over time with slow release of encapsulated molecules into the surrounding medium (Figure 1.4e).[57]

Fluorescent BTAs can be synthesized by attaching π-conjugated moieties to the core benzene unit.[37,40,60] Interestingly, the introduction of chiral, non-racemic and soluble alkyl side chains leads to the formation of 1D aggregates with a preferred helical sense.[61] This has allowed characterization of the aggregation properties and the mechanism of aggregation by using sensitive spectroscopic techniques such as circular dichroism (CD).

1.4. Self-Assembly of BTAs

1.4.1. In Solution State

Because of the facile synthetic feasibility of BTA derivatives, large varieties of BTA derivatives with different substituents have been synthesized and detailed studies on their intermolecular association properties have been carried out in the solution state. As a result, the BTA molecules are evolved as perfect systems for understanding the

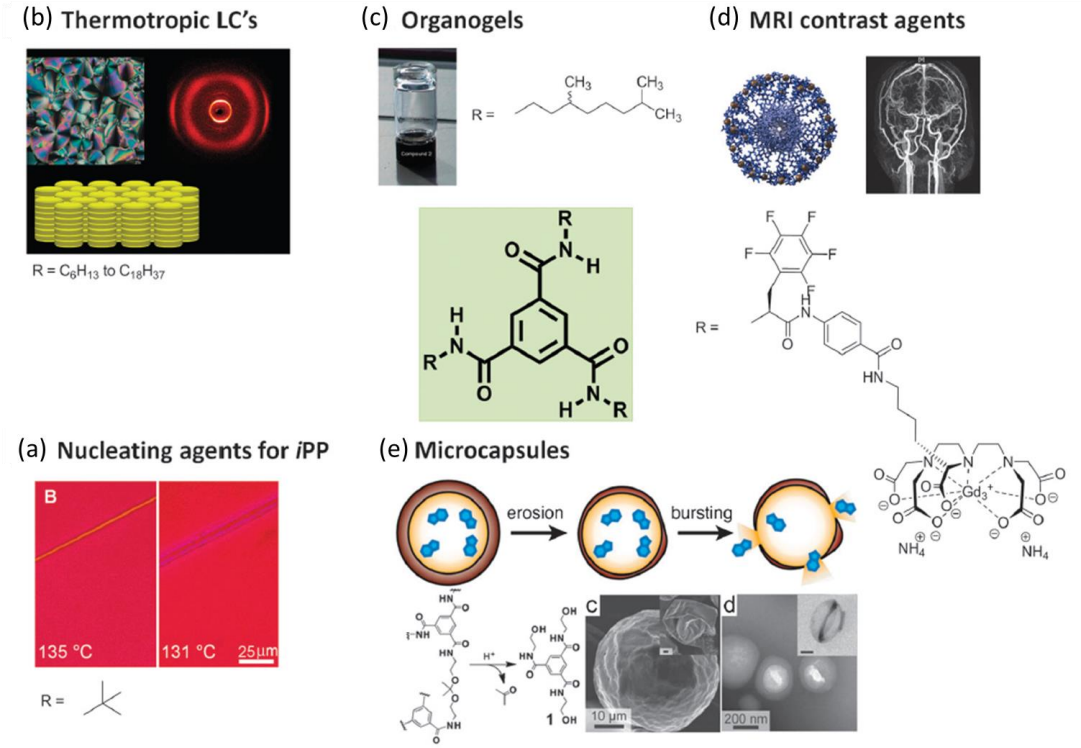

FIGURE 1.4. An overview of the application areas for BTAs. Different side chains attached to the BTAs result in different applications. (Adapted with permission from ref. 26. Copyright 2012 The Royal Society of Chemistry.)

effect of structural variations and the impact of solvents on the self-association process.[62] The parent BTA compound with C=O centered amide bond possessing both chiral and achiral aliphatic side chains has been studied by various spectroscopic techniques in dilute apolar and alkane solvents. Based on the reported crystal structure, it is expected that BTA with C=O centered amide bond will self-assemble via threefold H-bonding interactions into helical 1D assemblies.[63] The helical nature of the BTA aggregates were confirmed by the observation of strong Cotton effect, centered around 220 nm. The CD studies carried out on BTA molecule by introducing a chiral center into the alkyl side chain revealed that the

chiral methyl group in the alkyl chain prefers one helical confirmation over the other.[64-66] However, when deuterium/hydrogen substitution was used as the source of chirality, diastereomerically related right- and left-handed helical aggregates with small energy difference were observed.[66] In order to understand the correlation between the reported crystal structure and the corresponding structure of the helical aggregates formed in apolar solution, a detailed vibrational circular dichroism (VCD) studies and molecular calculations of BTA(*R*)-**6** were carried (Chart 1.2).[67] This correlation confirms that there is a nonzero twist angle between the amide plane and the benzene plane for the monomers present in the helical assembly. The complete disassembly of the helical aggregate was observed in presence of a competing solvents such as acetonitrile because the major noncovalent interaction between the monomers in the aggregates is the intermolecular H-bonding.[68] This is then further confirmed by substituting a competing side chain on the BTA that can form intramolecular H-bonding with the amide groups as in the case of BTA**7** (Chart 1.2).

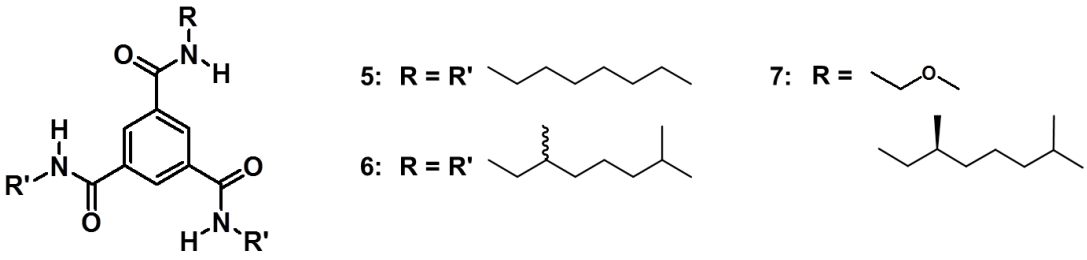

CHART 1.2. Structure of the molecules **5-7**.

It is well established that the temperature dependent UV-Vis absorption and CD spectroscopy are the most efficient method to probe the self-assembly mechanism. Therefore, these techniques are widely used for understanding the

mechanism of BTA self-assembly. Meijer *et al*., have used two C=O centered BTA molecules **5** and (*R*)-**6** (Chart 1.2) in *n*-heptane for explaining the mechanistic aspects of BTA self-assembly. CD studies reveal that BTA molecules do not show Cotton effect at high temperatures (> 360 K). This observation indicates that the molecules exist in the molecularly dissolved state at high temperatures. CD spectroscopy at lower temperatures showed the evolution of Cotton effect, reflecting the formation of helical aggregates. At the same time, UV-Vis absorption showed a concomitant hypsochromic shift of the absorption maximum indicating the formation of H-type aggregates. By monitoring the variation in absorbance at a particular wavelength as a function of temperature gives more information about the mechanism by which the assembly was formed. The normalized UV-Vis absorption at a single wavelength with a strong non-sigmoidal shape and a clear elongation temperature reflect the cooperative nature of the self-assembly. If the normalized UV-Vis absorption at a single wavelength follows a sigmoidal shape the self-assembly will be isodesmic nature.[69] Generally, most of the reported simple BTA derivatives follow a cooperative mechanism for the formation of helical self-assembly (Figure 1.5).

The cooperativity arises from a combination of long-range dipole-dipole interaction and short range polarization effect as a result of H-bonding.[70] The dipole-dipole interaction between individual BTA molecules in the helical aggregate is the result of a parallel orientation of the three amide groups along the columnar structure, resulting in a large macro-dipole along the supramolecular polymer.[71] The

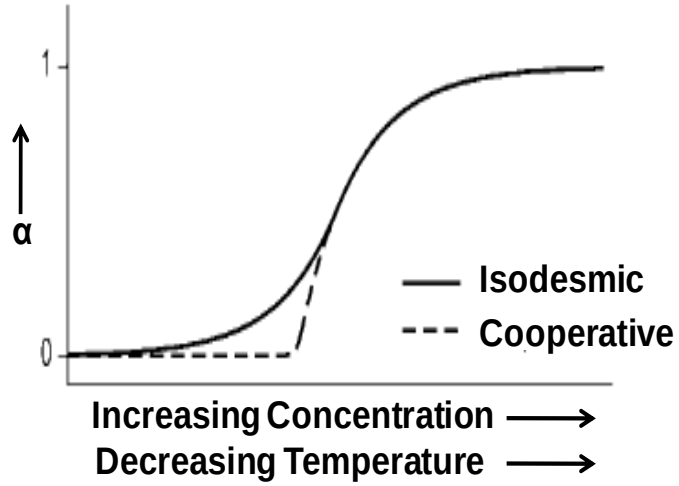

FIGURE 1.5. Schematic representation of the degree of aggregation (α) versus concentration and temperature for an isodesmic and a cooperative self-assembly mechanism. (Adapted with permission from ref. 69. Copyright 2010 WILEY-VCH.)

detailed mechanism of self-assembly of BTA molecule was studied by Meijer and coworkers. All the thermodynamic parameters were calculated by using the nucleation-elongation model.[72]

The Influence of amide H-bonding on aggregate stability and amplification of chirality in BTA derivatives have been studied by Meijer and coworkers. For this purpose, they have designed and synthesized a series of C=O centered and *N*-centered BTAs (Figure 1.6a). Detailed studies revealed that comparing to the C=O centered BTAs, the *N*-centered BTAs form weaker assemblies. Chiral amplification is observed in both cases but with a less pronounced effect in the case of *N*-centered BTAs. Since the rotation around the phenyl-NH bond has higher energy penalty when compared to the phenyl-C=O bond of the monomer, unfavorable deformation of the *N*-BTA is required upon its addition to a growing supramolecular polymer. This effect reduces the dipole moment and weakens the intermolecular H-bonding in

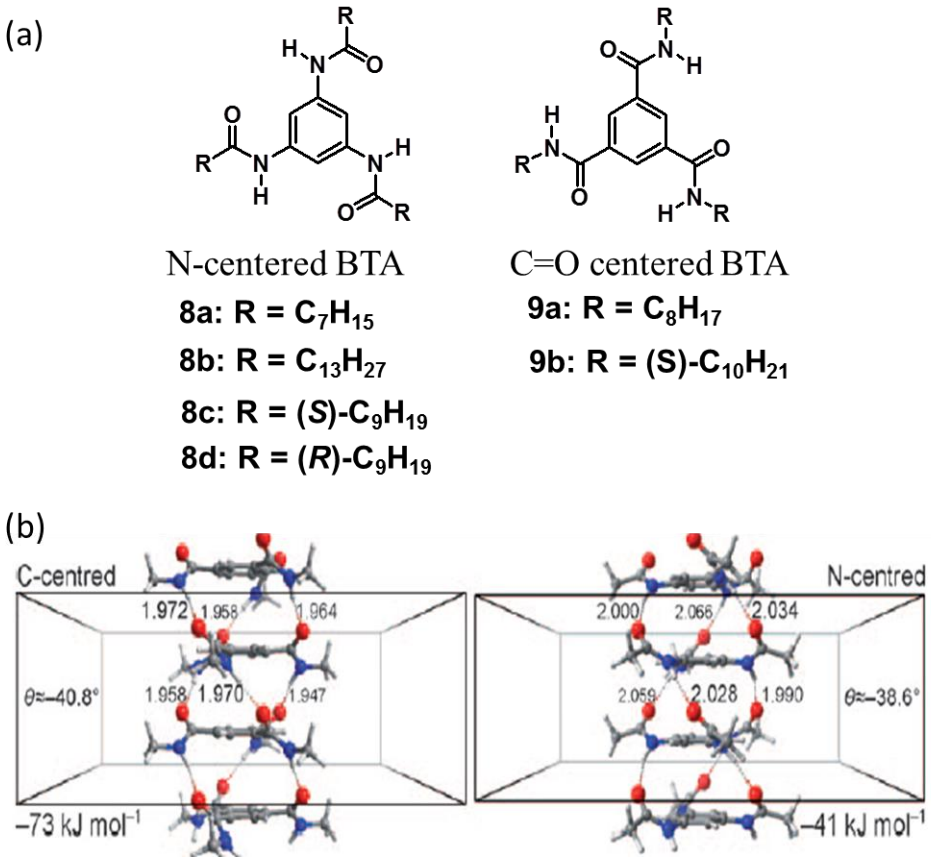

FIGURE 1.6. (a) Chemical structure of molecules **8** and **9** (b) PW-DFT (Plane Wave – DFT) optimized structures and N-H···O H-bond lengths (Å) of infinite chains of C=O centered BTA and *N*-centered BTA. Energy values presented correspond to the average interaction energy (ΔE) between the monomers in the respective supramolecular ensemble. (Adapted with permission from ref. 31. Copyright 2010 WILEY-VCH.)

the supramolecular polymer, which, in fact, results in less favorable polymerization process and rationalize the decreased stability of *N*-BTA aggregates with respect to aggregates of C=O BTAs. The average interaction energies of both the systems are also calculated and shown in Figure 1.6b.[31]

The influence of H-bonding interactions on the self-assembling properties was studied using C_3-symmetrical oligo(*p*-phenylenevinylene) derivatives, **10** and **11** (Figure 1.7a).[40] The two derivatives differ only in topology of the amide moieties.

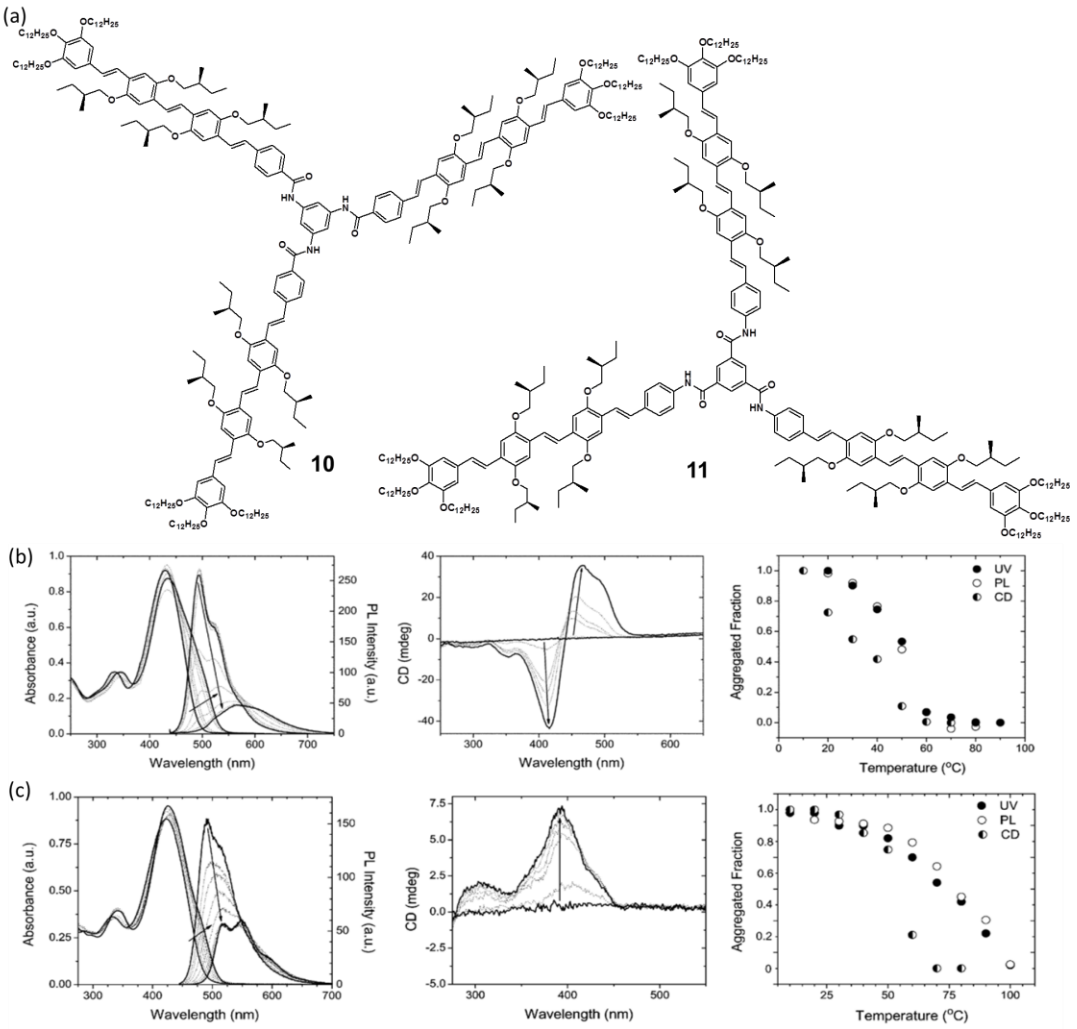

FIGURE 1.7. (a) Molecular structure of **10** and **11**. Temperature dependent UV-Vis absorption and photoluminescence, PL (left), CD (middle) spectra and the melting curves (right) of (b) **10** and (c) **11** in methyl cyclohexane (5.3×10^{-6} M). The aggregated fraction (φ) was determined by using the intensity of the UV-Vis absorption signal at 520 nm (for **10**) and 490 nm (for **11**), the PL signal at 494 nm (for **10**) and 500 nm (for **11**) and the CD signal at 416 (for **10**) and 400 (for **11**) nm and normalizing these intensities at 10 to 1 °C, and at 90 to 0 °C. (Adapted with permission from ref. 40. Copyright 2006 The Royal Society of Chemistry.)

It was observed that the helical aggregates of **10** and **11** are formed through two-step process; first, non-helical stacks are formed, which subsequently rearranges into a

helical conformation. Interestingly, the topology of the amide group was found to have a significant role in determining the stability and helicity of the fibers in solution and the length of the fibrils on a surface. CD measurements of methyl cyclohexane solution of **10** exhibited a bisignate CD curve with positive Cotton effect indicating a right handed helical conformation of constituent molecules within the aggregates, whereas **11** exhibited only a small positive cotton effect, indicating the presence of only non-helical stacks (Figure 1.7b and c). The variable temperature absorption and emission changes are also useful to understand the self-assembly mechanism. These studies illustrate the effect of the subtle difference like an amide sequence alternation on the self-assembly behavior.

The small differences in the balance between secondary interactions arising from BTA unit and the groups attached to it have a strong influence on the order within the supramolecular stack.[47] Compounds containing two phenylalanine motifs **12b** and **12d** (Chart 1.3) are neither soluble in chloroform nor in *n*-heptane even at a micromolar concentration range. The compounds **12c** and **12e** (Chart 1.3), both containing two phenylalanines with opposite chirality, found soluble in chloroform and not in *n*-heptane. The compounds **13a** and **13b** (Chart 1.3) containing glycine at the *C*-terminus of the dipeptide fragment, are easily soluble in both chloroform and *n*-heptane. The molecules **13b**, **12a**, **12c**, and **12e** (Chart 1.3) formed aggregates and failed to reach the molecularly dissolved state even at 50 °C in chloroform. Detailed studies revealed that depending on the strength of the interaction between the different moieties, there is a competition for the noncovalent interaction between the center of the discotics and the dipeptide fragments.

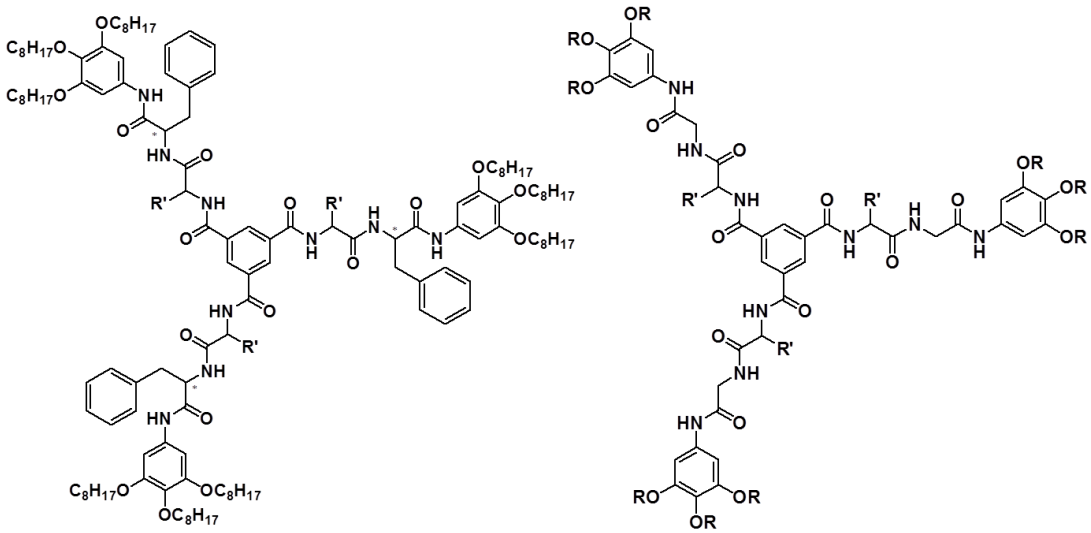

12a: * = L, R' = H

12b: * = L, R' = CH_2-Ph(L)

12c: * = L, R' = CH_2-Ph(D)

12d: * = D, R' = CH_2-Ph(D)

12e: * = D, R' = CH_2-Ph(L)

13a: R' = H, R =

13b: R' = CH_2-Ph(L), R =

CHART 1.3. The chemical structures of the peptide appended BTA molecules.

In a recent report, highly ordered infinite bilayer crystalline structures have been constructed from 3-pyridylamine appended BTA.[35] The intermolecular H-bonding between the pyridyl -*N* and the amide –NHs of the adjacent molecules provide the basis of the macromolecular organization in a rosette manner. The C_3-symmetry of the molecule allows the creation of an infinite two-dimensional (2D) honeycomb grid-like structure with repeating units at 13.87 Å in six directions and with a thickness of approximately 8.40 Å.

C_3-symmetric peptide conjugates that self-assemble into viral-sized peptide nanospheres was first reported using BTA by Kimizuka and co-workers.[48] In this case, the trigonal-$(FKFE)_2$ was prepared by coupling of thiol groups of

CFKFEFKFE peptides with C_3-symmetric iodoacetamidated core molecule **14** (Figure 1.8a). In this case, an induced CD is observed for the core BTA unit in addition to the CD signal corresponding to the β-sheet structures (Figure 1.8b). The sharp peaks shown in the Fourier transform-infrared (FT-IR) spectrum (Figure 1.8c) are characteristic of antiparallel β-sheet structures. This observation indicates that trigonal-$(FKFE)_2$ assists H-bonding mediated intermolecular assemblies, as it is not possible for a single trigonal-$(FKFE)_2$ molecule to form β-sheets in an antiparallel manner.

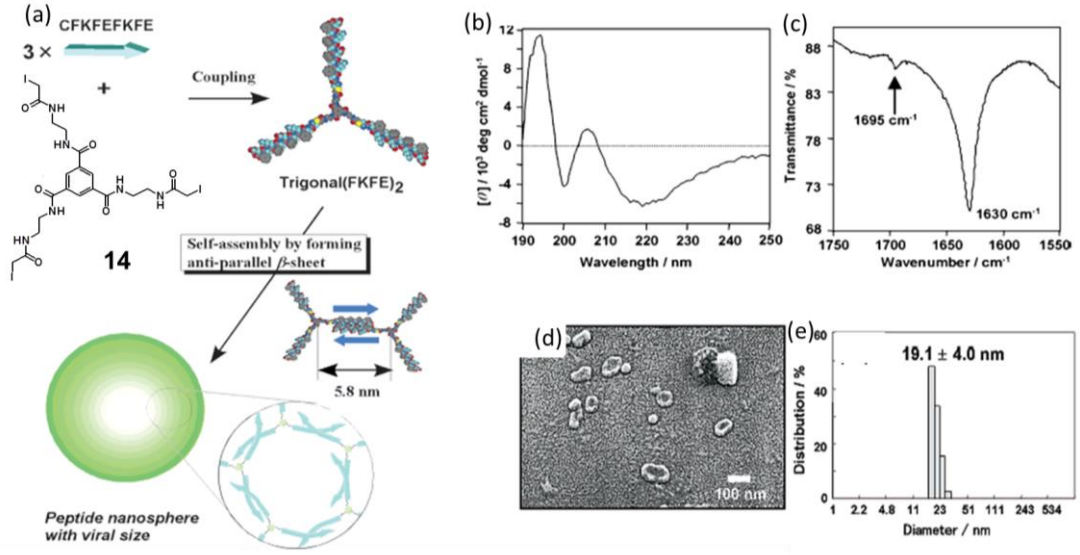

FIGURE 1.8. (a) Synthesis of a C_3-symmetric β-sheet peptide conjugate, **14** and schematic illustration of the self-assembly, (b) CD spectrum of trigonal-$(FKFE)_2$ (24 μM) in aqueous HCl solution (pH 3.3) at 25 °C and (c) FT-IR spectrum of trigonal-$(FKFE)_2$ cast from the acidic aqueous dispersion (24 μM, pH 3.3). (d) SEM image of trigonal-$(FKFE)_2$. (e) Size-distribution obtained from DLS of trigonal-$(FKFE)_2$ in aqueous HCl (pH 3.3). (Adapted with permission from ref. 48. Copyright 2005 American Chemical Society.)

The three armed trigonal-$(FKFE)_2$ molecules self-assemble to form finite set of closed aggregates which resembles a soccer ball. Scanning electron microscopy

(SEM) of the trigonal-$(FKFE)_2$ also showed the presence of spherical nanostructures (Figure 1.8d). The average diameter of nanospheres was determined by dynamic light scattering (DLS) and was found as 19.1±4.0 nm (Figure 1.8e). This C_3-symmetric peptide can be chemically modified with suitable functional groups and can foresee their applications in many fields such as gene carriers and nanosized reactors.

The subtle differences in the ionic character of the C_3-symmetric discotic amphiphiles are useful to control the size, shape and stability of columnar assemblies in aqueous environments by functionalizing the BTA moiety with a fluorinated L-phenylalanine having an aminobenzoate spacer. This approach creates a hydrophobic pocket in the core of the discotic moiety to shield the triple H-bonding motif (Figure 1.9a).[43] A hydrophilic metal chelating moiety is also introduced at the periphery. These modifications significantly increased the stability of the assemblies via additional H-bonding, π-π interactions, and solvophobic effects. Moreover, the presence of metal complex found to increase the scattering power of the aggregates. From the small angle X-ray scattering (SAXS) profile it is found that the discotic **15a** forms rod-like objects (Figure 1.9b). The aggregates are non-interacting cylinders with radius of 3.1 nm and length of around 25-75 nm with increasing concentration upto 1 mM. In contrast, the molecule **17a** formed spherical objects with radius around 3.2 nm (Figure 1.9c).

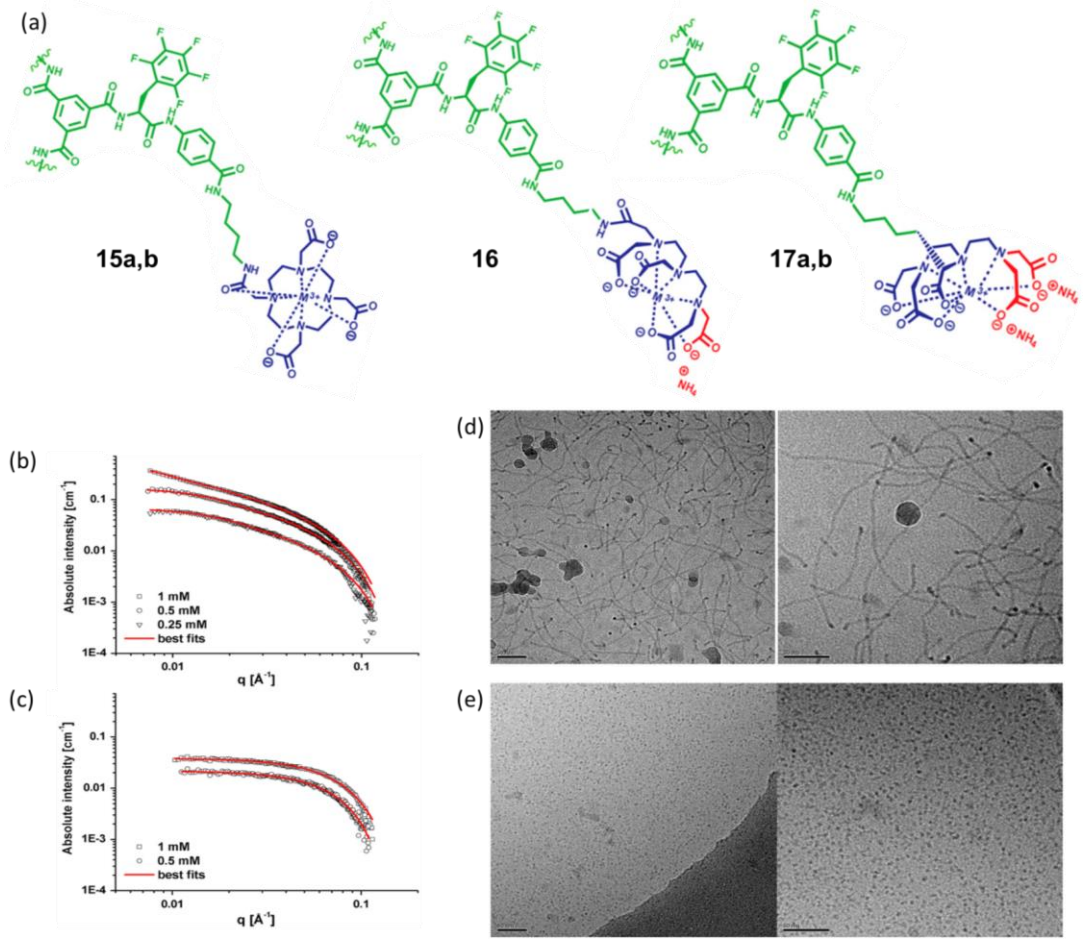

FIGURE 1.9. (a) Structures of the fluorinated discotic amphiphiles: [for paramagnetic discotics **15a**, **16**, and **17a** M(III) = Gd(III); for diamagnetic discotic **15b** and **17b** M(III) = Y(III)]. (b) and (c) SAXS profiles for the fluorinated discotics **15a** and **17a** respectively in citrate buffer (100 mM, pH 6). Cryo-TEM micrographs for self-assembled discotic amphiphile (d) **15a** (0.66 mM) and (e) **17a** (1 mM) vitrified at 288 K in citrate buffer (100 mM, pH 6); scale bar represents 50 nm. (Adapted with permission from ref. 43. Copyright 2010 Proceedings of the National Academy of Sciences (PNAS).

The corresponding cryo-transmission electron microscopy (TEM) images are shown in Figure 1.9d and Figure 1.9e, respectively. Along the same line, the BTA-amino acid based zinc complexes are also reported by Gelinsky *et al.*[44] In another study, Narayanan *et al* reported the BTA anchored naphthalene diimide system that self-

assembled in nonpolar solvents to form helically coiled nanofibers via an isodesmic pathway.[73]

1.4.2. Liquid Crystals

1.4.2.1. Discotic Liquid Crystals and Its Significance

Self-organization of disc-like molecules provides an entirely new class of liquid crystals, quite different from the classical liquid crystals formed by rod-like molecules. The disk-like molecules spontaneously self-assemble into 1D stack, which in turn self-organize on various 2D lattices. Mesophases formed by disk-shaped molecules are primarily of four types: (i) nematic, (ii) smectic, (iii) columnar, and (iv) cubic. The columnar phase is the most common phase in discotics followed by the nematic phase. The other two phases are rarely observed. These mesophases can be experimentally characterized by the combined use of optical polarizing microscope (OPM), differential scanning calorimetry (DSC) and variable temperature X-ray diffraction (XRD) techniques. Each mesophases exhibit characteristic birefringence pattern/texture with characteristic XRD pattern having different *d*-spacing ratios. After the discovery of first discotic mesogen, the most efforts have been made to understand the structural parameters required for a molecule to form the discotic mesophase and their transition temperatures. It is now well understood that the molecule with a central discotic core substituted with 3-12 saturated chains of three or more carbon atoms can form the discotic mesophase. These materials often have two-, three-, four-, or six-fold rotational symmetry. Benzene is the first discotic core and its hexa-esters synthesized by Chandrasekar *et*

al., are the first discotic liquid crystalline materials discovered.[74] Subsequently, a large variety of benzene derivatives have been designed and synthesized.[75] Studies have been carried out to comprehend the mesomorphism and chemical structure-physical property relationships.

Discotic liquid crystals typically consist of a flat, rigid aromatic core decorated with flexible aliphatic chains. The flexible alkyl chains are attached either directly or through specific linker units to the aromatic cores (Figure 1.10). So far a large number of organic cores suitably substituted with flexible alkyl chains exhibiting discotic liquid crystalline phases have been reported. Some of the commonly used cores are shown below (Chart 1.4). The nano-phase segregation between the flexible alkyl chains and the rigid aromatic cores of the discotic molecules is usually the main driving force for inducing liquid crystallinity to these types of molecular architectures.

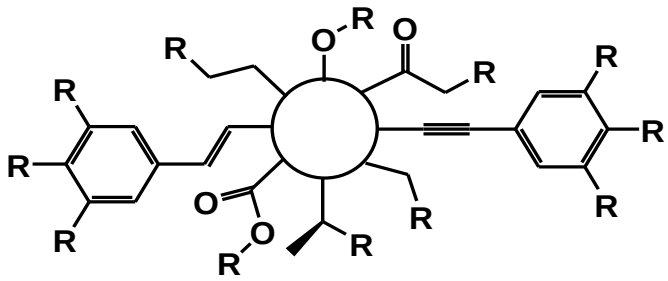

FIGURE 1.10. General structural templates for discotic liquid crystals, where, R is any flexible aliphatic chain.

The liquid crystallinity in BTAs has been found useful for a number of applications in advanced materials. The electrical properties of alkyl substituted BTA molecules are extensively studied by the research group of Tasaka.[76] The ferroelectric properties of alkyl substituted BTA were reported by Sijbesma and co-

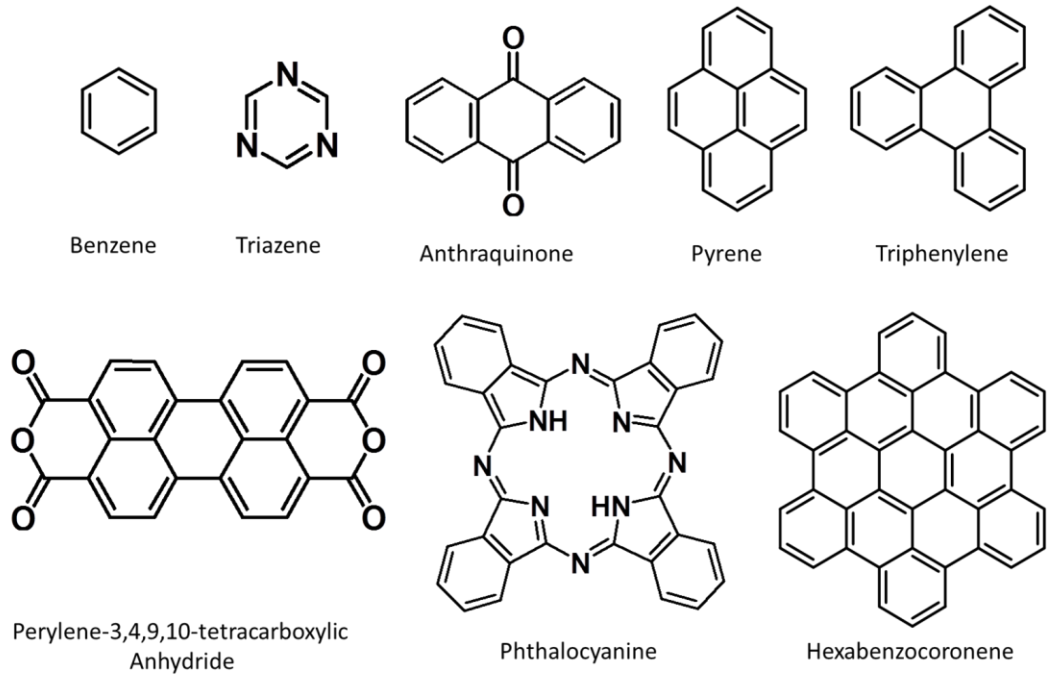

CHART 1.4. Molecular structures of commonly used aromatic cores for preparing discotic liquid crystals.

workers.[77] These studies demonstrate that ferroelectric columnar liquid crystalline phases having stable, switchable polarization along the column axis can be used in ultrahigh density memory devices in which a single column functions as the memory element through manipulation of its macroscopic polarization.[77] The crystallization of the alkyl chains at the periphery of the column induces the polar order in the liquid crystalline phase yielding high surface potential in thin film state (Figure 1.11). In the liquid crystalline phase, the crystallization of the alkyl chains of the molecule **18** freezes the polar order of the macrodipoles. In addition, the basic columnar order and the alignment are unaffected by the crystallization of the alkyl chains. The polarization (*P*) was plotted as a function of the applied electric field (*E*). The loop showed clear hysteresis and a concave shape, indicating the clear ferroelectric behavior (Figure 1.11d). The optical microscopic studies of the films of

the molecule **18** showed the aligned and the non-aligned areas (Figure 1.11b, c and f) and the surface potential was measured by the scanning Kelvin probe microscopy (SKPM) (Figure 1.11g).

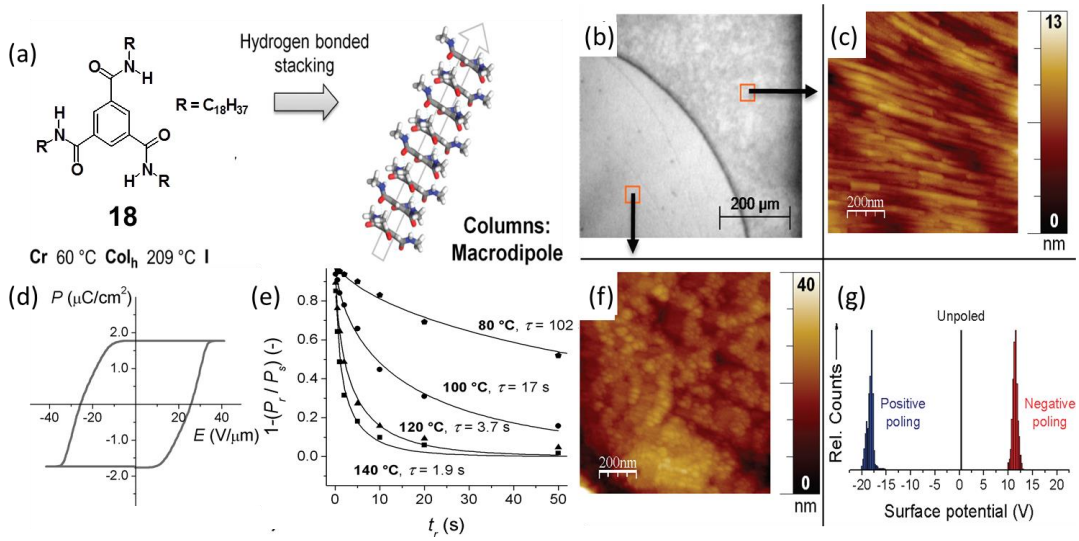

FIGURE 1.11. (a) Structure of BTA molecule **18**. (b) Optical microscopy image showing the difference between aligned (bottom left) and unaligned (top right) sample areas. The red squares indicate the approximate positions at which the atomic force microscopy (AFM) images in c and f were made. (c) AFM height image of an unaligned thin film. (d) Typical *P-E* hysteresis loop for **18** (100 °C, 0.5 Hz). (e) Normalized remaining polarization 1 - (P_r/P_s) as a function of time (t_r). The lines are stretched exponential fits to the data. (f) AFM height image of an aligned thin film. (g) Histogram of typical surface potentials observed by SKPM for positively poled, negatively poled, and unpoled thin films. (Adapted with permission from ref. 77. Copyright 2010 American Chemical Society.)

Meijer and coworkers have reported a new class of discotic liquid crystals based on 2,2'-bipyridine-3,3'-diamine connected to BTA unit, **19a-c** (Figure 1.12a).[36] The intramolecular H-bond, forces the 3,3'-di(carbonylamino)-2,2'-bipyridine fragment of each wedge into a planar conformation. The molecule itself possesses a high degree of planarity with an overall diameter of 28 Å. Compounds **19a-c** show liquid crystalline behavior. The strong intramolecular H-bonding in the

N-acylated 2,2'-bipyridine-3,3'-diamine with the amide N-H proton forced the bipyridine unit to be planar and to adopt a transoid conformation. The central benzene-1,3,5-tricarbonyl unit preferentially adopts a planar conformation in which all carbonyl groups point in the same direction giving rise to a C_3-symmetry and to an extended planar core, incorporating the bipyridine units. The presence of the peripheral lipophilic nonaromatic side chains induces liquid crystalline behavior, and the mesophases of compounds **19a-c** can be designated as discotic hexagonal phases (D_h) (Figure 1.12b and c).

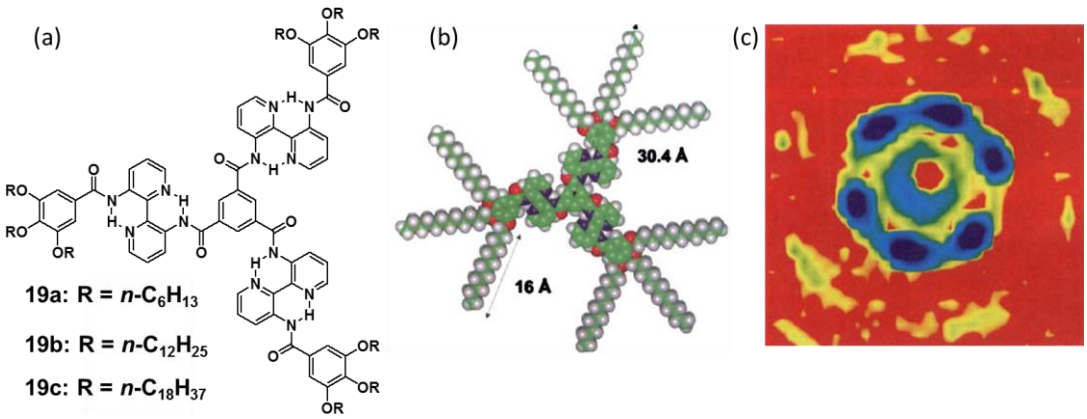

FIGURE 1.12. (a) Disc-shaped compounds based on *N*-acylated 2.2'-bipyridine-3.3'-diamine, (b) CPK model of compound **19b**. (c) The diffraction pattern observed in the small-angle area for compound **19c** at 120 °C. (Adapted with permission from ref. 36. Copyright 1997 WILEY-VCH.)

A BTA derivative **20** with three triphenylene groups connected to the periphery, was synthesized by Marcelis and co-workers (Figure 1.13).[39] The molecule, **20** displayed liquid crystalline property with the isotropization temperature around 208 °C and showed no crystallization at room temperature for several weeks. When viewed through an optical microscope, a ribbon-like texture with alternating dark and bright domains was observed. The intermolecular H-

bonding interaction leads to helix-like columns of benzenetrisamides in which the cores of successive molecules are rotated by 60°. Hence the orientation of the successive spacer group is almost 60° as proved by the computational studies. Still there is sufficient amount of overlap between the triphenylene cores of the adjacent molecules. Moreover, to investigate the potential of the additional stabilization by the H-bonds on the charge carrier mobility, pulse-radiolysis time-resolved microwave conductivity (PR-TRMC) measurements were performed. High charge carrier mobility of 0.06 $cm^2/V{\cdot}s$ is obtained at room temperature. This high value of charge carrier mobility is attributed to two factors. Firstly, the additional H-bonding reduces the movement of discs in the stack and restricts the rotation of the molecules. Secondly, the triphenylene can stack one over the other with very small rotation between the adjacent triphenylenes.

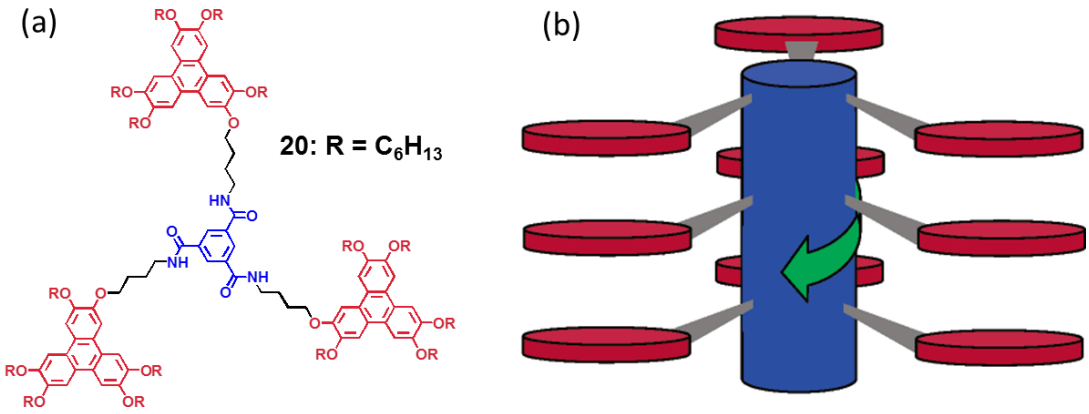

FIGURE 1.13. (a) Structure of the C_3-symmetrical trisamide derivative **20**. (b) Arrangement of the central trisamide H-bond stabilized column (blue) surrounded by three triphenylene π-stacked columns (red). The H-bond helical network is indicated by the green arrow. (Adapted with permission from ref. 39. Copyright 2006 The Royal Society of Chemistry.)

The effect of polar ethylene oxide side chains on the thermotropic liquid crystalline properties and the self-assembling properties of BTA derivatives were studied by Meijer and co-workers.[50] For this purpose, asymmetric BTA derivatives with both polar and apolar side chains, **21-26** (Chart 1.5) were prepared and their properties were investigated. It is found that replacement of one alkyl chain by one tetraethylene glycol chain lowers the stability of the mesophase by drastically lowering the clearing temperature (the temperature at which the liquid crystal transforms into an isotropic liquid) from 236 °C (compound **21**) to 134 °C (compound **22**). The reduction of clearing temperature upon the introduction of ethylene glycol chain was attributed to the greater conformational flexibility of the molecule with polar chains when compared to that of the molecule with alkyl chains. The presence of long ethylene glycol chain also reduces the self-assembling properties by lowering the association constant of the molecules in solutions. The possibility of back folding of the oligo(ethylene glycol) chains and the resulting competitive H-bonds may be the reason for low association constants after introducing ethylene oxide residues. On the other hand, the compounds **23** and **24** did not show any birefringence under crossed polarizer, indicating the absence of any long-range order in these molecules. Compound **25** and **26** show almost similar solid-state properties to that of **21** and **22** and also show liquid crystalline behavior. In the case of compound **25** and **26**, a reduction of around 50 ºC in clearing temperature was observed when compared to their symmetrical analogues.

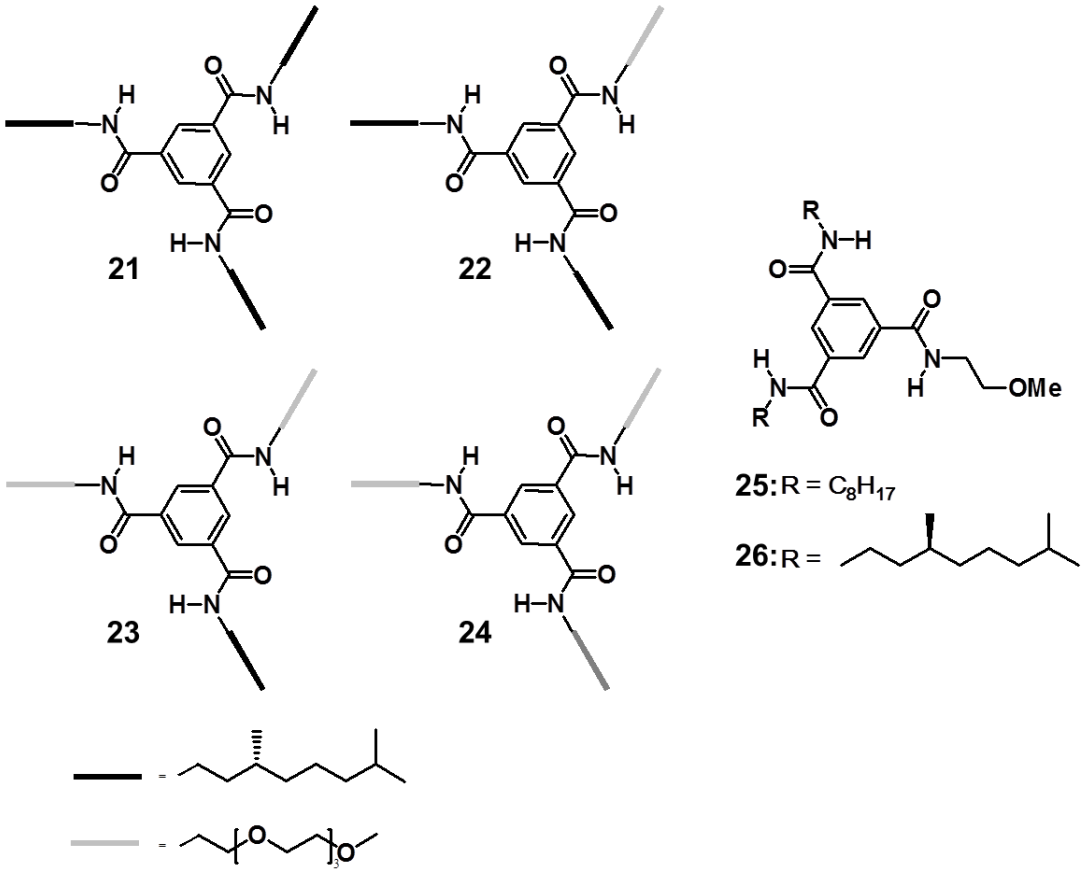

CHART 1.5. Chemical structure of compounds **21-26**.

Mesogenic diacetylenes, which can be polymerized in liquid crystalline state, has been prepared using BTA as the central core.[34] These molecules are of special interest because they can stack in columnar fashion. Zipping of diacetylenes along the column axis by polymerization leads to covalent fixation of supramolecules with columnar structures. One of the three BTA based liquid crystalline molecules has ester linkage (**27,** Figure 1.14 a) while the other two have amide linkage (**28** and **29**). These molecules showed an obvious difference in the clearing temperatures. For example, in the case of molecule **27**, the clearing transition is observed at 146 °C, whereas the same observed for **28** at temperature 204 °C and **28** displayed a discotic

nematic mesophase upon cooling. Needle-like texture was first observed for compound **28** and became thread-like by shearing as shown in Figure 1.14c. During the thermal polymerization, only one of the acetylene groups was found to involve in polymerization for the compound **28**. In the case of compound **27**, the polymerization occurred along the column direction, which involved the polymerization of more than one acetylenic group. The compound **29** is highly susceptible to thermal polymerization due to the absence of second phenyl ring in the side group.

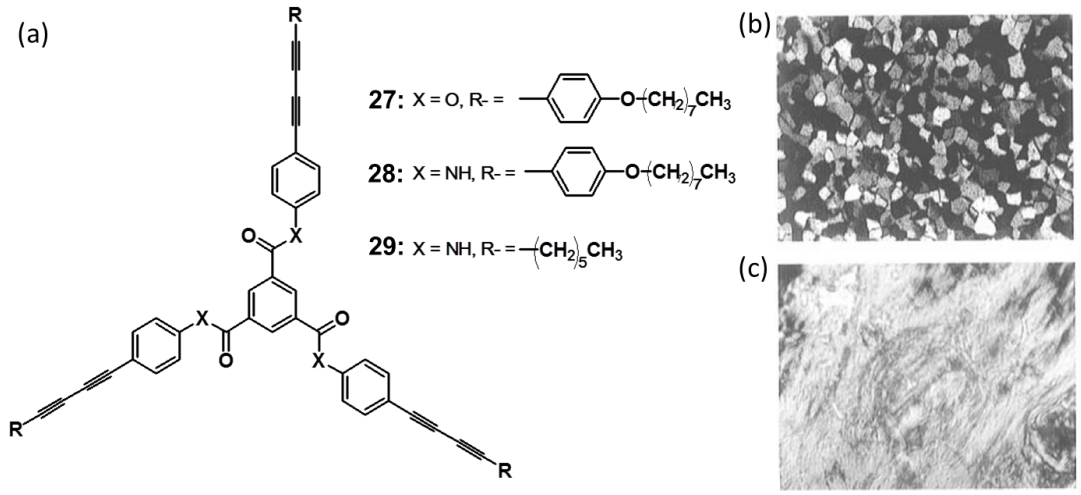

FIGURE 1.14. (a) Structures of the disc-like diacetylenes **27-29**. Optical polarized micrographs of (b) compound **27** at 137 °C obtained on cooling from the isotropic liquid (200 magnification) and (c) compound **28** obtained at 194 °C on heating (500 magnification). (Adapted with permission from ref. 34. Copyright 1997 American Chemical Society.)

1.4.3. Organogels

As already discussed, 1,3,5-benzenetrisamide (BTA) units have been extensively used for the design of dynamic 1D supramolecular assemblies via directional, threefold H-bonding interactions. BTA directed self-assembly have also resulted in

the formation of supramolecular gels in different polar and apolar solvents. Hence, decorating BTA with different π-conjugated chromophores is of great interest, because it would result in highly directional and stable assemblies of conjugated π-systems. In an attempt to obtain a new functional organogelator with potential photonic applications, Park and co-workers have designed and synthesized a BTA derivative with three 2,5-diphenyl[1,3,4]oxadiazole arms, **30** (Figure 1.15a).[78]

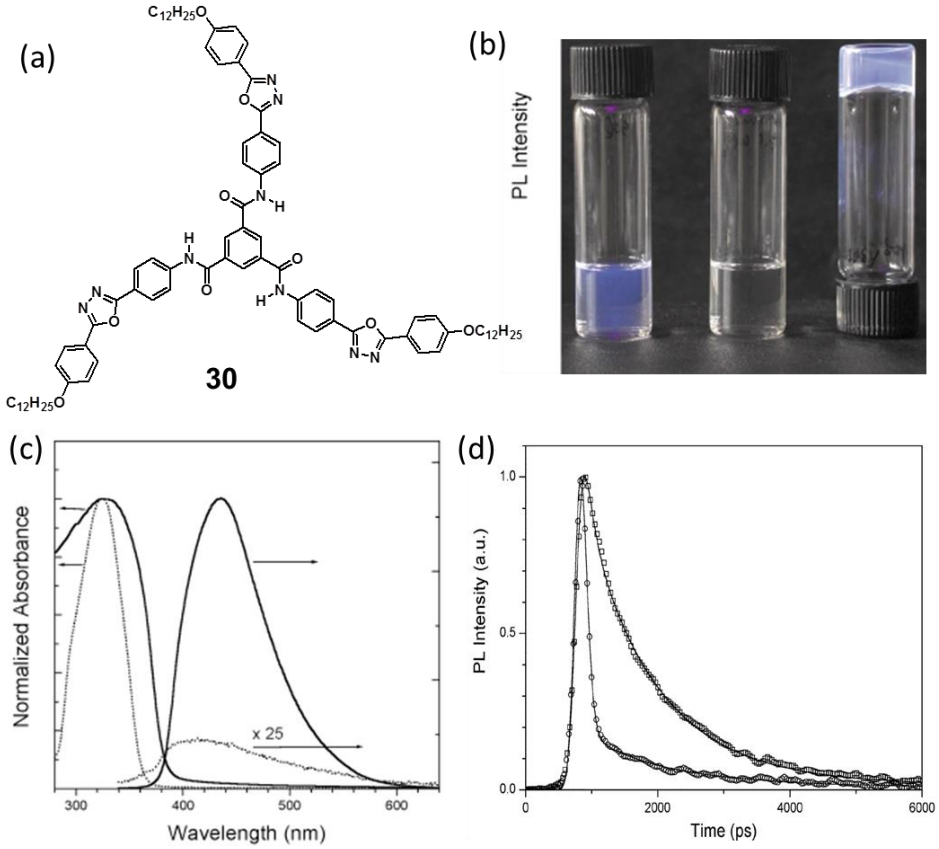

FIGURE 1.15. (a) Molecular structure of **30**. (b) Photographs of solutions and a gel of **30** taken under 365 nm illumination: (from left) 20 mM solution in $CHCl_3$, 0.1 wt% solution in $CHCl_3$/methanol = 9/1, and 0.1 wt% gel in $CHCl_3$. (c) Absorption and PL spectra of **30**: xerogel film (solid absorption), 20 mM solution in $CHCl_3$/methanol = 9/1 (dotted, absorption), 0.1 wt% gel in $CHCl_3$ (solid, PL), and 0.1 wt% solution in $CHCl_3$/methanol = 9/1 (dotted, PL). (d) Fluorescence lifetime decay profiles for monomer (o) and H-bonded aggregate (□) states of **30**. Samples were excited at 386 nm and monitored above 420 nm. Solid lines are

convoluted fits for the profiles. (Adapted with permission from ref. 78. Copyright 2004 The Royal Society of Chemistry.)

Here, the monomeric state is non fluorescent, however became highly luminescent upon the formation of H-bonded self-assembly (Figure 1.15b and c). In the case of the monomer with no H-bonding, the lowest singlet excited state undergoes a facile nonradiative decay via intersystem crossing (ISC) (Figure 1.15d). In the case of aggregates, the H-bonding between the molecules plays an important role in aggregation-induced luminescence generation by providing significant singlet–triplet splitting to reduce the rate of ISC.

Gunnlaugsson and co-workers have reported the gelation properties of a terpyridine functionalized BTA derivative (**31**) upon complexation with certain metal ions such as Eu^{III} (Figure 1.16).[79] The initial self-assembly of the ligand was facilitated by the threefold H-bonding from the BTA units. The BTA core was connected to three 2,2',6',2''-terpyridyl moieties through carboxamide spacers coordinated to Eu^{III} ions and resulted in the formation of higher order self-assembled metallogels. Here, the Eu^{III} ions functions as a "glue" by intermolecularly connecting such supramolecular polymers through coordination of Eu^{III} ions to more than one terpyridine unit in the adjacent strands (Figure 1.16). This intermolecular connection results in the formation of a luminescent metallogel with improved order and physical properties. 1D strands formed during the formation of gel and the corresponding high resolution TEM and XRD pattern are shown in Figure 1.16 b and c.

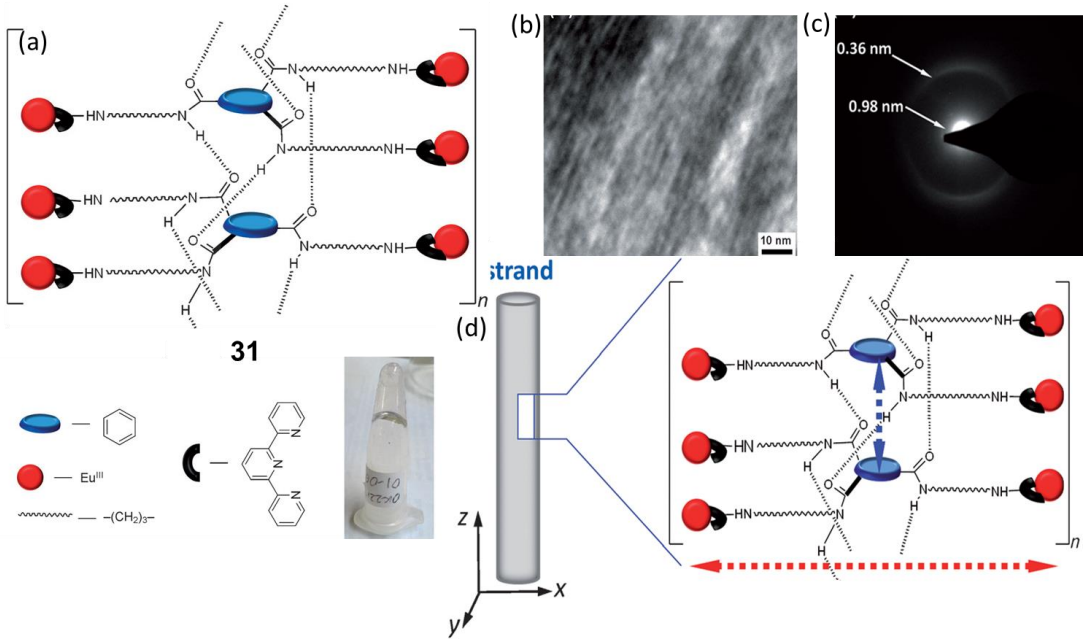

FIGURE 1.16. (a) A schematic representation of the possible formation of threefold H-bonding in helices of the terpyridine-based tripodal ligand, **31** (L) showing the europium binding sites on the outside of the helix. The inset shows formation of a transparent $EuCl_3$-L gel in a H_2O/CH_3OH solvent mixture. (b) TEM image of $EuCl_3$-L supramolecular gel. (c) Electron diffraction pattern. (d) Schematic representation of the self-assembly of L molecules and Eu^{III} ions within $EuCl_3$-L gels. The blue and red arrows correspond to the distances 0.36 and 0.98 nm (shown in (c)), respectively. (Adapted with permission from ref. 79. Copyright 2012 WILEY-VCH.)

Recently, organogels based on tetrathiafulvalenes (TTV) connected to BTAs were prepared by Amabilano *et al.*[80] Molecule **32a** formed organogel and when the corresponding xerogel was doped with iodine, charge transfer induced transport of charges was observed (Figure 1.17a).[80] The chiral derivative **32b** exhibited supramolecular chirality as observed by CD spectroscopy and morphological analysis. The solution of **32b** showed negative band in the CD spectrum and on quartz surface, a positive CD band was observed (Figure 1.17b). Microscopic

croissant-like structures were formed by slow cooling of drop casted hot solution of **32b** (10^{-3}M, Figure 1.17 c and d).[81]

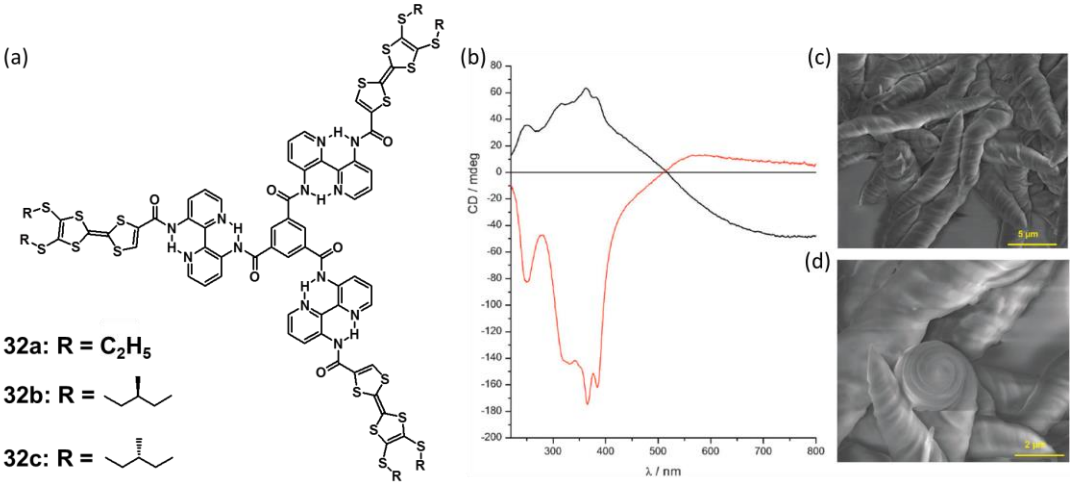

FIGURE 1.17. (a) Structure of the molecules **32a-c**. (b) CD spectra of a film of **32b** on quartz (positive bands at 350 nm, black line) and solution state (negative band at 350 nm, red line). Scanning electron microscope images (c) and (d) of the "micro-croissants" formed by molecule **32b**. (Adapted with permission from ref. 80. Copyright 2012 The Royal Society of Chemistry.)

It has been reported that porphyrin macrocycles form periodic patterns on mica substrate when connected to the BTA unit (Figure 1.18).[38] Highly ordered line pattern was formed by the combined effect of the molecular self-assembly and other physical processes such as contact-line pinning and hierarchical dewetting process. The strong self-assembly of **33** was the result of the balanced combination of intermolecular H-bonding and π-π interaction leading to the growth of columnar stacks of millimeter length. The contact-line pinning and solvent evaporation, caused the molecules dissolved in the droplet to follow a definite orientation, which then subjected to spinodal dewetting process. Combined with the propensity of **33** to

form one-dimensional (1D) aggregates, this dewetting gave rise to the formation of highly defined periodic patterns.

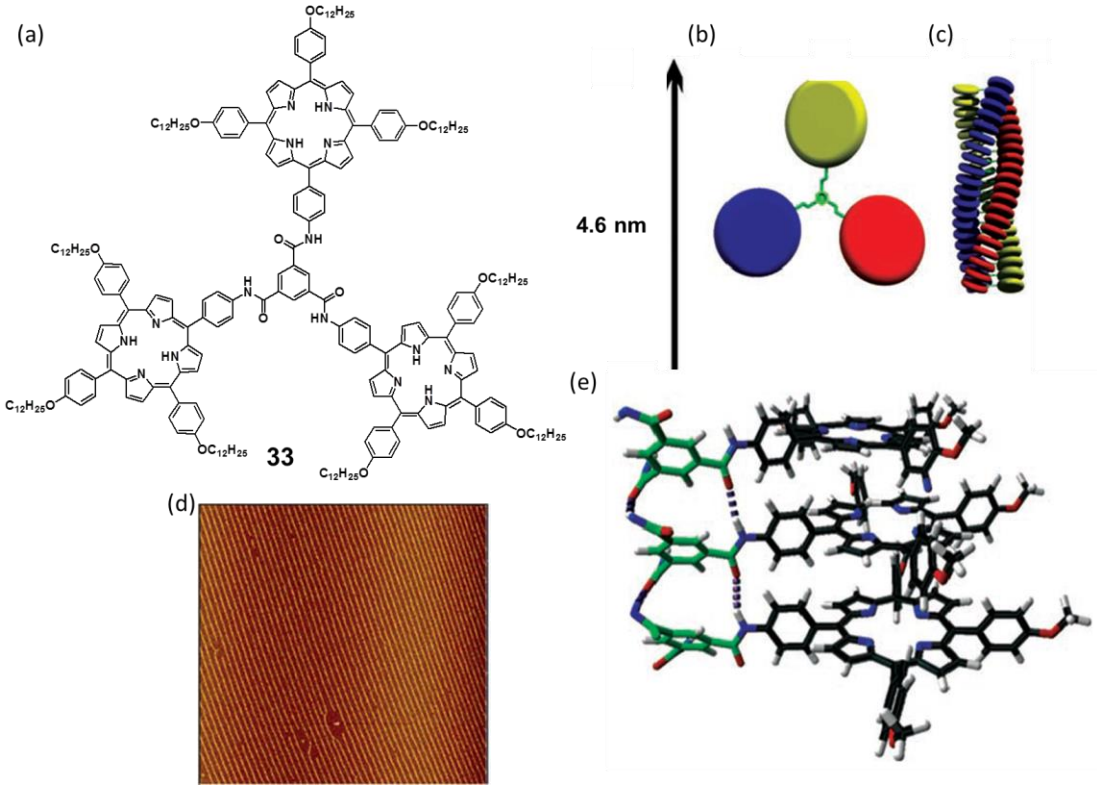

FIGURE 1.18. (a) Chemical structure of porphyrin trimer (**33**). (b) Schematic representation of **33**. (c) Schematic representation of a columnar stack of **33**. (d) AFM image (scan size = 25 × 25 mm^2) of a pattern of highly ordered equidistant parallel lines (e) Computer-generated model of the H-bonding network in a columnar stack of **33** (two of the three porphyrins of each molecule of **33** are omitted for clarity). (Adapted with permission from ref. 38. Copyright 2006 American Association for the Advancement of Science.)

1.5. Applications of BTA Derivatives as Sensors

A chemical sensor is a molecular device to detect a specific molecule or class of molecules.[82,83] The most common signal transduction method utilizes optical and electrical properties.[84] Fluorescence properties of molecules have been widely used for designing new sensors for various analytes. Fluorescence is a highly sensitive

optical transduction method, and therefore analyte binding events that produce an attenuation, enhancement, or wavelength shift in the emission can be used to produce a functional sensor.[85] On the other hand, the changes in absorption spectra, although less sensitive, have also been used for sensory applications.[86]

Recently, Brunsveld and coworkers have reported a disc shaped molecule, **34** that self-assembles into columnar supramolecular polymer at very lower concentration in water and other polar media (Figure 1.19a).[87] The polymerization of the same exhibited bright fluorescence when self-assembled. In order to provide a platform for attaching biologically important molecules, the terminal functional groups of the compound **34** was modified with an azide functionality (**35**). Modification of this compound by attaching a mannose unit produced final compound **36** (Figure 1.19a). The columnar assembly formed by the compound **36** can form effective scaffold that could bind and detect bacteria as a result of mannose-lectin interaction (-OH group of the sugar and the $-NH_2$ group of the amino acid). The strong fluorescence of the bacterial aggregate was observed only for mannose modified discotic **36** because of the presence of specific interacting site. The corresponding fluorescence microscopic images are shown in Figure 1.19d. The reversible self-assembly of monomers into polymers provides fine control over ligand density, polymeric architecture, and the environmental response to the biological counterpart, which is difficult to achieve with covalently attached polymeric systems.

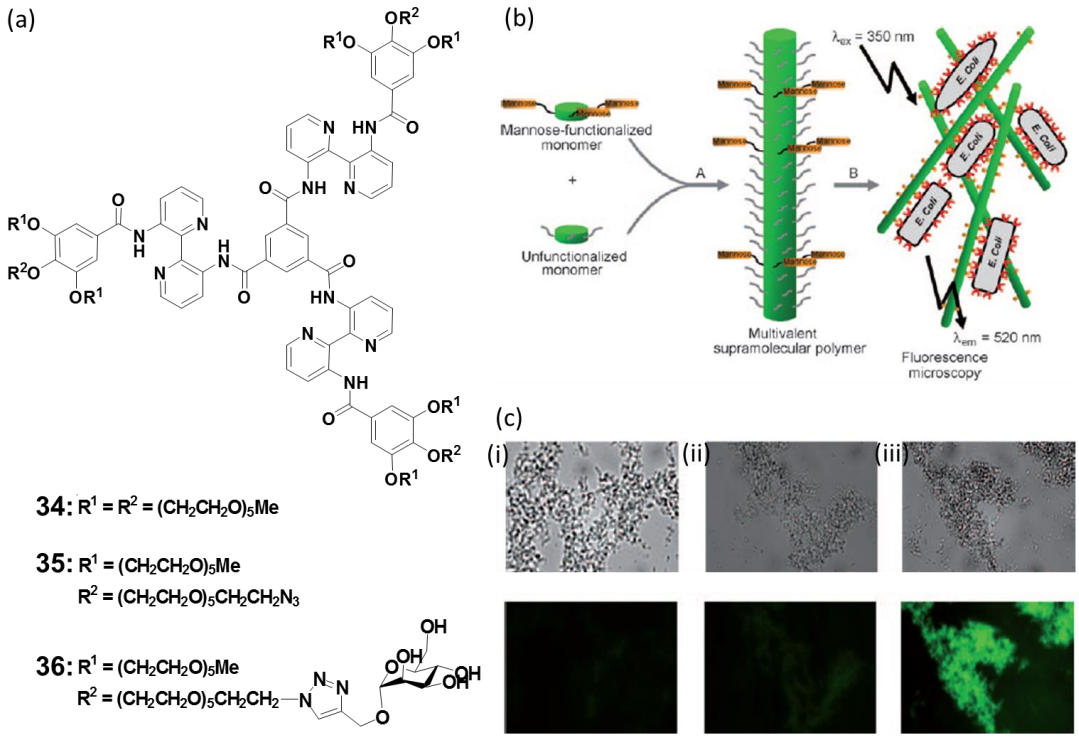

FIGURE 1.19. (a) Discotic compounds with inert glycol side chains (**34**), with azide functionalities for attachment of ligands (**35**), and with mannose moiety (**36**) in the periphery. (b) Schematic representation of the formation of polyvalent columnar supramolecular polymer and its interactions with bacteria. (c) Microscopy pictures in bright field (top) and fluorescence, λ_{ex} = 360 nm, λ_{em} = 490 nm mode (bottom) on E. coli incubated with (i) water, (ii) inert discotic **34**, (iii) mannose functionalized discotic **36**. (Adapted with permission from ref. 87. Copyright 2009 WILEY-VCH.)

Another interesting system that has been intensively studied in recent years is hexa-*peri*-hexabenzocoronenes (HBCs) which forms columnar stacking via mesophase or 1D self-assembly process.[88] The self-assembly and the fiber growth of the HBCs can be controlled by introducing alkyl chains or functional groups such as amide in the peripheral ring.[88] The water soluble HBC derivative **40** (Figure 1.20a) forms well organized microfibers with diameters ranging from 500 nm to 2 μm and length up to 200 μm. A negative charge is introduced on to the fiber through

multiple –COOH group at the periphery. These fibers act as templates for positively charged peptides by electrostatic interactions (Figure 1.20b). Positively charged peptide (Arg-Lys-Arg-Lys-Arg-Arg) enriched with amine groups were used for studying the electrostatic interaction between self-assembled polymer (**40**) and the peptide chain.

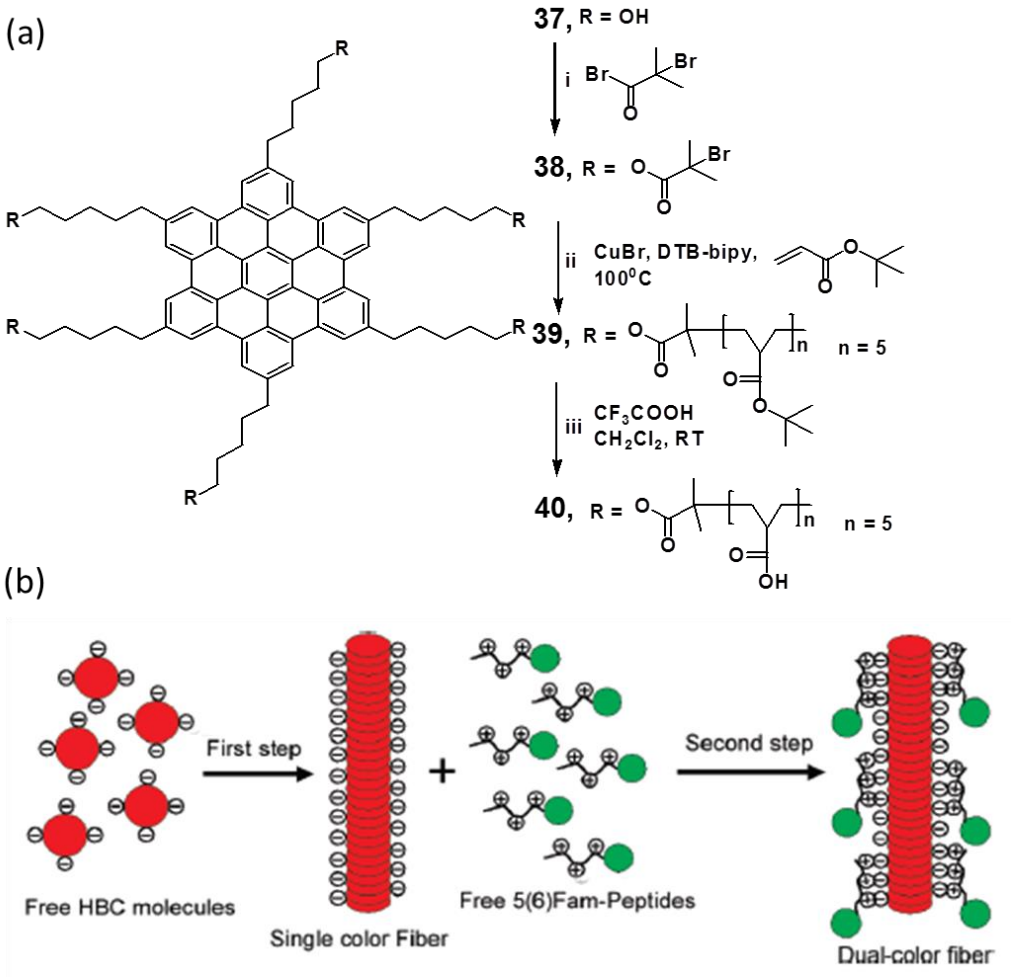

FIGURE 1.20. (a) Synthesis of negatively charged HBC derivative **40**. (b) Schematic drawing illustrates the two-step template strategy (The red color indicates the red fluorescence of HBC derivative and the green color indicate the green fluoresceine labeling of the peptide). (Adapted with permission from ref. 88. Copyright 2009 American Chemical Society.)

1.6. Origin, Objectives and Approach to the Thesis

Liquid crystals and organogels are two different classes of materials with vast interest in the area of fundamental and applied research. From the previous studies, the fundamental understanding of the design of C_3-symmetrical liquid crystal molecules are well established, however the design of the corresponding gelator molecules are still not fully understood, because most of the time gelation occurs in an unprecedented way. In this regard, we became interested to the rational design of new gelator system using C_3-symmetrical π-conjugated molecules. OPVs are a class of molecules that have been extensively studied due to their interesting optoelectronic properties. Our group has reported a number of functionalized OPVs and their spontaneous self-assembly from nonpolar hydrocarbon solvents at low concentrations that lead to gelation via the formation of entangled fiber network.[89] Even though modulation of optical, chiroptical and morphological features of OPV based gelators are studied well, these properties have not been properly exploited for any potential applications. One of the main objectives of the present thesis was to undertake a detailed investigation on the self-assembly, gelation and sensing properties of C_3-symmetrical OPV molecules with sufficient solid-state fluorescence quantum yields.

The structural design involves a benzenetrisamide unit in which OPV molecules are connected to the central benzene ring via C=O centered amide bonds (Scheme 1.1). The intermolecular H-bonding between amide functionalities, van der Waals interactions between alkyl chains and π-π interactions between planner

aromatic rings, facilitates the formation of supramolecular assembly and gels of these OPVs.

Depending upon the molecular structure, the self-assembly and gelation can be controlled, which may lead to changes in the morphology of the soft materials formed. When such materials are used as sensors, the morphology plays an important role in the selectivity and sensitivity.[90] Therefore, synthesis of different ***C*$_3$OPV**s (Scheme 1.1) forming different morphology under various experimental conditions were planned. The detailed study on the self-assembly behavior and application of these molecules in the sensing of nitroaromatics was also planned.

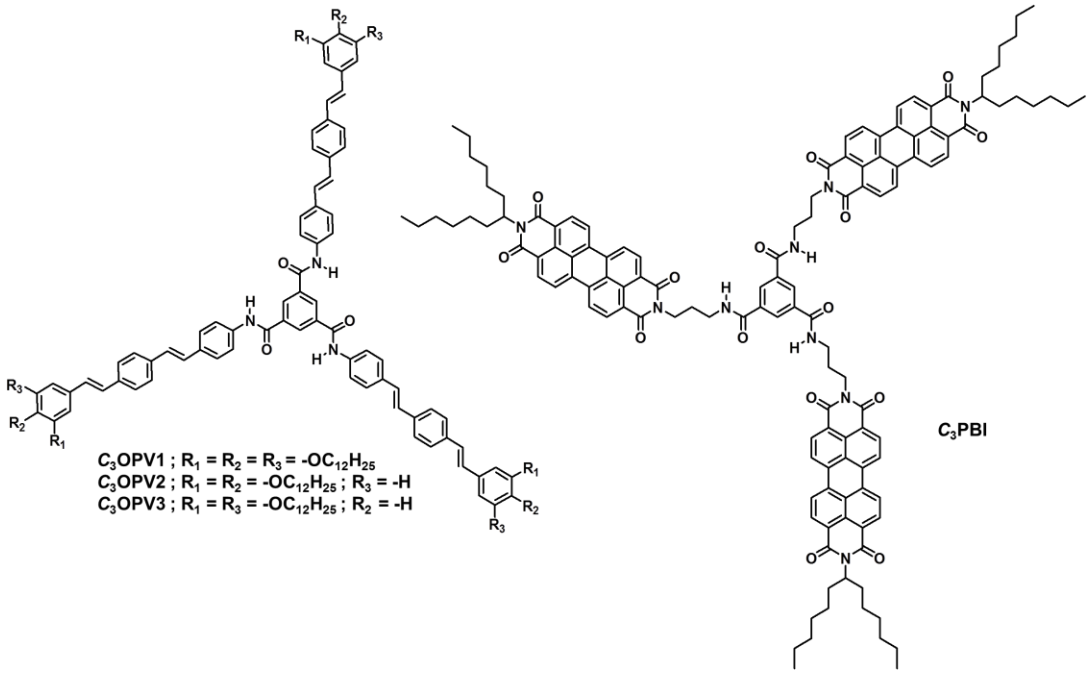

Scheme 1.1. Proposed molecular structures of ***C*$_3$OPV**s and ***C*$_3$PBI**.

Since OPVs are electron rich π-systems, we thought of exploring the use of electron deficient molecules such as perylene bisimide (PBI) on the discotic OPVs (Scheme 1.1). Detailed study on the combination of these two systems and their use

as sensor platform for the detection of volatile organic compounds were envisaged. Thus, the work described in the present thesis is the result of the detailed investigation on the synthesis, self-assembly, gelation properties and applications of C_3-symmetrical OPV and PBI systems.

1.7. References

1. Lehn, J. M. *Angew. Chem., Int. Ed. Engl.* **1990**, *29*, 1304–1319.
2. Lehn, J. M. *Proc. Natl. Acad. Sci. USA* **2002**, *99*, 4763–4768.
3. MacGillivray, L. R.; Atwood, J. L. *Nature* **1997**, *389*, 469–472.
4. Elemans, J. A. A. W.; Rowan, A. E.; Nolte, R. J. M. *J. Mater. Chem*. **2003**, *13*, 2661–2670.
5. (a) Lehn, J. M. *Chem. –Eur. J.* **2000**, *6*, 2097–2102; (b) Baxter, P. N. W.; Lehn, J. M.; Kneisel, B. O.; Baum, G.; Fenske, D. *Chem. –Eur. J.* **1999**, *5*, 113–120; (c) Philp, D.; Stoddart, J. F. *Angew. Chem., Int. Ed. Engl.* **1996**, *35*, 1155–1196.
6. (a) Mcculloch, I.; Heeney, M.; Bailey, C.; Genevicius, K.; Macdonald, I.; Shkunov, M.; Sparrowe, D.; Tierney, S.; Wagner, R.; Zhang, W. M.; Chabinyc, M. L.; Kline, R. J.; Mcgehee, M. D.; Toney, M. F. *Nat. Mater*. **2006**, *5*, 328–333; (b) Sirringhaus, H.; Wilson, R. J.; Friend, R. H.; Inbasekaran, M.; Wu, W.; Woo, E. P.; Grell, M.; Bradley, D. D. C. *Appl. Phys. Lett*. **2000**, *77*, 406–408.
7. Demus, D.; Goodby, J.; Gray, G. W.; Spiess, H. W.; Vill, V. *Handbook Of Liquid Crystals*, Wiley-VCH, Weinheim **1998**.
8. Chandrasekhar, S. *Liquid Crystals*, 2nd ed., Cambridge University Press, Cambridge **1992**.
9. Shirota, Y.; Kageyama, H. *Chem. Rev*. **2007**, *107*, 953–1010.

10. Kato, T.; Misoshita, N.; Kishimoto, K. *Angew. Chem., Int. Ed.* **2006**, *45*, 38–68.

11. Hegmann, T.; Qi, H.; Marx, V. M.; *J. Inorg. Organomet. Polym. Mater.* **2007**, *17*, 483–508.

12. Kumar, S. *Synth. React. Inorg., Met.-Org., Nano-Met. Chem.* **2007**, *37*, 327–331.

13. George, M.; Weiss, R. G. *J. Am. Chem. Soc.* **2001**, *123*, 10393–10394.

14. Terech, P.; Weiss, R. G. *Chem. Rev.* **1997**, *97*, 3133–3159.

15. Babu, S. S.; Praveen, V. K.; Ajayaghosh, A. *Chem. Rev.* **2014**, *114*, 1973−2129.

16. Babu, S. S.; Kartha, K. K.; Ajayaghosh, A. *J. Phys. Chem. Lett.* **2010**, *1*, 3413–3424.

17. Amabilino, D. B.; Puigmarti-Luis, J. *Soft Matter* **2010**, *6*, 1605–1612.

18. Babu, S. S.; Prasanthkumar, S.; Ajayaghosh, A. *Angew. Chem., Int. Ed*. **2012**, *51*, 1766–1776

19. Fukushima, T.; Asaka, K.; Kosaka, A.; Aida, T. *Angew. Chem., Int. Ed*. **2005**, *44*, 2410–2413.

20. Mukai, K.; Asaka, K.; Sugino, T.; Kiyohara, K.; Takeuchi, I.; Terasawa, N.; Futaba, D. N.; Hata, K.; Fukushima, T.; Aida, T. *Adv. Mater*. **2009**, *21*, 1582–1585.

21. Katakabe, T.; Kaneko, T.; Watanabe, M.; Fukushima, T.; Aida, T. *J. Electrochem. Soc*. **2005**, *152*, A1913–A1916.

22. Maeda, H. *Chem.–Eur. J*. **2008**, *14*, 11274–11282.

23. Piepenbrock, M.-O. M.; Lloyd, G. O.; Clarke, N.; Steed, J. W. *Chem. Rev*. **2010**, *110*, 1960–2004.

24. Banerjee, S.; Das, R. K.; Maitra, U. *J. Mater. Chem*. **2009**, *19*, 6649–6687.

25. Lloyd, G. O.; Steed, J. W. *Nat. Chem*. **2009**, *1*, 437–442.

26. Cantekin, S.; de Greef, T. F. A; Palmans, A. R. A. *Chem. Soc. Rev.* **2012**, *41*, 6125– 6137.

27. Matsunaga, Y.; Miyajima, N.; Nakayasu, Y.; Sakai, S.; Yonenaga, M. *Bull. Chem. Soc. Jpn*. **1988**, *61*, 207–210.

28. Curtius, T. *J. Prakt. Chem.* **1915**, *91*, 39–100.

29. Rohm & Haas Co., US patent *US*2774750, **1956**.

30. Ried, W.; Koenigstein, F. J. *Chem. Ber*. **1959**, *92*, 2532–2542

31. Stals, P. J. M.; Everts, J.; de Bruijn, R.; Filot, I. A. W.; Smulders, M. M. J.; Martín-Rapún, R.; Pidko, E. A.; de Greef, T. F. A.; Palmans, A. R. A.; Meijer, E. W. *Chem. –Eur. J*. **2010**, *16*, 810–821.

32. van Gorp, J. J.; Vekemans, J. A. J. M.; Meijer, E. W. *J. Am. Chem. Soc.* **2002**, *124*, 14759–14769.

33. Bernet, A.; Albuquerque, R. Q.; Behr, M.; Hoffmann, S. T.; Schmidt, H.-W. *Soft Matter* **2012**, *8*, 66–69.

34. Chang, J. Y.; Baik, J. H.; Lee, C. B.; Han, M. J. *J. Am. Chem. Soc*. **1997**, *119*, 3197–3198.

35. Palmans, A. R. A.; Vekemans, J. A. J. M.; Meijer, E. W.; Kooijmans, H.; Spek, A. L. *Chem. Commun.* **1997**, 2247–2248.

36. Palmans, A. R. A.; Vekemans, J. A. J. M.; Fischer, H.; Hikmet, R. A.; Meijer, E. W. *Chem. –Eur. J.* **1997**, *3*, 300–309.

37. Brunsveld, L.; Zhang, H.; Glasbeek, M.; Vekemans, J. A. J. M.; Meijer, E. W. *J. Am. Chem. Soc.* **2000**, *122*, 6175–6182.

38. van Hameren, R.; Schön, P.; van Buul, A. M.; Hoogboom, J.; Lazarenko, S.V.; Gerritsen, J. W.; Engelkamp, H.; Christianen, P. M.; Heus, H. A.; Maan, J. C.; Rasing, T.; Speller, S.; Rowan, A. E.; Elemans, J. A. A. W.; Nolte, R. J. M. *Science* **2006**, *314*,1433–1436.

39. Paraschiv, I.; Giesbers, M.; van Lagen, B.; Grozema, F. C.; Abellon, R. D.; Siebbeles, L. D. A.; Marcelis, A. T. M.; Zuilhof, H.; Sudhölter, E. J. R. *Chem. Mater.* **2006**, *18*, 968–974.

40. van Herrikhuyzen, J.; Jonkheijm, P.; Schenning, A. P. H. J.; Meijer, E. W. *Org. Biomol. Chem.* **2006**, *4*, 1539–1545.

41. Gong, B.; Zheng, C.; Yan, Y. *J. Chem. Crystallogr.* **1999**, *29*, 649–652.

42. Bose, P. P.; Drew, M. G. B.; Das, A. K.; Banerjee, A. *Chem. Commun*. **2006**, 3196–3198.

43. Besenius, P.; Portale, G.; Bomans, P. H. H.; Janssen, H. M.; Palmans, A. R. A.; Meijer, E. W. *Proc. Natl. Acad. Sci. USA* **2010**, *107*, 17888–17893.

44. Gelinsky, M.; Vogler, R.; Vahrenkamp, H. *Inorg. Chem*. **2002**, *41*, 2560–2564.

45. de Loos, M.; van Esch, J. H.; Kellogg, R. M.; Feringa, B. L. *Tetrahedron* **2007**, *63*, 7285–7301.

46. Veld, M. A. J.; Haveman, D.; Palmans, A. R. A.; Meijer, E. W. *Soft Matter* **2011**, *7*, 524–531.

47. van den Hout, K. P.; Martín-Rapún, R.; Vekemans, J. A. J. M.; Meijer, E. W. *Chem.–Eur. J.* **2007**, *13*, 8111–8123.

48. Matsuura, K.; Murasato, K.; Kimisuka, N. *J. Am. Chem. Soc.* **2005**, *127*, 10148–10149.

49. Akiyama, M.; Katoh, A.; Ogawa, T. *J. Chem. Soc., Perkin Trans. 2* **1989**, 1213–1219.

50. Stals, P. J. M.; Haveman, J. F.; Martín-Rapún, R.; Fitié, C. F. C.; Palmans, A. R. A.; Meijer, E. W. *J. Mater. Chem.* **2009**, *19*, 124–130.

51. Lee, S.; Lee, J.-S.; Lee, C. H.; Jung, Y.-S.; Kim, J.-M. *Langmuir* **2011**, *27*, 1560−1564.

52. Shikata, T.; Ogata, D.; Hanabusa, K. *J. Phys. Chem. B* **2004**, *108*, 508–514.

53. Shi, N.; Dong, H.; Yin, G.; Xu, Z.; Li, S. *Adv. Funct. Mater.* **2007**, *17*, 1837–1843.

54. Fitié, C. F. C.; Tomatsu, I.; Byelov, D.; de Jeu, W. H.; Sijbesma, R. P. *Chem. Mater.* **2008**, *20*, 2394–2404.

55. Besenius, P.; Heynens, J. L. M.; Straathof, R.; Nieuwenhuizen, M. M. L.; Bomans, P. H. H.; Terreno, E.; Aime, S.; Strijkers, G. J.; Nicolay, K.; Meijer, E. W. *Contrast Media Mol. Imaging* **2012**, *7*, 356–361.

56. Blomenhofer, M.; Ganzleben, S.; Hanft, D.; Schmidt, H.-W.; Kristiansen, M.; Smith, P.; Stoll, K.; Maeder, D.; Hoffmann, K.; *Macromolecules* **2005**, *38*, 3688–3695.

57. Broaders, K. E.; Pastine, S. J.; Grandhe, S.; Fréchet, J. M. J. *Chem. Commun*. **2011**, *47*, 665–667.

58. Kristiansen, M.; Smith, P.; Chanzy, H.; Baerlocher, C.; Gramlich, V.; McCusker, L.; Weber, T.; Pattison, P.; Blomenhofer, M.; Schmidt, H.-W. *Cryst. Growth Des*. **2009**, *9*, 2556–2558.

59. Stals, P. J. M.; Smulders, M. M. J.; Martín-Rapún, R.; Palmans, A. R. A.; Meijer, E. W. *Chem.–Eur. J.* **2009**, *15*, 2071–2080.

60. Ryu, S. Y.; Kim, S.; Seo, J.; Kim, Y.-W.; Woon, O.-H.; Jang, D.-J.; Park, S. Y. *Chem. Commun.* **2004**, 70–71.

61. Brunsveld, L.; Schenning, A. P. H. J.; Broeren, M. A. C.; Janssen, H. M.; Vekemans, J. A. J. M.; Meijer, E. W. *Chem. Lett.* **2000**, 292–293.

62. de Greef, T. F. A.; Smulders, M. M. J.; Wolffs, M.; Schenning, A. P. H. J.; Sijbesma R. P.; Meijer, E. W.; *Chem. Rev.* **2009**, *109*, 5687–5754.

63. Rajput, L.; Biradha, K. *J. Mol. Struct*. **2008**, *876*, 339–343.

64. Brunsveld, L.; Schenning, A. P. H. J.; Broeren, M. A. C.; Janssen, H. M.; Vekemans, J. A. J. M.; Meijer, E. W. *Chem. Lett*. **2000**, 292–293.

65. Smulders, M. M. J.; Buffeteau, T.; Cavagnat, D.; Wolffs, M.; Schenning, A. P. H. J.; Meijer, E. W. *Chirality* **2008**, *20*, 1016–1022.

66. Cantekin, S.; Balkenende, D. W. R.; Smulders, M. M. J.; Palmans, A. R. A.; Meijer, E. W. *Nat. Chem*. **2011**, *3*, 42–46.

67. Lightfoot, M. P.; Mair, F. S.; Pritchard, R. G.; Warren, J. E. *Chem. Commun*. **1999**, 1945–1946.

68. Smulders, M. M. J.; Schenning, A. P. H. J.; Meijer, E. W. *J. Am. Chem. Soc*. **2008**, *130*, 606–611.

69. Smulders, M. M. J.; Nieuwenhuizen, M. M. L.; de Greef, T. F. A.; van der Schoot, P.; Schenning, A. P. H. J.; Meijer, E. W. *Chem. –Eur. J.* 2010, *16*, 362–367.

70. Filot, I. A. W.; Palmans, A. R. A.; Hilbers, P. A. J.; van Santen, R. A.; Pidko, E. A.; de Greef, T. F. A. *J. Phys. Chem. B* **2010**, *114*, 13667–13674.

71. Sakamoto, A.; Ogata, D.; Shikata, T.; Urakawa, O.; Hanabusa, K. *Polymer* **2006**, *47*, 956–960.

72. Smulders, M. M. J.; Schenning, A. P. H. J.; Meijer, E. W. *J. Am. Chem. Soc.* **2008**, *130*, 606–611.

73. Narayan, B.; Kulkarni, C.; George, S. J. *J. Mater. Chem. C* **2013**, *1*, 626–629.

74. Chandrasekhar, S.; Sadashiva, B. K.; Suresh, K. A. *Pramana* **1977**, *9*, 471–480.

75. Kumar, N. S. S.; Varghese, S.; Suresh, C. H.; Rath, N. P.; Das, S. *J. Phys. Chem. C* **2009**, *113*, 11927–11935.

76. Sugita, A.; Suzuki, K.; Tasaka, S. *Jpn. J. Appl. Phys*. **2008**, *47*, 8043–8048.

77. Fitié, C. F. C.; Roelofs, W. S. C.; Kemerink, M.; Sijbesma, R. P. *J. Am. Chem. Soc.* **2010**, *132*, 6892–6893.

78. Ryu, S. Y.; Kim, S.; Seo, J.; Kim, Y.-W.; Kwon, O.-H.; Jang, D.-J.; Park, S. Y. *Chem. Commun.* **2004**, 70–71.

79. Kotova, O.; Daly, R.; dos Santos, C. M. G.; Boese, M.; Kruger, P. E.; Boland, J. J.; Gunnlaugsson, T. *Angew. Chem., Int. Ed*. **2012**, *51*, 7208–7212.

80. Danila, I.; Riobé, F.; Puigmartí-Luis, J.; del Pino, Á. P.; Wallis,J. D.; Amabilino, D. B.; Avarvari, N. *J. Mater. Chem*. **2009**, *19*, 4495–4504.

81. Danila, I.; Pop, F.; Escudero, C.; Feldborg, L. N.; Puigmartí-Luis, J.; Riobé, F.; Avarvari, N.; Amabilino, D. B. *Chem. Commun*. **2012**, *48*, 4552–4554.

82. Czarnik, A. W. Ed. *Fluorescent Chemosensors for Ion and Molecular Recognition*, ACS Symposium Series 538, American Chemical Society: Washington, DC, **1993**.

83. Desvergne, J.-P.; Czarnik, A. W. *Chemosensors of Ion and Molecular Recognition*, Eds., NATO ASI Series, Series C: Vol. 492, Kluwer Academic Press: Dordrecht, **1997**.

84. Hirschfeld, T.; Callis, J. B.; Kowalski, B. R. *Science* **1984**, *226*, 312–318.

85. Bissell, R. A.; de Silva, A. P.; Gunaratne, H. Q. N.; Lynch, P. L. M.; Maguire, G. E. M.; McCoy, C. P.; Sandanayake, K. R. A. S. *Fluorescent PET (Photoinduced Electron Transfer) Sensors* in *Topics in Current Chemistry*; Springer-Verlag: Berlin Heidelberg, **1993**, *168*, 224–245.

86. Borman S. *Anal. Chem.* **1987**, *59*, 1161A–1164A.

87. Müller, M. K.; Brunsveld, L. *Angew. Chem., Int. Ed*. **2009**, *48*, 2921–2924.

88. Yin, M.; Shen, J.; Pisula, W.; Liang, M.; Zhi, L.; Müllen, K. *J. Am. Chem. Soc***.** **2009**, *131*, 14618–14619.

89. George, S. J.; Ajayaghosh, A. *Chem. –Eur. J.* **2005**, *11*, 3217–3227.

90. Kartha, K. K.; Sandeep, A.; Nair, V. C.; Takeuchi, M.; Ajayaghosh, A. *Phys. Chem Chem. Phys.* **2014**, *16*, 18896–18901.

Chapter 2

Effect of Alkyl Chains in C_3-Symmetrical OPVs on Self-assembly, Liquid Crystalline Behavior and Gelation

2.1. Abstract

To design a liquid crystal or an organogelator, a rational understanding of the structural features and possible molecular interactions are necessary. Herein we report the effect of structural parameters such as the number of alkyl chains on the self-assembling properties of a series of π-conjugated molecules. For this purpose we designed and synthesized three C_3-symmetrical molecules based on oligo(p-phenylenevinylene), ***C_3OPV1-3****. The self-assembly properties of these molecules are studied in the solid and solution state. All the three molecules form self-assembly through isodesmic pathway with different aggregate stabilities. Out of these molecules, only* ***C_3OPV1****, with nine peripheral alkoxy chains could show the liquid crystalline property. Upon cooling from isotropic melt* ***C_3OPV1*** *formed columnar phase with two-dimensional (2D) rectangular lattice and retained the liquid crystalline phase even at room temperature. The gelation ability is shown only by* ***C_3OPV2****. Even though both* ***C_3OPV2*** *and* ***C_3OPV3*** *molecules are structural isomers with six peripheral alkoxy chains, only* ***C_3OPV2*** *were able to form gel, whereas* ***C_3OPV3*** *could not.*

2.2. Introduction

Liquid crystals (LC) and gels are two distinct classes of soft materials of contemporary importance from the view point of basic and applied research.[1-9] While, the fundamental understandings of LCs have helped the rational design and application of several subclasses,[10,11] the case of molecular gelators are completely different. The critical understanding of the structural features that can impart such properties is essential to the design of new soft materials. Self-organization events involving H-bonding plays a crucial role in the formation of LC phases and its stabilization.[12-29] Soft side chains are introduced to the hard core in order to prevent the crystallization.

Most of the earlier reports on gelators are serendipitous. However, the continued effort over the years has helped researchers to have a better understanding of the requirements of gelator design.[30-35] Presence of functional groups such as hydroxyl, amide, urea and carboxylic acid that can form H-bonding has been proved as one of the essential requirements for the formation of gel. The directionality and the rigidity of H-bonding interaction help the spatial arrangement of the chromophore to achieve efficient gelation. Molecules with structural motifs such as amino acids, peptides, etc. also assist the formation of gel. The presence of aromatic rings in the molecule facilitates π-π stacking and thereby assists the gelation process. Other structural motifs that induce dipole-dipole, donor-acceptor interactions also help gelation process. Another important structural requirement for molecules to assist gelation is the presence of long hydrocarbon chains with optimum chain length. The presence of the hydrocarbon chains facilitate van der Waals interaction

between the gelator molecules and also help maintaining a subtle balance between solubility and precipitation of the gelator molecule in a given solvent.[36]

Several examples of organogels are known in the literature. Initially, cholesterol based gels were extensively synthesized and studied for their use as the template to create a variety of nanomaterials.[37-39] Later π-gelators were introduced as a novel class of soft functional materials.[40,41] π-Gelators are mainly derived by the self-assembly of aromatic π-systems.[6,34,42] Among different π-gelators, phenylenevinylenes (PVs) are one of the well-studied classes of molecules due to their importance in various electro-optical devices such as light-emitting diodes (LEDs),[43,44] photovoltaic cells[45-49] and field-effect transistors (FETs).[50-52] Control of the HOMO-LUMO gap by donor-acceptor interaction and by varying the conjugation length of π-conjugated oligomers provides materials with well-defined functional properties.[53-55]

In the first report on fluorescent *p*-phenylenevinylene derivatives as π-gelators, Ajayaghosh and coworkers have described the thermoreversible gelation of molecules **1a** and **1b** (Figure 2.1a) by cooperative H-bonding and π-stack induced self-assembly.[56a,b] Gelation could be significantly controlled by changing the H-bonding groups as well as varying the length of the alkyl chains. Gelation is weak or even not observed when the hydroxyl group is changed to an ether moiety, **1c** (Figure 2.1a). In the case of molecule **1d** without any functional end-groups (Figure 2.1a), no gelation was observed. The scanning electron microscopic (SEM) image of a dried gel of **1a** revealed the formation of entangled nanostructures of

approximately 100-150 nm width (Figure 2.1b). The probable way of self-assembly of the molecules is shown in Figure 2.1c.

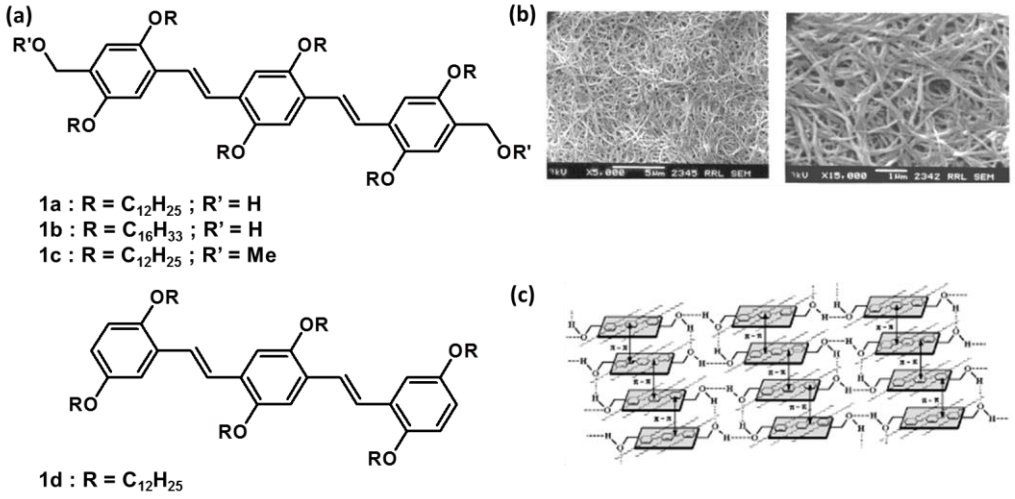

Figure 2.1. (a) The structure of OPVs, (b) SEM images of a dried gel of **1a** from toluene and (c) the probable self-assembly of OPV gelator in the gel state. (Adapted with permission from ref. 56a. Copyright 2001 American Chemical Society.)

C_3-symmetrical platforms, which are well exploited to the design of columnar LCs[57-59] have also been reported to be suitable for the design of supramolecular gelators.[60-63] We decided to explore the potential of C_3-symmetrical systems with one of the well-studied π-gelators, oligo(*p*-phenylenevinylenes) (OPVs) to the design of LC based π-gelators in order to create multifunctional soft materials. In this process, we encountered with an interesting observation of remarkable property variations of a C_3-symmetrical OPV molecule ***C*$_3$OPV1** when a terminal alkoxy chain is knocked out to form the molecule ***C*$_3$OPV2** and ***C*$_3$OPV3** (Figure 2.2). In this chapter, we describe the details of these studies.

Over the past decade a large number of C_3-symmetrical benzene-1,3,5-tricarboxamide (BTA) based molecules are reported.[64-66] These molecules find wide-range of applications in the field of nanostructured materials,[64] metal complexation reagents[65] and in drug delivery.[66] LCs and organogels based on C_3-symmetrical discotic molecules are also well studied.[67,68] Some of the discotics reported can form both LC and organogel,[69] whereas some others can show either of the properties. This means that there is a delicate balance in the structure of the discotic molecules to exhibit LC and gelation properties.

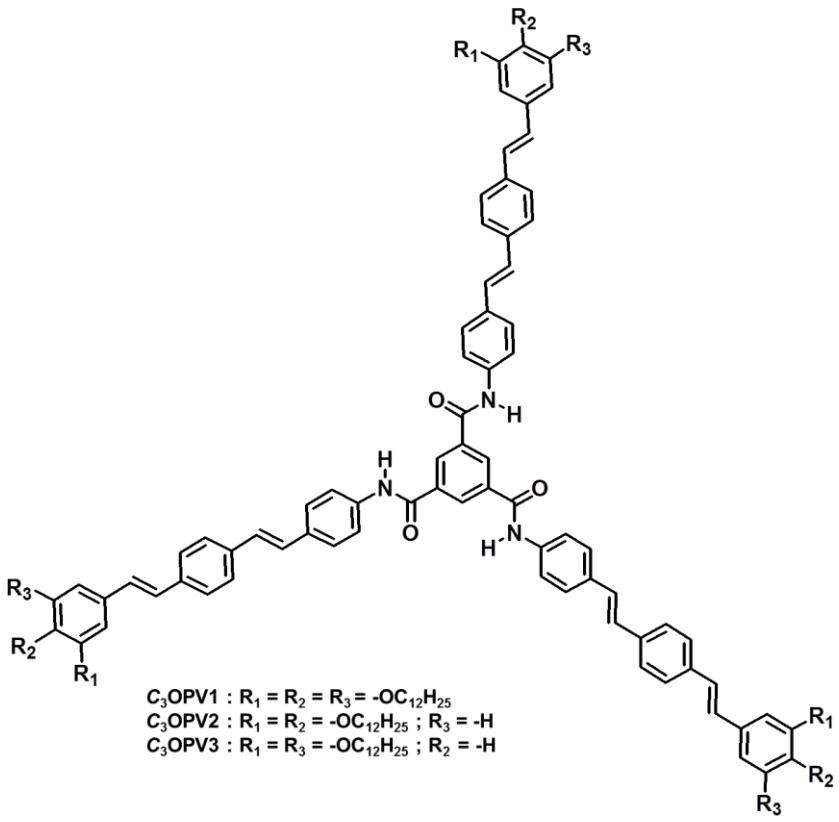

Figure 2.2. Molecular structure of ***C*$_3$OPV1**, ***C*$_3$OPV2** and ***C*$_3$OPV3**.

2.3. Results and Discussion

2.3.1. Synthesis of C_3OPV1, C_3OPV2 and C_3OPV3

Synthesis of ***C*$_3$OPV1**, ***C*$_3$OPV2** and ***C*$_3$OPV3** were achieved as shown in Scheme 2.2. The intermediate compounds (**2**-**6**) required for the synthesis of ***C*$_3$OPV1**, ***C*$_3$OPV2** and ***C*$_3$OPV3** were prepared as per Scheme 2.1. Bromination of 4-methyl-benzonitrile (**2**) was carried out with *N*-bromosuccinimide. The bromomethyl derivative **3** obtained in 90% yield was converted into 4-(bromomethyl)benzaldehyde (**4**) by reduction reaction using diisobutylaluminium hydride (DIBAL-H), in 70% yield. The aldehyde **4** was then protected using 2,2-dimethyl-1,3-propanediol to get the molecule **5** in 80% yield which was then converted into the phosphonate ester **6** by treating **5** with triethylphosphite in 90% yield.

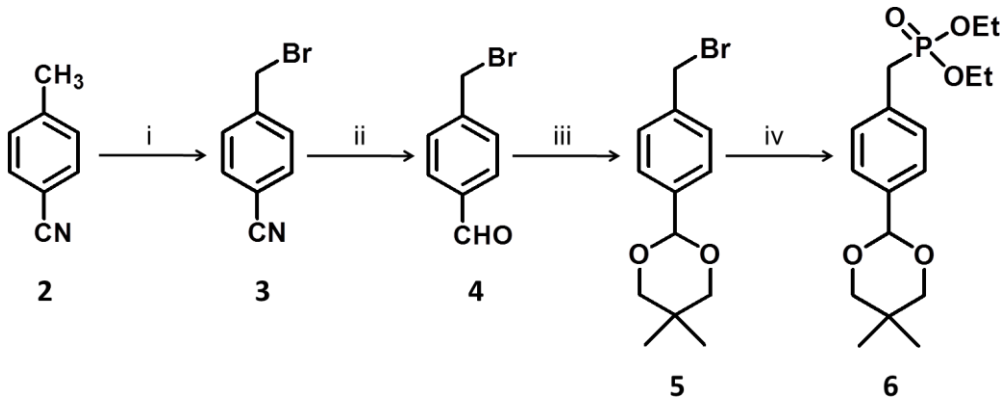

Scheme 2.1. Reagents and conditions: (i) *N*-bromosuccinimide, AIBN, dry CCl_4 , 80 ºC, 12 h, 90%; (ii) DIBAL-H, dry toluene, 0 ºC, 1 h, 70%; (iii) 2,2-dimethyl-1,3-propanediol, dry benzene, pyridinium hydrochloride (catalytic amount) 100 ºC, 10 h, 80%; (iv) triethylphosphite, 110 ºC, 8 h, 90%.

The alkylated benzaldehyde derivatives (**8a**-**c**) were synthesized by treating the corresponding hydroxybenzaldehyde (**7a**-**c**) with 1-bromododecane in 90-95% yield

(Scheme 2.2). The Wittig-Horner-Emmons olefination reaction of **8**a-c with the phosphonate **6** afforded compounds **9a-c** in 82-85% yield which was then deprotected using trifluoroacetic acid to yield the aldehydes **10a-c** in 88-90% yield. The aldehydes **10a-c** were then subjected to Wittig-Horner-Emmons olefination reaction with diethyl(4-nitrobenzyl)phosphonate to yield the nitro derivatives **11a-c** in 80-82% yield. The nitro compounds **11a-c** were then reduced to the amino compounds **12a-c** using stannous chloride as the reducing agent in 80-85% yield.

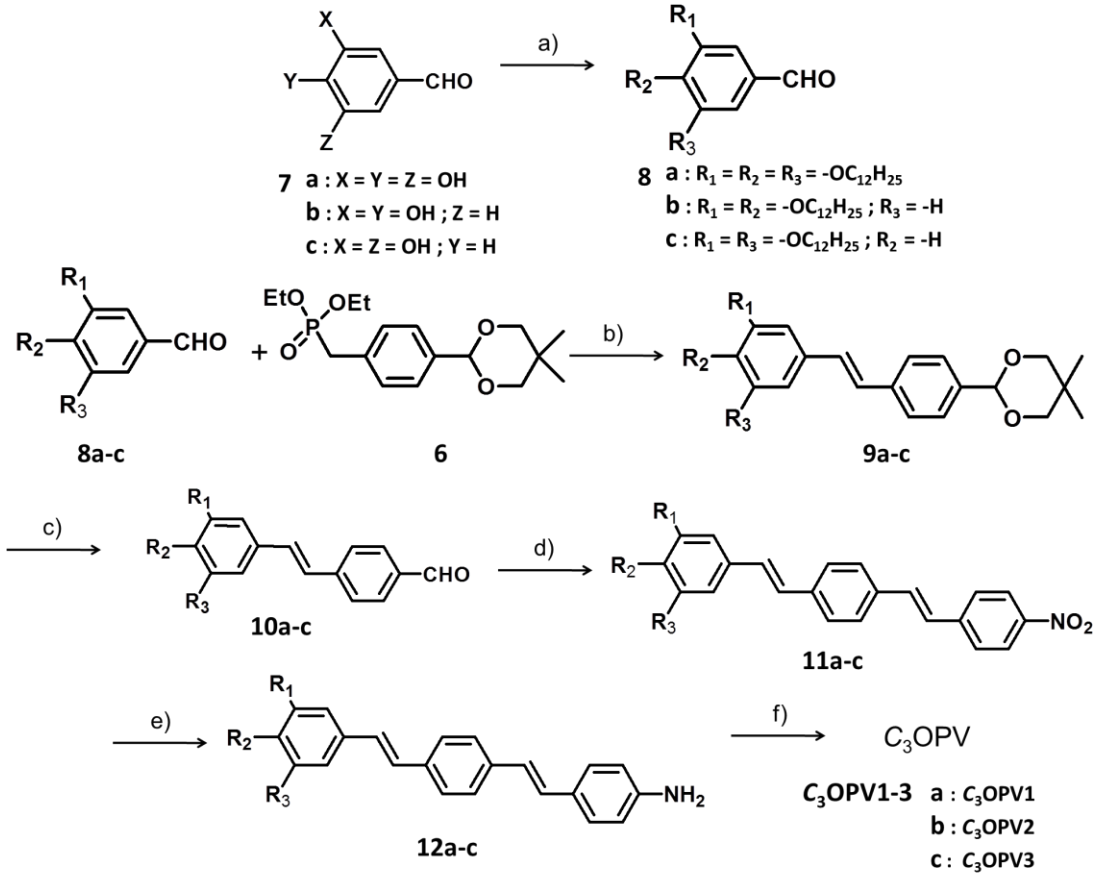

Scheme 2.2. Reagents and conditions: (a) 1-bromododecane, K_2CO_3, DMF, 70 ºC, 14 h; (b) NaH, dry THF, rt., 5 h; (c) TFA, dry CH_2Cl_2, rt., 2 h; (d) diethyl(4-nitrobenzyl)phosphonate, NaH, dry THF, rt., 5 h; (e) stannous chloride, dry THF, 60 ºC, 4 h; (f) trimesic acid trichloride, Et_3N, dry CH_2Cl_2, rt., 6 h, 45% (***C*$_3$OPV1**), 50% (***C*$_3$OPV2**) and 42% (***C*$_3$OPV3**).

The OPV amine derivatives **12a-c** were then converted into the corresponding ***C*$_3$OPV** by treating with trimesic acid trichloride (Scheme 2.2).[70] All the reactions were carried out under dark condition in order to avoid the *cis-trans* isomerization of the olefinic double bond. All the intermediates and the final molecules, ***C*$_3$OPV1**, ***C*$_3$OPV2** and ***C*$_3$OPV3** were characterized by ^{1}H and ^{13}C NMR, FT-IR spectroscopy and MALDI-TOF mass spectrometry techniques. The details of the synthesis and characterization are given in the experimental section.

2.3.2. Liquid Crystalline Properties

2.3.2.1. Optical Polarizing Microscopic (OPM) Studies

Having obtained the C_3-symmetrical OPV molecules in pure forms, our first objective was to study their LC properties. The preliminary characterization of the LC phases was carried out by optical polarizing microscopy (OPM). OPM studies revealed that due to the presence of strong amide H-bonding, these molecules exhibit high clearing temperatures (> 260 ºC), and therefore get charred at these temperatures. Thus, to avoid such issues, the as prepared sample was first heated just below the clearing temperature and slowly cooled back to room temperature with a cooling rate of 5 K min^{-1}. In the case of ***C*$_3$OPV1**, upon cooling, a clear dendritic growth was observed with subsequent formation of a strongly birefringent LC texture (Figure 2.3a). With further cooling, a mosaic pattern is observed, which is retained right down to room temperature (Figure 2.3b). In some cases focal conics with stunted ends and stripes on the back of them was observed (Figure 2.4). Keeping these features in mind and the X-ray results to be described below, we identify the mesophase to be a columnar phase with 2-d rectangular lattice. It should

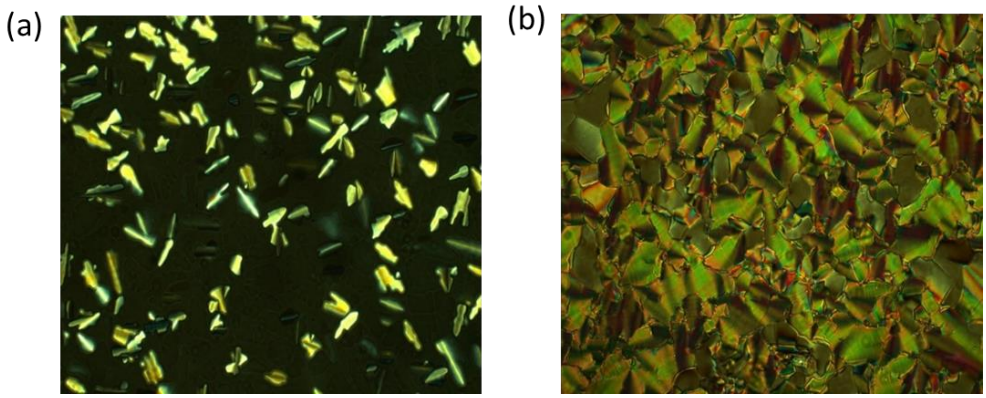

Figure 2.3. OPM images of ***C*$_3$OPV1** (a) at 257 °C and (b) at 28 °C upon cooling the sample heated just below the clearing temperature.

however be mentioned that unlike the sharp and narrow stripes observed generally for the rectangular columnar phase, the stripes seen here were quite broad.

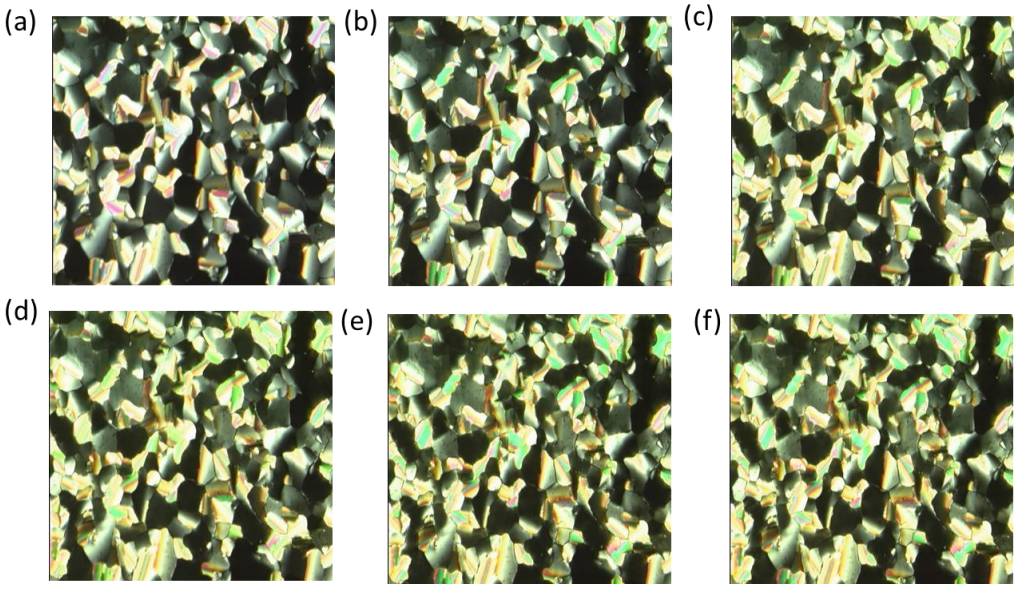

Figure 2.4. OPM images of ***C*$_3$OPV1** (a) at 254 °C, (b) at 218 °C, (c) at 165°C, (d) at 118°C, (e) at 65 °C and (f) at 40 °C upon cooling the sample heated just below the clearing temperature.

Homeotropic alignment of the sample with a dark field of view under OPM, very commonly observed for the hexagonal columnar phase, was also missing, further supporting the rectangular nature of the lattice.[71] The other two derivatives ***C*$_3$OPV2**

and ***C*$_3$OPV3** showed no characteristic textures and lack LC property. Due to the decomposition of samples at the clearing point, we were unable to characterize phase transitions using differential scanning calorimetry.

2.3.2.2. X-ray Diffraction Studies

The detailed identification of the columnar phase of ***C*$_3$OPV1** was carried out using temperature-dependent X-ray diffraction (XRD) at different temperatures by cooling down the sample from 250 ºC to room temperature (28 ºC). The main panel of Figure 2.5 shows the XRD profiles of ***C*$_3$OPV1** in the low angle region and obtained at 200 ºC and 28 ºC (RT). At all temperatures, a very intense and sharp peak at low angles and a diffuse maximum at wide angles (inset B of Figure 2.5) were seen.

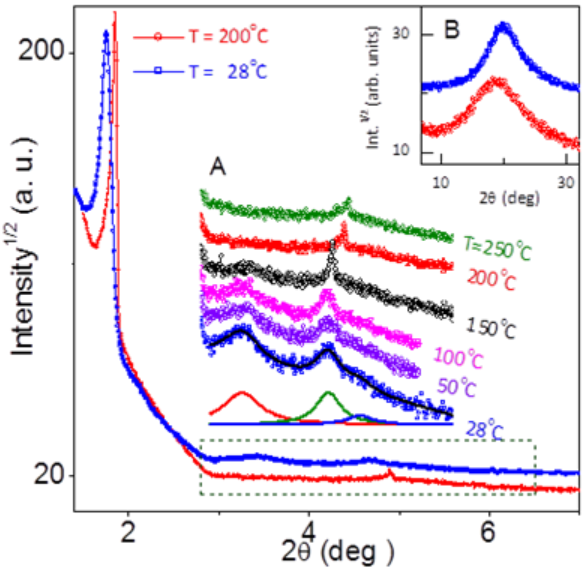

Figure 2.5. XRD profile of ***C*$_3$OPV1** at 200 ºC (red) and 28 ºC (blue). The low angle region is shown in the main panel; the expansion (A) and the wide angle portion (B) are shown in the inset.

In addition, a very weak, but sharp peak was seen at intermediate angles. The intensity of this peak increases as the sample is cooled from 250 ºC, but

interestingly, starts decreasing below 150 ºC. Concomitantly, two diffuse maxima, one at the same angle as this peak, and another at a slightly lower angle are developed (inset A of Figure 2.5). The spacing corresponding to peaks at the lowest and intermediate angle are in the ratio of 1: 1/√7. Generally, for a hexagonal columnar packing, the ratio of the spacing of the small-angle peaks should be 1: 1/√3: 1/2: 1/√7 etc.[72] However, for ***C*$_3$OPV1**, if one wants to choose the indexing to be for a hexagonal lattice, the second (1/√3) and third peaks (1/2) should be presumed to be missing. Even if one considers that the diffuse peak at ~ 2θ = 3.5º contains a sharp peak, the 1/√3 ratio peak would still be missing. It may be recalled that there has been a report [73] wherein such a feature of certain peaks were found missing. In the present case, we can perhaps attribute it to the helical packing of the benzenetrisamide units by a three-fold H-bonding interaction. An alternate stand that could be taken is that the diffraction pattern arises from a rectangular lattice. This corroborates the OPM observations mentioned above, and we tend to take this situation to be true, and thus the results of the measured and calculated *d*-spacing, miller indices and lattice parameters summarized in Table 2.1, reflect this choice. The effect of temperature on the lowest angle (1 0) peak is shown in the Figure 2.6. On lowering the temperature, the spacing increases from 4.70 to 5.02 nm reaching a saturating value around room temperature. This can be explained by the conformational stabilization of the peripheral alkyl chains owing to their negative thermal expansion.

A feature depicted in the inset A of Figure 2.5 that needs to be commented is the weakening of the lattice reflections – specifically the (21) peak – on cooling the

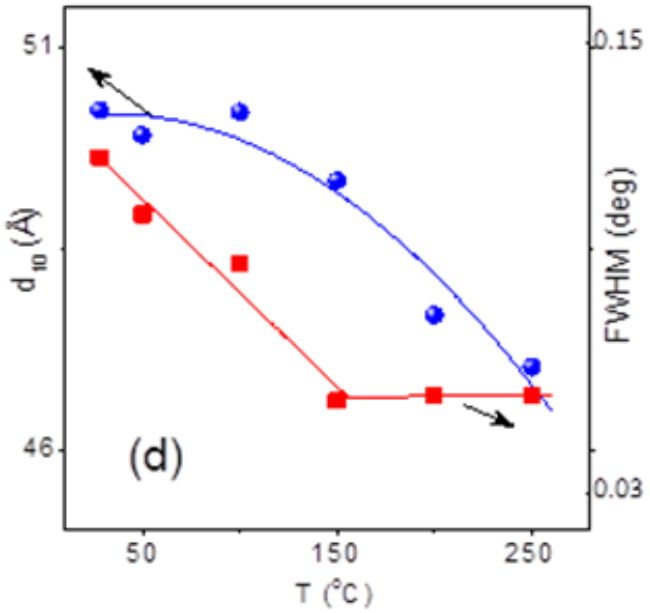

Figure 2.6. Variation of (1 0) peak *d*-space value with different temperatures.

sample below 150 ° C. This is surprising since at least till room temperature, the mesophase remains the same. Even if there is a transition to a disordered phase, it is difficult to imagine that any pre-transition effect would be spread over such a large temperature range. A possibility that we would like to propose is the following. At high temperatures (T >150 ºC), the chains which would have significant gauche conformations owing to the substantial free space available, may still permit a slightly better interaction between the cores of the neighbouring molecules in the column. At lower temperatures, when the chains are quite stretched adopting the all-trans conformation, a secondary effect may start dominating: the three-fold H-bonding interaction between the adjacent molecules in the column leading to a packing of the molecules in such a way that there is an angle of twist between them.[73] Such a requirement would weaken the lattice ordering resulting in lower

Table 2.1. Temperature-dependent XRD data of the columnar LC phase of ***C*$_3$OPV1**, presenting the measured and calculated spacing, miller indices and lattice parameters.

Temp. (°C)	d_calc (Å)		h	k	Columnar Rectangular Parameters	
					aR (Å)	bR (Å)
250	47.03	47.03	1	0	47.03	27.39
	17.84	17.84	2	1		
	Diffuse 17.69					
	Diffuse 4.77					
200	47.67	47.67	1	0	47.67	27.64
	18.05	18.05	2	1		
	Diffuse 17.38					
	Diffuse 4.77					
150	49.33	49.33	1	0	49.33	28.83
	24.89	24.89	1	1		
	18.70	18.74	2	1		
	Diffuse 17.98					
	Diffuse 4.60					
100	50.18	50.18	1	0	50.18	29.74
	25.59	25.59	1	1		
	18.97	19.18	2	1		
	Diffuse 17.34					
50	49.89	49.89	1	0	49.89	29.60
	25.46	25.46	1	1		
	18.88	19.08	2	1		
	Diffuse 17.29					
28 (rt)	50.21	50.21	1	0	50.21	30.00
	25.76	25.76	1	1		
	18.92	19.25	2	1		
	Diffuse 17.27					
	Diffuse 4.43					

intensity for the reflections with higher Miller indices, and also broaden the peaks, clearly seen from the width of the (10) peak (Figure 2.6).

2.3.3. Self-Assembly of *C*$_3$OPV1, *C*$_3$OPV2 and *C*$_3$OPV3

In order to understand the self-assembly of the molecules, the absorption and emission spectra of all the three molecules were monitored in different solvents. The details are tabulated in Table 2.2. The absorption spectra of ***C*$_3$OPV1** (10^{-4} M) in both THF and toluene showed almost similar spectral features with maxima around 380 nm in both cases (Figure 2.7a). Furthermore, the temperature-dependent absorption spectra in toluene did not show any changes when the temperature increased from 20 to 90 °C. For ***C*$_3$OPV2**, the absorption spectrum in THF (10^{-4} M) was found to be similar to the absorption spectrum of ***C*$_3$OPV1** in THF with the absorption maximum at 380 nm (Figure 2.7b). On the other hand, the absorption spectrum of ***C*$_3$OPV2** in toluene (10^{-4} M) showed blue-shifted (10 nm) absorption with the maximum at 370 nm (Figure 2.7c). In the case of ***C*$_3$OPV3**, the absorption maximum in THF (10^{-4} M) was found to be at 370 nm. The blue-shift in the absorption maximum of ***C*$_3$OPV3** in THF when compared to the other two molecules can be due to the absence of an alkoxy group in the *para* position of the

Table 2.2. The absorption and emission spectral details of ***C*$_3$OPV1**, ***C*$_3$OPV2** and ***C*$_3$OPV3**. The concentration of the solution is 10^{-4} M.

Solvent	***C*$_3$OPV1** (λ_{max} in nm)		***C*$_3$OPV2** (λ_{max} in nm)		***C*$_3$OPV3** (λ_{max} in nm)	
	Abs.	Em.	Abs.	Em.	Abs.	Em.
THF	380	435	380	431	370	436
Toluene	380	435	370	504	360	436

terminal benzene ring of the OPV unit. As in the case of ***C*$_3$OPV2**, the absorption maximum of ***C*$_3$OPV3** in toluene (10^{-4} M) also showed a blue-shift of 10 nm. In spite of this blue-shift, both ***C*$_3$OPV2** and ***C*$_3$OPV3** displayed an additional shoulder band at longer wavelengths (425 nm), which disappeared at higher temperatures. From the absorption features of the molecules in THF and toluene, it is evident that the ***C*$_3$OPV2** and ***C*$_3$OPV3** could form self-assembly in toluene, whereas it is less obvious in the case of ***C*$_3$OPV1**.

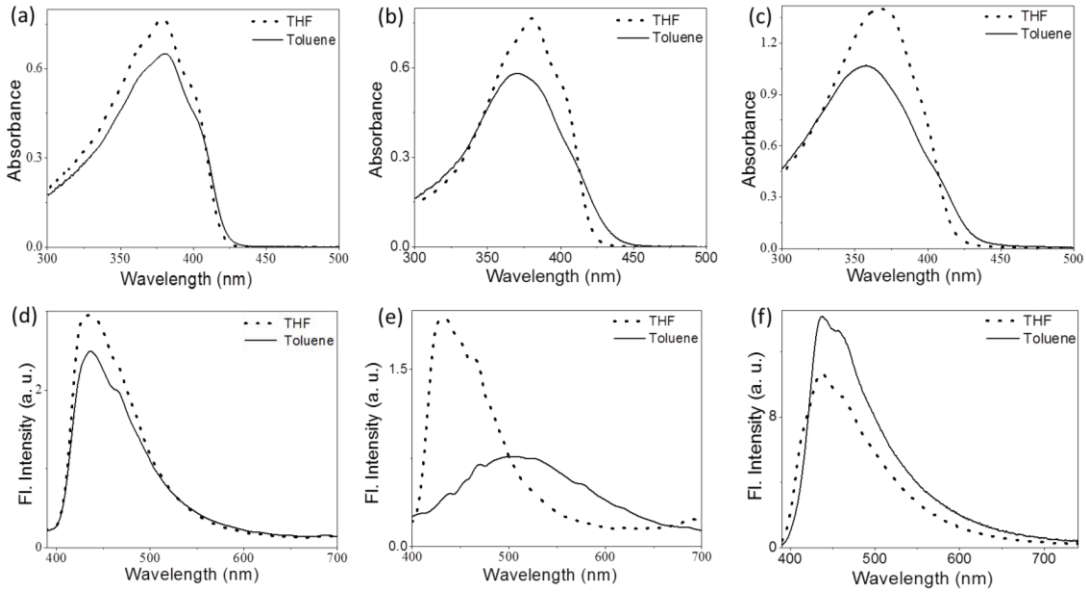

Figure 2.7. Absorption spectra of (a) ***C*$_3$OPV1**, (b) ***C*$_3$OPV2** and (c) ***C*$_3$OPV3** in THF and toluene (10^{-4} M). The emission spectra of (d) ***C*$_3$OPV1**, (e) ***C*$_3$OPV2** and (f) ***C*$_3$OPV3** in THF and toluene (10^{-4} M), λ_{ex} = 375 nm.

To understand the mechanism of the self-assembly process, temperature-dependent absorption studies were carried out. A 10^{-4} M solution of the compound in toluene was used for the studies. The absorption corresponding to the aggregation band at 425 nm was monitored as a function of temperature. The fraction of aggregates (α_{agg}) was then plotted against temperature. Figure 2.8 shows comparison

of the melting transition curves obtained for ***C*$_3$OPV1**, ***C*$_3$OPV2** and a mixture of 10% ***C*$_3$OPV1** and ***C*$_3$OPV1**. The melting transition temperature, T_m (the temperature at which the α_{agg} is 50%) for ***C*$_3$OPV1** is 310.8 K and that for ***C*$_3$OPV2** is 321.5 K (Figure 2.8a and b).

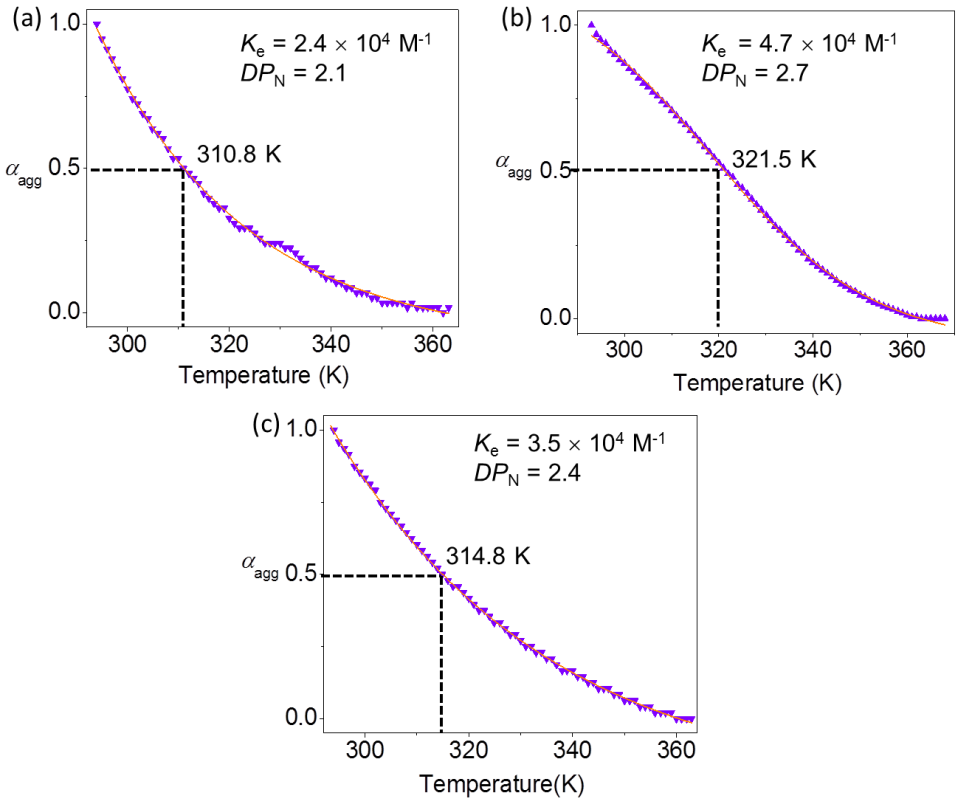

Figure 2.8. Plots of the fraction of aggregates (α_{agg}) *versus* temperature for (a) ***C*$_3$OPV1**, (b) ***C*$_3$OPV2** and (c) 10% (v/v) of ***C*$_3$OPV2** in ***C*$_3$OPV1**. Absorbance was monitored at 425 nm with a rate of cooling of 1 K min^{-1}. (▼ is the normalized spectra and — is the curve fit). The value of association constant (K_e) and degree of polymerization (DP_N) are given in the inset.

This difference in the T_m values indicates that ***C*$_3$OPV2** forms stronger assembly than the ***C*$_3$OPV1**. In order to study the effect of ***C*$_3$OPV2** on the self-assembly of ***C*$_3$OPV1** we have added a 10% (v/v) of 10^{-4} M ***C*$_3$OPV2** solution to ***C*$_3$OPV1** and the absorbance at 425 nm was monitored as the function of temperature. The

melting transition temperature was found to increase from 310.8 K to 314.8 K. This experiment clearly shows that the presence of ***C*$_3$OPV2** molecules increases the stability of the co-assembly formed by ***C*$_3$OPV1** (Figure 2.8c).

From the plot of α_{agg} versus temperature (Figure 2.8), it is clear that all the molecules aggregate via isodesmic mechanism in which the binding constant for each addition of monomer to the growing assembly is the same.[74] The temperature dependent absorption spectrum of ***C*$_3$OPV1** and ***C*$_3$OPV2** is then fitted with the isodesmic or the equal-K model. Standard isodesmic model is used for analyzing the data.[74] According to this model the degree of polymerization or the molar fraction of aggregated species $\alpha_{agg}(T)$ is given by the equation (2.1).

$$\alpha_{agg}(T) \cong \frac{1}{1+\exp\left(-0.908\Delta H\frac{T-T_m}{RT_m{}^2}\right)} \qquad (2.1)$$

By using equation (2.1), $T_{m,}$ the melting temperature is defined as the temperature for which α_{agg} = 0.5 and ΔH, the molar enthalpy release related to the formation of noncovalent intermolecular interactions were determined. The number-averaged degree of polymerization DP_N can be calculated from $\alpha_{agg}(T)$:

$$DP_N = \frac{1}{\sqrt{1-\alpha_{agg}(T)}} \qquad (2.2)$$

This expression can be related to the equilibrium constant K and the total concentration of molecules C_T via:

$$DP_N = \frac{1}{\sqrt{1-\alpha_{agg}(T)}} = \frac{1}{2} + \frac{1}{2}\sqrt{4K_e(T)C_T + 1} \qquad (2.3)$$

The thermodynamic parameters are calculated by applying the isodesmic model and are summarized in Table 2.3.

Table 2.3. Thermodynamic parameters for the self-assembly of ***C*$_3$OPV1**, ***C*$_3$OPV2** and a mixture of 10% ***C*$_3$OPV2** and ***C*$_3$OPV1** obtained using the isodesmic model. Concentration is kept at 0.1 mM.

Molecule	ΔH (KJ mol^{-1})	ΔS (J mol^{-1} K^{-1})	ΔG (KJ mol^{-1})	T_m (K)	K_e (10^4 M^{-1})	DP_N
***C*$_3$OPV1**	-103.75	-248.67	-29.35	310.8	2.4	2.1
***C*$_3$OPV2**	-85.10	-194.5	-26.75	321.4	4.7	2.7
10 % ***C*$_3$OPV2** and ***C*$_3$OPV1**	-97.28	-237.44	-26.18	314.8	3.5	2.4

ΔH the change in enthalpy, ΔS the change in entropy, ΔG the change in free energy, T_m the melting transition temperature, K_e the association constant and DP_N is the degree of polymerization.

Subsequently, we studied the fluorescence properties of ***C*$_3$OPV1-3** (10^{-4} M). For ***C*$_3$OPV1**, the emission maximum in both toluene and THF remains almost same at 435 nm. However, the emission intensity was found to be less in the case of toluene (Figure 2.7d). In THF, ***C*$_3$OPV2** showed an emission maximum at 431 nm and in toluene, the emission maximum displayed a red shift of 70 nm (λ_{max} = 504 nm) with broadening of the spectrum (Figure 2.7e). Quenching of fluorescence was also observed with the broadening. This quenching and broadening are due to the formation of supramolecular assembly of ***C*$_3$OPV2** in toluene. The ***C*$_3$OPV3** molecule showed almost similar emission features both in toluene and THF with slightly higher emission intensity in toluene (Figure 2.7f).

Then, we studied the self-assembly properties of ***C*$_3$OPV1** molecule in THF-water system (Figure 2.9). As the composition of water is increased, the red-shifted shoulder band, characteristic for the formation of aggregates were started to appear, which disappeared upon increasing temperature (Figure 2.9a). In THF-water

mixture, the emission intensity was found to be high for the aggregates and the variable temperature emission studies of ***C*$_3$OPV1** in THF-water mixture established the aggregation induced enhanced emission property of the molecule. As the temperature decreased, the emission of ***C*$_3$OPV1** showed an enhancement in intensity (Figure 2.9b).

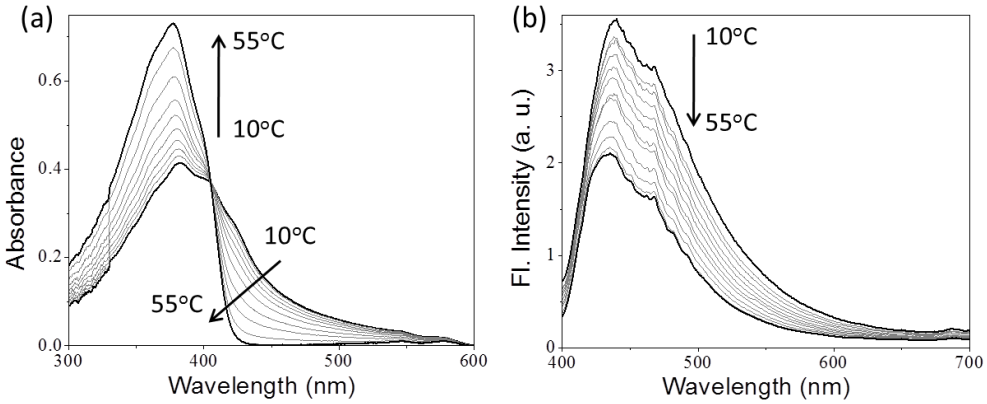

Figure 2.9. Temperature-dependent (a) absorption and (b) emission (λ_{ex} = 375 nm) spectra of ***C*$_3$OPV1** in 25% water-THF mixture (5×10^{-5} M).

To understand the nature of interaction between the molecules and with the solvents, and to understand the nature of the assembly formed in these solvents, detailed morphological studies were carried out. In the case of nonpolar solvents, the molecule-solvent interactions are minimum, and hence the molecule-molecule non-covalent forces may play a major role in the self-assembly of molecules. The morphological studies were carried out on mica surface. ***C*$_3$OPV1** formed very week assembly in toluene due to competing solvent-molecule interactions resulting in spherical particles of size around 220 nm at a concentration of 10^{-4} M (Figure 2.10a). At the same concentration, ***C*$_3$OPV2** in toluene formed highly intertwined fibers of micrometer length with a diameter of approximately 250 nm (Figure

2.10b). Formation of these extended assemblies can be due to the long-range interaction of molecules via various non-covalent forces such as H-bonding, π-stacking and van der Waals interactions. On the other hand, ***C*$_3$OPV3** fails to form such an extended assembly; instead it formed spherical particles of size around 210 nm (Figure 2.10c).

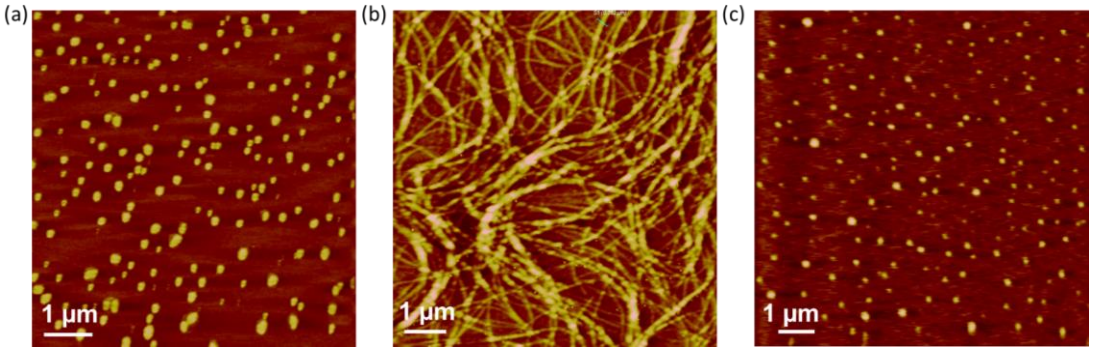

Figure 2.10. Atomic force microscopic images (AFM) of (a) ***C*$_3$OPV1**, (b) ***C*$_3$OPV2** and (c) ***C*$_3$OPV3** aggregates in toluene (1 x 10^{-4} M) dropcast on mica surface.

The spherical particle size distribution of both ***C*$_3$OPV1** and ***C*$_3$OPV3** are given in Figure 2.11. In the case of ***C*$_3$OPV1**, the size of the particle varies from 150-300 nm with maximum number of particles having an average size of 220 nm (Figure 2.11a). Similarly, for ***C*$_3$OPV3**, the size distribution is almost similar to that of ***C*$_3$OPV1** with an average size of 210 nm (Figure 2.11b).

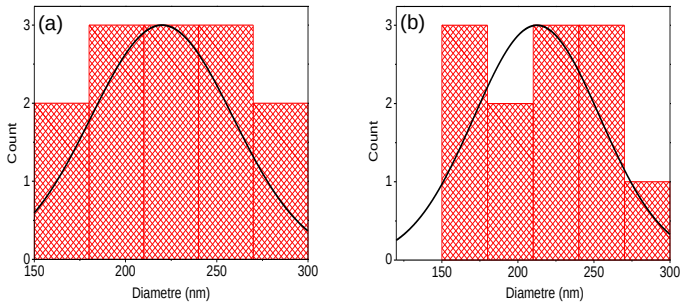

Figure 2.11. Histogram showing the size distribution of spherical particles formed by (a) ***C*$_3$OPV1** and (b) ***C*$_3$OPV3**.

The gelation properties of these molecules were then studied and found that only ***C*$_3$OPV2** was able to form gel (Table 2.4). The other two molecules failed to form gel in any of the solvents tested. ***C*$_3$OPV2** was able to form gel in toluene, *n*-decane, cyclohexane, methylcyclohexane, etc. As in the case of other C_3-symmetrical molecules, ***C*$_3$OPV2** needs very high concentration to form the gel.[75] The critical gelator concentration (CGC) for ***C*$_3$OPV2** in toluene is 4.65 mM. In cyclohexane and methylcyclohexane, the CGC is found to be 14 mM, which is almost more than three times that required for the gelation in toluene. Furthermore, a solvent dependent difference in the nature of the gel was noticed. In toluene, a transparent gel was formed while in other solvents gels were found to be opaque (Figure 2.12a-d). The lack of gelation property of ***C*$_3$OPV1** and ***C*$_3$OPV3** can be rationalized on the basis of their morphology. Gelation is basically the entrapment of solvents inside a three-dimensional (3D) solid matrix of interconnected network of fibers.[76] Morphological studies revealed that ***C*$_3$OPV2** is capable of forming such self-assembled structures (Figure 2.11b and Figure 2.12e). However, the other two molecules, i.e., ***C*$_3$OPV1** and ***C*$_3$OPV3** were unable to form 1D fibers assembly (Figure 2.11a and Figure 2.11c). The spherical particles formed in the case of ***C*$_3$OPV1** and ***C*$_3$OPV3** could not entrap solvent molecules and therefore gelation was not observed.

The lack of self-assembly of ***C*$_3$OPV1** in toluene can be due to the presence of nine alkyl chains around the central C_3 core, which give high solubility for the molecule in this solvent. In the case of THF-water mixture, it is the hydrophobic interaction between the molecules and solvent causes the molecule to form

Table 2.4. Behavior of ***C*$_3$OPV1**, ***C*$_3$OPV2** and ***C*$_3$OPV3** in different solvents. Critical gelation concentration (mM) is shown in bracket.

Molecule	Cyclohexane	Methyl cyclohexane	*n*-Decane	Toluene
***C*$_3$OPV1**	S	S	S	S
***C*$_3$OPV1**	G(14.86)	G(13.94)	G(9.29)	G(4.65)
***C*$_3$OPV1**	S	S	S	S

Where, S = Soluble, G = Gel

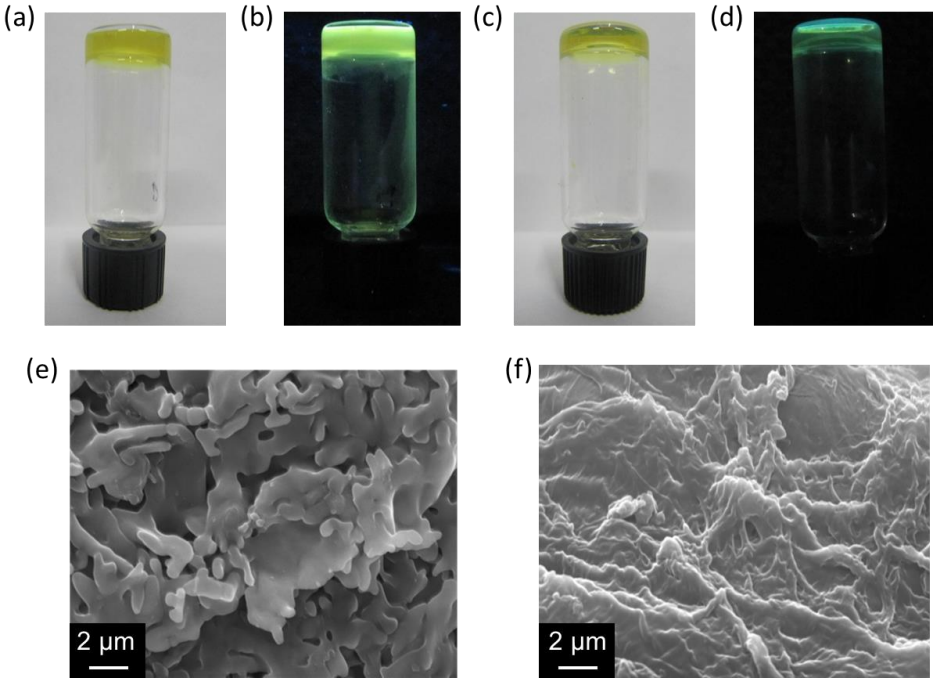

Figure 2.12. Photograph of ***C*$_3$OPV2** gel formed in (a) and (b) *n*-decane and (c) and (d) in toluene under normal light and under UV-light (λ_{ex} = 365 nm), respectively. (e) and (f) Scanning electron microscope (SEM) image of ***C*$_3$OPV2** *n*-decane and toluene gel, respectively.

self-assembly. At the same time, when one of the alkyl chains from each arm of the ***C*$_3$OPV1** is removed, as in the case of ***C*$_3$OPV3** or as in the case of ***C*$_3$OPV2**, (in both cases the molecule with total of six alkyl chains) the solubility in toluene and

other non-polar solvents will be reduced, forcing the molecule to form assembly via H-bonding, π-π stacking and van der Waals interaction.

2.4. Conclusions

The rational design of molecules with delicate structural differences leads to molecules with extremely contrasting properties. In the present study, we have demonstrated one such example of structural engineering, which leads to the formation of mesophase and organogel. We have synthesized three C_3-symmetrical OPV molecules, and their liquid crystalline and organogelation properties were studied in detail. The self-assembly of these three molecules are entirely different in different states. In solution, ***C*$_3$OPV1** and ***C*$_3$OPV3** fail to form any kind of extended assembly, whereas ***C*$_3$OPV2** form self-assembly in non-polar solvents. Both ***C*$_3$OPV1** and ***C*$_3$OPV3** forms spherical morphology and ***C*$_3$OPV2** forms extended 3D network of nanofibers. Self-assembly of ***C*$_3$OPV1** can be induced by adding small amount of ***C*$_3$OPV2**. ***C*$_3$OPV1**, the molecule with nine alkoxy chains at the periphery of the disc shows mesomorphic properties even at room temperature and the LC phase is identified as columnar phase with 2-D rectangular lattice. As the number of alkoxy chains at the periphery decreases the LC properties disappears. When the number of alkoxy chain decreases to six, ***C*$_3$OPV2** is able to gelate organic solvents. ***C*$_3$OPV3** even though had a total of six alkoxy chains, could neither form gel nor shows any liquid crystalline properties.

2.5. Materials and Methods

2.5.1. General

Unless otherwise stated, all starting materials and reagents were purchased from commercial suppliers and used without further purification. The solvents were purified and dried by standard methods prior to use. Reactions were monitored using thin layer chromatography (TLC) on silica gel 60 F_{254} (0.2 mm; Merck). Visualization was accomplished using UV lamp (365 nm). Column chromatography was performed on glass columns of different sizes hand packed with silica gel 60 (particle size 0.040–0.063 mm, Merck). Molecules ***C*$_3$OPV1-3** were synthesized according to Scheme 2.1 and 2.2 based on standard protocols.

2.5.2. Instrumentation

NMR spectra were measured on a 300 or 500 MHz Bruker Avance DPX spectrometer. Chemical shifts are reported in parts per million (ppm) using tetramethylsilane (TMS) (δ_H = 0 ppm) as an internal reference. The resonance multiplicity is described as s (singlet), d (doublet), t (triplet) and m (multiplet). Mass spectra (MS) were recorded on a JEOL JSM 600 fast atom bombardment (FAB) high-resolution mass spectrometer. Matrix-assisted laser desorption ionization time-of-flight (MALDI-TOF) mass spectra were obtained on a Shimadzu AXIMA-CFR PLUS spectrometer using α-cyano-4-hydroxycinnamic acid as the matrix. The electronic absorption spectra were recorded on a Shimadzu UV-3101 or 2401PC UV-Vis-NIR scanning spectrophotometer. The fluorescence spectra were recorded on a SPEX-Fluorolog F112X spectrofluorimeter. AFM images were

recorded under ambient conditions using a NTEGRA (NT-MDT) operating with a tapping mode regime. Micro-fabricated TiN cantilever tips (NSG10) with a resonance frequency of 299 kHz and a spring constant of S8 20-80 Nm^{-1} was used. Samples for the imaging were prepared by drop casting the required solution (1×10^{-4} M) prepared in toluene on freshly cleaved mica surface after drying in vacuum. SEM images were taken on a Zeiss EVO 18 cryo SEM Special Edn with variable pressure detector working at 20–30 kV after sputtering with gold. Gel samples were prepared after drop casting on freshly cleaved mica substrate. It was kept for overnight to allow slow evaporation of the solvent and further dried in a vacuum desiccator for 12 h. Liquid crystalline phase transitions and optical anisotropy were observed using a Leica DFC 490 polarized light optical microscope, equipped with a Mettler TOLEDO FP82HT (Temperature programmer) heating and freezing stage. Temperature depend X-ray diffraction studies at liquid crystalline phases were carried out on samples filled in Lindemann capillaries and were held at required temperatures using a Mettler hot stage and irradiated with Cu K_α radiation (λ = 1.5418 Å). The apparatus essentially involved a high-resolution X-ray powder diffractometer (PANalytical X'Pert PRO) equipped with a high-resolution fast detector, PIXCEL.

2.5.3. Gelation Studies

A weighed amount of the compound in an appropriate solvent was placed in a glass vial, which was sealed and heated until the compound was dissolved. The solution was allowed to cool to room temperature. The gel formation was confirmed by the

failure of the gel mixture to flow by inverting the glass vial. The thermoreversibility of the gelation was confirmed by repeated heating and cooling.

2.6. Synthesis and Characterization

2.6.1. Preparation of 4-bromomethyl-benzonitrile (3)

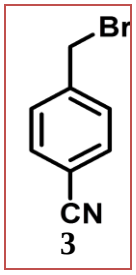

3

To a solution of 4-methyl-benzonitrile (**2**) (1 g, 8.32 mmol) in 30 mL of dry carbon tetrachloride was added *N*-bromosuccinimide (1.77 g, 10 mmol) and AIBN. The reaction mixture was refluxed for 8 h. The hot solution was then filtered, concentrated and kept overnight for recrystallization and the product obtained was filtered and dried. **Yield**: 90%; **m.p.** 113-116 °C; **^{1}H NMR** (300 MHz, $CDCl_3$, TMS) δ: 7.63-7.68 (m, 2H), 7.26-7.51 (m, 2H), 4.48 (s, 1H) ppm; **MS-FAB** (m/z): $[M+H]^+$ calculated for C_8H_6BrN is 197.04; found 196.07.

2.6.2. Preparation of 4-bromomethyl-benzaldehyde (4)

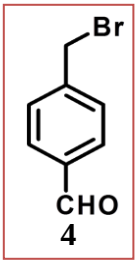

4

Compound **3** (4-(bromomethyl)benzonitrile) (1 g, 5.1 mmol) was dissolved in 10 mL of toluene and cooled at 0 ºC. A portion of 1.08 M DIBAL-H in *n*-hexane (2 eq.) was added drop wise under Nitrogen atmosphere. The solution was stirred for another hour at 0 ºC. Chloroform was added then followed by 10% hydrochloric acid and the solution was stirred at room temperature for another 1 h. The organic layer was separated, washed with distilled water and dried over anhydrous sodium sulphate and filtered. The solvent was almost completely removed from the filtrate under reduced pressure and the residue was cooled, filtered, washed with cold *n*-hexane and dried at 50 ºC under vacuum. **Yield**: 70%; **m.p.** 97-100 °C; **^{1}H NMR** (300 MHz,

$CDCl_3$, TMS) δ: 10.02 (s, 1H), 7.86 (m, 2H), 7.57 (m, 2H), 4.52 (s, 2H) ppm; **MS-FAB** (m/z): $[M+H]^+$ calculated for C_8H_7BrO is 200.04; found 200.76.

2.6.3. Preparation of 2-(4-bromomethyl-phenyl)-5,5-dimethyl-[1,3]dioxane (5)

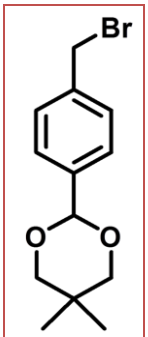

5

Compound **4** (4-(bromomethyl)benzaldehyde) (500 mg, 1 mmol), 2,2-dimethyl-1,3-propandiol (300 mg, 2.88 mmol) and catalytic amount of pyridinium hydrochloride were dissolved in dry benzene. The solution was then refluxed for 8 h at 100 ºC. Water formed in the reaction mixture was separated from benzene using a dean-stark set-up. After the completion of the reaction, the excess benzene was distilled off and the residue was dissolved in dichloromethane. The compound was then extracted, dried over anhydrous sodium sulphate. The product, a colorless oily solid was further purified using column chromatography over silica gel (30% $CHCl_3$-*n*-hexane). **Yield**: 80%; **^{1}H NMR** (300 MHz, $CDCl_3$, TMS) δ: 7.61-7.49 (m, 2H), 7.41-7.38 (m, 2H), 5.39 (s, 1H), 4.59 (s, 2H), 3.79-3.63 (dd, 4H), 1.29 (s, 3H), 0.80 (s, 3H) ppm; **MS-FAB** (m/z): $[M+H]^+$ calculated for $C_{13}H_{17}BrO_2$: 286.18; found 287.5.

2.6.4. Preparation of [4-(5,5-dimethyl-[1,3]dioxan-2-yl)-benzyl]-phosphonic acid diethyl ester (6)

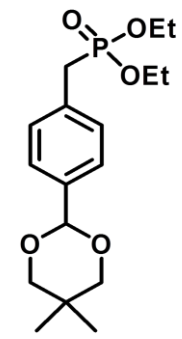

6

A mixture of triethyl phosphite (2.0 mL, 11.6 mmol) and **5** (1.25 g, 5.1 mmol) was heated at 160 °C. The generated bromoethane was distilled off, as was the excess triethyl phosphite after a reaction time of 1 h, and the residue was purified by column chromatography over basic alumina using EtOAc as eluent.

Yield: 90%; **^{1}H NMR** (300 MHz, $CDCl_3$, TMS) δ: 7.46-7.43 (d, 2H), 7.31-7.28 (d, 2H), 5.37 (s, 1H), 4.13-3.96 (q, 4H), 3.78-3.62 (m, 4H), 3.18-3.11 (d, 2H), 1.36-1.21 (t, 6H), 0.79 (s, 6H) ppm; **MS-FAB** (m/z): $[M+H]^+$ calculated for $C_{17}H_{27}O_5P$ is 343.37; found 342.16.

2.6.5. Preparation of 3,4,5-tris-dodecyloxy-benzaldehyde (8a)

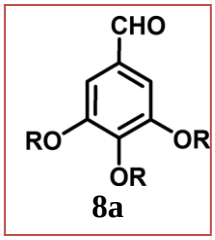

8a

A mixture of 3,4,5-trihydroxy benzaldehyde (2 g, 13 mmol) and potassium carbonate (5 g) was mixed well. 1-Bromododecane (18.71 mL, 77 mmol) was added drop wise and the reaction mixture was heated at 70 ºC for 10 h with stirring. It was cooled to room temperature and poured into ice water. The precipitate formed was then filtered. The crude precipitate was passed through a column of silica gel using 5% ethyl acetate-hexane as the eluent. The product was precipitated by adding methanol into a concentrated solution of dichloromethane. **Yield**: 94%; **m.p.** 50-52 °C; **^{1}H NMR** (300 MHz, $CDCl_3$, TMS) δ: 9.83 (s, 1H), 7.08 (s, 2H), 4.06-4.01 (m, 6H), 1.83-1.75 (m, 6H), 1.48-1.26 (m, 54H), 0.88-0.86 (t, 9H) ppm; **MS-FAB** (m/z): $[M+H]^+$ calculated for $C_{43}H_{78}O_4$ is 659.59; found 659.48.

2.6.6. Preparation of 5,5-dimethyl-2-{4-[2-(3,4,5-tris-dodecyloxy-phenyl)-vinyl]-phenyl}-[1,3]dioxane (9a)

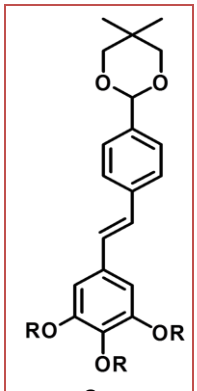

9a

The compound **8a** (400 mg, 0.65 mmol) and the compound **6** (diethyl 4-(2,2-dimethyl-1,3-dioxan-5-yl)benzylphosphate) (350 mg, 1.2 mmol) were taken in a two-neck round bottom flask purged with argon. Dry THF was then added to the flask. Sodium hydride was then added to the reaction mixture. The mixture was

stirred overnight at room temperature, extracted with chloroform and dried over anhydrous sodium sulphate. The product thus obtained was purified by reprecipitation by adding excess methanol into concentrated chloroform solution. The resulting product was further purified by column chromatography over silica gel using 40% $CHCl_3$-*n*-hexane as an eluent.

Yield: 83%; **m.p.** 62-65 °C; **^{1}H NMR** (300 MHz, $CDCl_3$, TMS) δ: 7.46-7.16 (m, 4H), 6.96-6.84 (m, 2H), 6.6 (s, 2H), 5.32 (s, 1H), 3.95-3.86 (m, 6H), 3.7-3.45 (m, 4H), 1.64-1.21 (m, 60H), 0.82-0.81 (t, 9H), 0.79 (s, 3H) ppm; **MS-FAB** (m/z): $[M+H]^+$ calculated for $C_{56}H_{94}O_5$ is 848.34; found 847.7.

2.6.7. Preparation of 4-[2-(3,4,5-tris-dodecyloxy-phenyl)-vinyl]-benzaldehyde (10a)

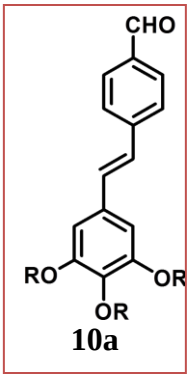

10a

Compound **9a** and trifluoroacetic acid in dichloromethane was stirred at room temperature for 2 h. The organic layer was then washed with water dried over anhydrous sodium sulphate and evaporated to dryness. The product was then purified by column chromatography over silica gel using 30% $CHCl_3$-hexane as eluent. **Yield**: 92%; **m.p.** 48-51 °C; **^{1}H NMR** (300 MHz, $CDCl_3$, TMS) δ: 9.99 (s, 1H), 7.88-7.85 (d, 2H), 7.65-7.62 (d, 2H), 7.19-6.98 (m, 2H), 6.74 (s, 2H), 4.05-3.96 (t, 6H), 1.83-1.75 (m, 6H), 1.48-1.26 (m, 58H), 0.88-0.86 (t, 9H) ppm; **MS-FAB** (m/z): $[M+H]^+$ calculated for $C_{51}H_{84}O_4$ is 762.21; found 762.4.

2.6.8. Preparation of 1,2,3-tris-dodecyloxy-5-(2-{4-[2-(4-nitro-phenyl)-vinyl]-phenyl}-vinyl)-benzene (11a)

To a mixture of the compound **10a** (80 mg, 0.1 mmol) and the compound (diethyl 4-nitrobenzylphosphonate) (82 mg, 0.3 mmol) in a two-necked round bottom flask,

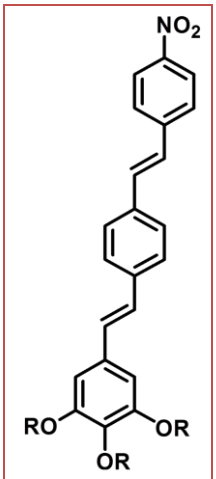

11a

argon was purged. The compounds were then dissolved in dry THF and sodium hydride was added.The reaction mixture was then stirred for 2 h. After checking the completion of the reaction by TLC, the reaction mixture was extracted using chloroform and washed with water for several time. The combined extracts were then dried over anhydrous sodium sulphate. The product thus obtained was purified by reprecipitation by adding excess methanol into a concentrated chloroform solution. The resulting product was further purified by column chromatography over silica gel using 30% $CHCl_3$-*n*-hexane as an eluent. **Yield**: 83%; **m.p. 70**-72 °C; **^{1}H NMR** (300 MHz, $CDCl_3$, TMS) δ: 8.28-8.21 (m, 2H), 7.71-7.63 (m, 2H), 7.53 (s, 4H), 7.18-7.1 (m, 2H), 7.04-6.95 (m, 2H), 6.73 (s, 2H), 4.05-3.98 (t, 6H), 1.83-1.76 (t, 6H), 1.56-1.27 (m, 57H), 0.881-0.86 (t, 9H) ppm; **MS-FAB** (m/z): $[M+H]^+$ calculated for $C_{58}H_{89}NO_5$ is 881.33; found 882.1.

2.6.9. Preparation of 4-(2-{4-[2-(3,4,5-tris-dodecyloxy-phenyl)-vinyl]-phenyl}-vinyl)-phenylamine (12a)

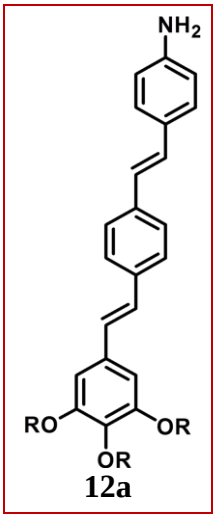

12a

The OPV nitro compound **11a** and stannous chloride in THF containing four drops of 37% hydrochloric acid was refluxed at 70 °C for 4 h. The reaction mixture was then diluted with 50 mL dichloromethane and washed once with 0.1 M sodium bicarbonate solution and two times with water. The organic layer was then filtered through a silica pad using dichloromethane as the eluent to afford the amino compound. The product was then

precipitated using methanol after dissolving it in dichloromethane. **Yield**: 80%; **m.p.** 55-58 °C; **^{1}H NMR** (300 MHz, $CDCl_3$, TMS) δ: 7.5-7.28 (m, 4H), 7.19-7.07 (m, 2H), 7.04-6.88 (m, 3H), 6.81-6.79 (m, 3H), 6.4-6.38 (d, 2H), 4.69 (s, 2H), 3.99-3.9 (t, 6H), 1.83-1.76 (t, 6H), 1.51-1.3 (m, 57H), 0.88-0.87 (t, 9H) ppm; **MS-FAB** (m/z): $[M+H]^+$ calculated for $C_{58}H_{91}NO_3$ is 851.35; found 852.1.

2.6.10. Preparation of *C*$_3$OPV1

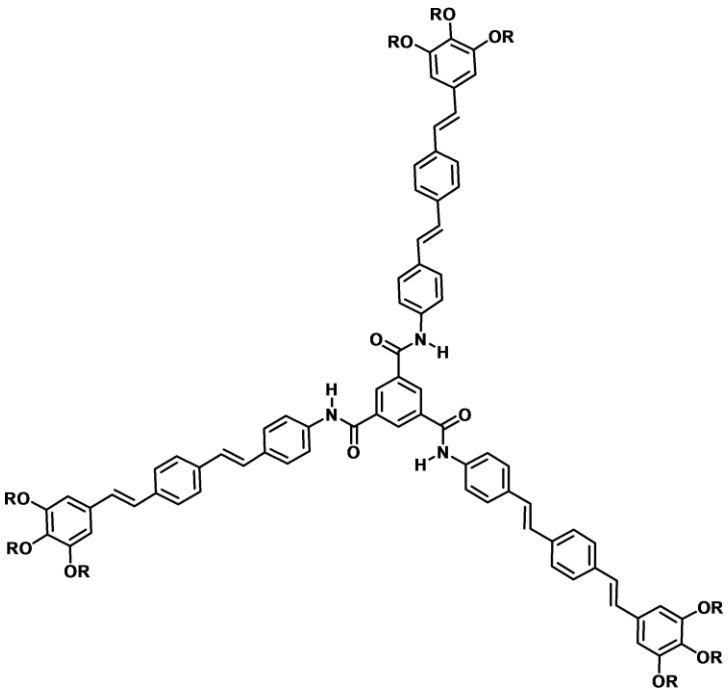

***C*$_3$OPV1**

To a solution of **12a** (200 mg, 0.15 mmol) and triethylamine (0.5 mL) in dry dichloromethane (10 mL) a solution of 1,3,5-benzenetricarboxylic acid chloride (11.8 mg, 0.045 mmol) was added dropwise. The mixture was stirred for 6 h and the solvent was evaporated *in vacuo.* The residue was then extracted using dichloromethane and washed with water for several time. Purification by column

chromatography over silica gel (dichloromethane–*n*-hexane 3:1) and BioBeads SX-1 (dichloromethane) yielded pure ***C*$_3$OPV1**.

Yield: 45%; **m.p.** > 260 °C; **^{1}H NMR** (300 MHz, THF-d_8) δ: 11.14 (s, 3H), 10.21 (s, 3H), 8.78 (s, 3H), 7.91-7.53 (m, 18H), 7.19-7.04 (m, 18H), 6.82 (s, 3H), 4.02-3.82 (m, 18H), 1.77-1.31 (m, 180H) 0.89 (s, 27H) ppm; **^{13}C NMR** (125 MHz, $CDCl_3$): δ = 13.8, 23.7, 25.4, 29.9, 30.2, 32.4, 69.6, 118.3, 124.7, 126.8, 127.4, 129.2, 129.3, 133.2, 134.7, 137.2, 147.5, 165.2 ppm; **MALDI-TOF-MS**: m/z calculated for $C_{183}H_{273}N_3O_{12}$ [M^+] is 2707.14; found: 2707.63.

Synthesis of *C*$_3$OPV2

2.6.11. Preparation of 3,4 -bis-dodecyloxy-benzaldehyde (8b)

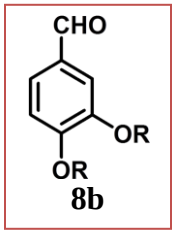

8b

A mixture of 3,4,-dihydroxy benzaldehyde (0.5 g, 3.62 mmol) and potassium carbonate (5 g) was mixed well in dry DMF. 1-bromododecane (2.17 g, 8 mmol) was added drop wise and stirred at 70 °C for 10 h. The reaction mixture was cooled to room temperature and poured into ice water. The precipitate formed was filtered. The crude product was then passed through a column of silica gel using 5% ethyl acetate-hexane as the eluent. Finally, the product was precipitated by adding methanol into concentrated dichloromethane solution. **Yield**: 95%; **m.p.** 70-73 °C; **^{1}H NMR** (300 MHz, $CDCl_3$, TMS): δ: 9.83 (s, 1H), 7.42-7.40 (m, 2H), 6.96-6.95 (d, 1H), 4.13-4.06 (m, 4H), 1.83- 1.75 (m, 4H), 1.48-1.26 (m, 36H), 0.88-0.86 (t, 6H) ppm; **MS-FAB** (m/z): $[M+H]^+$ calculated for $C_{31}H_{54}O_3$ is 475.76; found 474.31.

2.6.12. Preparation of 2-{4-[2-(3,4-bis-dodecyloxy-phenyl)-vinyl]-phenyl}-5,5-dimethyl-[1,3]dioxane (9b)

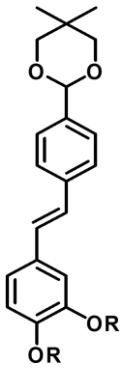

9b

Synthesis of **9b** was carried out by following the same procedure for the synthesis of compound **9a**. **Yield**: 85%; **m.p.** 82-84 °C; **^{1}H NMR** (300 MHz, $CDCl_3$, TMS) δ: 7.92-7.91 (m, 2H), 7.6-7.45 (m, 4H), 6.89-6.86 (m, 3H), 5.32 (s, 1H), 3.95-3.86 (m, 4H), 3.7-3.45 (m, 4H), 1.64-1.21 (m, 40H), 0.82-0.81 (t, 9H), 0.79 (s, 3H) ppm; **MS-FAB** (m/z): $[M+H]^+$ calculated for $C_{56}H_{94}O_5$ is 664.02; found 663.45.

2.6.13 .Preparation of 4-[2-(3,4-bis-dodecyloxy-phenyl)-vinyl]-benzaldehyde (10b)

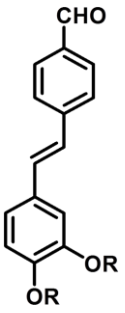

10b

Synthesis of **10b** was carried out by using the same procedure for the synthesis of compound **10a**. **Yield**: 90%; **^{1}H NMR** (300 MHz, $CDCl_3$, TMS) δ: 9.99 (s, 1H), 7.92-7.91 (m, 2H), 7.7- 7.54 (m, 4H), 6.89-6.86 (m, 3H), 4.05-3.96 (t, 4 H), 1.83-1.75 (m, 4H), 1.48-1.26 (m, 36H), 0.88-.86 (t 6H) ppm; **MS-FAB** (m/z): $[M+H]^+$ calculated for $C_{51}H_{84}O_4$ is 577.89; found 577.9.

2.6.14. Preparation of 1,2-Bis-dodecyloxy-4-(2-{4-[2-(4-nitro-phenyl)-vinyl]-phenyl}-vinyl)-benzene (11b)

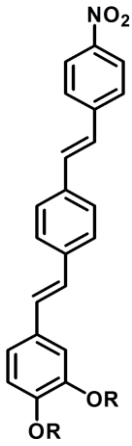

11b

Synthesis of **11b** was accomplished by the same procedure used for the synthesis of compound **11a**. **Yield**: 80%; **m.p.** 90-92 °C; **^{1}H NMR** (300 MHz, $CDCl_3$, TMS) δ: 8.28-8.21 (m, 2H), 7.71-7.63 (m, 2H), 7.53 (s, 4H), 7.18-7.1 (m, 2H), 7.04-6.95 (m, 2H), 6.95- 6.73 (m, 3H), 4.05-3.98 (t, 4H), 1.83-1.76 (t, 4H), 1.56-1.27 (m, 37H), 0.881-0.86 (t, 6H) ppm; **MS-FAB** (m/z): $[M+H]^+$ calculated for $C_{58}H_{89}NO_5$ is 697.01; found 698.1.

2.6.15. Preparation of 4-(2-{4-[2-(3,4-bis-dodecyloxy-phenyl)-vinyl]-phenyl}-vinyl)-phenylamineCompound (12b)

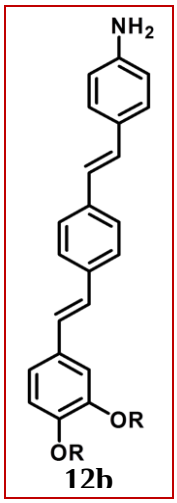

12b

Synthesis of **12b** was achieved by the same procedure used for the synthesis of compound **12a**. **Yield**: 85%; **m.p.** 78-82 °C; **^{1}H NMR** (300 MHz, $CDCl_3$, TMS) δ: 7.5-7.28 (m, 4H), 7.19-7.07 (m, 2H), 7.04-6.88 (m, 3H), 6.81-6.79 (m, 3H), 6.4-6.38 (d, 3H), 4.69 (s, 2H), 3.99-3.9 (t, 4H), 1.83-1.76 (t, 4H), 1.51-1.3 (m, 37H), 0.88-.87 (t, 6H) ppm; **MS-FAB** (m/z): $[M+H]^+$ calculated for $C_{58}H_{91}NO_3$ is 851.35; found 852.1.

2.6.16. Synthesis of *C*$_3$OPV2

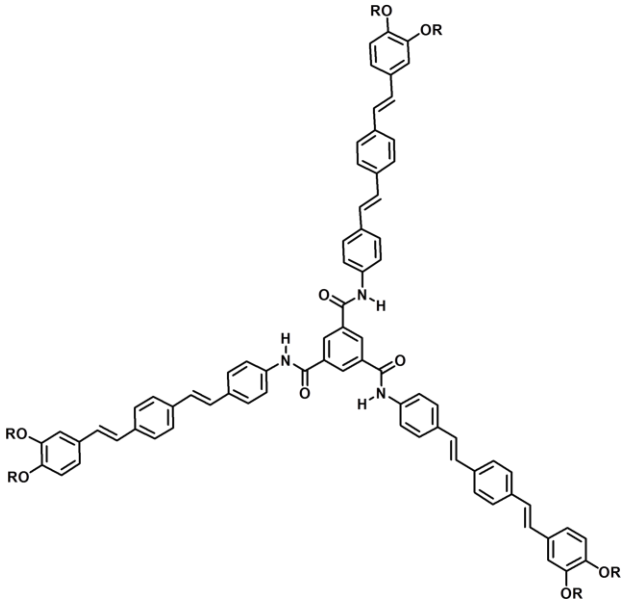

***C*$_3$OPV2**

Synthesis of ***C*$_3$OPV2** was carried out by following the same procedure for the synthesis of ***C*$_3$OPV1**.

Yield: 50%; **m.p.** > 260 °C; **^{1}H NMR** (300 MHz, THF-d_8) δ: 11.00 (s, 3H), 9.94 (s, 3H), 8.78 (s, 3H), 7.9-7.87 (d, 6H), 7.77-7.41 (m, 16H), 7.19-7.03 (m, 14H), 6.78 (s, 6H), 4.02-3.82 (m 12H), 1.77-1.31 (m, 180H) 0.89 (s, 18H) ppm; **^{13}C NMR** (125 MHz, $CDCl_3$) δ: 11.6, 20.7, 22.2, 29.6, 29.8, 31.8, 65.2, 73.8, 102.8, 118.3,

124.6, 124.8, 125.4, 134, 136.7, 138.1, 153.5, 165.2 ppm; **MALDI-TOF-MS**: m/z calculated for $C_{147}H_{201}N_3O_9$ [M^+] is 2155.20; found 2155.23.

Synthesis of *C*$_3$OPV3

***C*$_3$OPV3** was synthesized by using similar procedure as that of ***C*$_3$OPV1** and ***C*$_3$OPV2. Yield**: 42%; **^{1}H NMR** (300 MHz, THF-d_8) δ: 11.12 (s, 3H), 10.07 (s, 3H), 8.67 (s, 3H), 7.79-7.77 (d, 6H), 7.44-7.41 (m, 16H), 7.06-6.91 (m, 14H), 6.78 (s, 6H), 4.02-3.82 (m 12H), 1.77-1.31 (m, 180H) 0.89 (s, 18H) ppm; **^{13}C NMR** (125 MHz, $CDCl_3$)δ : 11.4, 21.3, 22.2, 29.7, 29.8, 31.2, 65.0, 72.6, 102.6, 116.1, 124.0, 124.6, 125.2, 134.2, 136.8, 138.7, 153.1, 165.2 ppm; **MALDI-TOF-MS:** m/z calculated for $C_{147}H_{201}N_3O_9$ [M^+] is 2155.20; found: 2155.74.

2.7. References

1. Tschierske, C. *J. Mater. Chem.* **2008**, *18*, 2869–2871.

2. O'Neil, M.; Kelly, S. M. *Adv. Mater*. **2003**, *15*, 1135–1146.

3. Ikeda, T.; Mamiya, J.-i.; Yu, Y. *Angew. Chem., Int. Ed.* **2007**, *46*, 506–528.

4. Hirst, A. R.; Escuder, B.; Miravet, J. F.; Smith, D. K. *Angew. Chem., Int. Ed.* **2008**, *47*, 8002–8018.

5. Babu, S. S.; Praveen, V. K.; Ajayaghosh, A. *Chem. Rev.* **2014**, *114*, 1973–2129.

6. Babu, S. S.; Prasanthkumar, S.; Ajayaghosh, A. *Angew. Chem., Int. Ed*. **2012**, *51*, 1766–1776.

7. Banerjee, S.; Das, R. K.; Maitra, U. *J. Mater. Chem.* **2009**, *19*, 6649–6687.

8. Sangeetha, N. M.; Maitra, U. *Chem. Soc. Rev*. **2005**, *34*, 821–836.

9. Li, J.-L.; Liu, X.-Y. *Adv. Funct. Mater.* **2010**, *20*, 3196–3216.

10. Demus, D.; Goodby, J.; Gray, G. W.; Spiess, H. W.; Vill, V. *Handbook of Liquid Crystals*, Wiley-VCH, Weinheim **1998**.

11. Chandrasekhar, S. *Liquid Crystals*, 2nd ed., Cambridge University Press, Cambridge **1992**.

12. Fouquey, C.; Lehn, J.-M.; Levelut, A.-M. *Adv. Mater.* **1990**, *2*, 254–257.

13. Lehn, J.-M. *Makromol. Chem., Macromol. Symp.* **1993**, *69*, 1–17.

14. Gulik-Krzywicki, T.; Fouquey, C.; Lehn, J.-M. *Proc. Natl. Acad. Sci. U.S.A.* **1993**, *90*, 163–167.

15. Kotera, M.; Lehn, J.-M.; Vigneron, J.-P. *J. Chem. Soc., Chem. Commun.* **1994**, 197–199.

16. Marchi-Artzner, V.; Jullien, L.; Gulik-Krzywicki, T.; Lehn, J.-M. *Chem. Commun.* **1997**, 117–118.

17. Matsunaga, Y.; Terada, M. *Mol. Cryst. Liq. Cryst.* **1986**, *141*, 321–326.

18. Praefcke, K.; Levelut, A.-M.; Kohne, B.; Eckert, A. *Liq. Cryst.* **1989**, *6*, 263–270.

19. Ebert, M.; Kleppinger, R.; Soliman, M.; Wolf, M.; Wendorf, J. H.; Latterman, G.; Staufer, G. *Liq. Cryst.* **1990**, *7*, 553–570.

20. Festag, R.; Kleppinger, R.; Soliman, M.; Wendorff, J. H.; Latterman, G.; Staufer, G. *Liq. Cryst.* **1992**, *11*, 699–710.

21. Malthête, J.; Levelut, A.-M.; Liebert, L. *Adv. Mater.* **1992**, *4*, 37–41.

22. Kato, T.; Kihara, H.; Kumar, U.; Uryu, T.; Fréchet, J. M. *Angew. Chem., Int. Ed. Engl.* **1994**, *33*, 1644–1645.

23. Kleppinger, R.; Lillya, C. P.; Yang, C. *Angew. Chem., Int. Ed. Engl.* **1995**, *34*, 1637–1638.

24. Albouy, P. A.; Guillon, D.; Heinrich, B.; Levelut, A.-M.; Malethête, J. *J. Phys. II Fr.* **1995**, *5*, 1617–1634.

25. Koh, K. N.; Araki, K.; Komori, T.; Shinkai, S. *Tetrahedron Lett.* **1995**, *36*, 5191–5194.

26. Palmans, A. R. A.; Vekemans, J. A. J. M.; Fischer, H.; Hikmet, R. A.; Meijer, E. W. *Chem.–Eur. J.* **1997**, *3*, 300–307.

27. Kleppinger, R.; Lillya, C. P.; Yang, C. *J. Am. Chem. Soc*. **1997**, *119*, 4097–4102.

28. Kato, T.; Kubota, Y.; Uryu, T.; Ujiie, S. *Angew. Chem., Int. Ed*. *Engl.* **1997**, *36*, 1617–1618.

29. Suarez, M.; Lehn, J.-M.; Zimmerman, S. C.; Skoulios, A.; Heinrich, H. *J. Am. Chem. Soc*. **1998**, *120*, 9526–9532.

30. Terech, P.; Weiss, R. G. *Chem. Rev.* **1997**, *97*, 3133–3160.

31. van Esch, J. H.; Feringa, B. L. *Angew. Chem., Int. Ed*. **2000**, *39*, 2263–2266.

32. Abdallah, D. J.; Weiss, R. G. *J. Braz. Chem. Soc.* **2000**, *11*, 209–218.

33. *Molecular Gels, Materials with Self-Assembled Fibrillar Networks*; Terech, P., Weiss, R., Eds.; Kluwer Academic Publishers: Dordrecht, The Netherlands, **2005**.

34. Babu, S. S.; Kartha, K. K.; Ajayaghosh, A. *J. Phys. Chem. Lett*. **2010**, *1*, 3413–3424.

35. Piepenbrock, M.-O. M.; Lloyd, G. O.; Clarke, N.; Steed, J. W. *Chem. Rev*. **2010**, *110*, 1960–2004.

36. Ghosh, S.; Li, X-Q.; Stepanenko, V.; Würthner, F. *Chem. –Eur. J.* **2008**, *14*, 11343 – 11357

37. Ono, Y.; Nakashima, K.; Sano, M.; Kanekiyo, Y.; Inoue, K.; Hojo, J.; Shinkai, S. *Chem. Commun*. **1998**, 1477–1478.

38. Jung, J. H.; Ono, Y.; Shinkai, S. *Angew. Chem., Int. Ed*. **2000**, *39*, 1862–1865.

39. Jung, J. H.; Ono, Y.; Sakurai, K.; Sano, M.; Shinkai, S. *J. Am. Chem. Soc*. **2000**, *122*, 8648–8653.

40. Swager, T. M.; Gil, C. J.; Wrighton, M. S. *J. Phys. Chem*. **1995**, *99*, 4886–4893.

41. Schoonbeek, F. S.; van Esch, J.; Wegewijs, B.; Rep, D. B. A.; de Haas, M. P.; Klapwijk, T. M.; Kellogg, R. M.; Feringa, B. L. *Angew. Chem., Int. Ed. Engl.* **1999**, *38*, 1393–1397.

42. Ajayaghosh, A.; Praveen, V. K. *Acc. Chem. Res*. **2007**, *40*, 644–656.

43. Burroughes, J. H.; Bradley, D. D. C.; Brown, A. R.; Marks, R. N.; MacKay, K.; Friend, R. H.; Burns, P. L.; Holmes, A. B. *Nature* **1990**, *347*, 539–541.

44. Kraft, A.; Grimsdale, A. C.; Holmes, A. B. *Angew. Chem., Int. Ed.* **1998**, *37*, 402–428.

45. Yu, G.; Gao, J.; Hummelen, J. C.; Wudl, F.; Heeger, A. J. *Science* **1995**, *270*, 1789–1791.

46. Halls, J. J. M.; Walsh, C. A.; Greenham, N. C.; Marseglia, E. A.; Friend, R. H.; Moratti, S. C.; Holmes, A. B. *Nature* **1995**, *376*, 498–500.

47. Brabec, C. J.; Sariciftci, N. S.; Hummelen, J. C. *Adv. Funct. Mater.* **2001**, *11*, 15–26.

48. El-ghayoury, A.; Schenning, A. P. H. J.; van Hal, P. A.; van Duren, J. K. J.; Janssen, R. A. J.; Meijer, E. W. *Angew. Chem., Int. Ed*. **2001**, *40*, 3660–3663.

49. Ramos, A. M.; Rispens, M. T.; van Duren, J. K. J.; Hummelen, J. C.; Janssen, R. A. J. *J. Am. Chem. Soc.* **2001**, *123*, 6714–6715.

50. Horowitz, G. *Adv. Mater.* **1998**, *10*, 365–377.

51. Sirringhaus, H.; Brown, P. J.; Friend, R. H.; Nielsen, M. M.; Bechgaard, K.; Langeveld-Voss, B. M. W.; Spiering, A. J. H.; Janssen, R. A. J.; Meijer, E. W.; Herwig, P.; de Leeuw, D. M. *Nature* **1999**, *401*, 685–688.

52. Cornil, J.; Beljonne, D.; Calbert, J.-P.; Bréads, J.-L. *Adv. Mater*. **2001**, *13*, 1053–1067.

53. Martin, R. E.; Diederich, F. *Angew. Chem., Int. Ed.* **1999**, *38*, 1350–1377.

54. Tour, J. M. *Chem. Rev.* **1996**, *96*, 537–554.

55. Müllen, K.; Wegner, G. *Electronic Materials*; *The Oligomer Approach*; VCH: Weinheim, Germany, **1998**.

56. (a) Ajayaghosh, A.; George, S. J. *J. Am. Chem. Soc.* **2001**, *123*, 5148–5149; (b) George, S. J. ; Ajayaghosh, A. *Chem.–Eur. J.* **2005**, *11*, 3217–3227.

57. Palmans, A. R. A.; Vekemans, J. A. J. M.; Fischer, H.; Hikmet, R. A.; Meijer, E. W. *Chem.–Eur. J.* **1997**, *3*, 300–307.

58. Timme, A.; Kress, R.; Albuquerque, R. Q.; Schmidt, H.-W. *Chem.–Eur. J.* **2012**, *18*, 8329–8339.

59. Kreger, K.; Wolfer, P.; Audorff, H.; Kador, L.; Stutzmann, N. S.; Smith, P.; Schmidt, H.-W. *J. Am. Chem. Soc*. **2010**, *132*, 509–516.

60. Ryu, S. Y.; Kim, S.; Seo, J.; Kim, Y.-W.; Kwon, O.-H.; Jang, D.-J.; Park, S. Y. *Chem. Commun.* **2004**, 70–71.

61. Kotova, O.; Daly, R.; dos Santos, C. M. G.; Boese, M.; Kruger, P. E.; Boland, J. J.; Gunnlaugsson, T. *Angew. Chem., Int. Ed*. **2012**, *51*, 7208 –7212.

62. Danila, I.; Riobé, F.; Puigmartí-Luis, J.; del Pino, Á. P.; Wallis, J. D.; Amabilino, D. B.; Avarvari, N. *J. Mater. Chem*. **2009**, *19*, 4495–4504.

63. Danila, I.; Pop, F.; Escudero, C.; Feldborg, L. N.; Puigmartí-Luis, J.; Riobé, F.; Avarvari, N.; Amabilino, D. B. *Chem. Commun*. **2012**, *48*, 4552–4554.

64. Fitié, C. F. C.; Tomatsu, I.; Byelov, D.; de Jeu, W. H.; Sijbesma, R. P. *Chem. Mater.* **2008**, *20*, 2394–2404.

65. Gelinsky, M.; Vogler, R.; Vahrenkamp, H. *Inorg. Chem*. **2002**, *41*, 2560–2564.

66. Broaders, K. E.; Pastine, S. J.; Grandhe, S.; Fréchet, J. M. J. *Chem. Commun*. **2011**, *47*, 665–667.

67. (a) Chandrasekhar, S.; Sadashiva, B. K.; Suresh, K. A. *Pramana* **1977**, *9*, 471–480. (b) Kumar, S. *Liquid Crystals* **2009**, *36*, 607–638.

68. (a) Bao, C.; Lu, R.; Jin, M.; Xue, P.; Tan, C.; Xu, T.; Liu, G.; Zhao, Y. *Chem. – Eur. J.* **2006**, *12*, 3287–3294; (b) Aparicio, F.; Garcia, F.; Fernández, G.; Matesanz, E.; Sánchez, L. *Chem. –Eur. J.* **2011**, *17*, 2769–2776.

69. (a) Varghese, S.; Kumar, N. S. S.; Krishna, A.; Rao, D. S. S.; Prasad, S. K.; Das, S. *Adv. Funct. Mater.* **2009**, *19*, 2064–2073. (b) Prabhu, D. D.; Kumar, N. S. S.; Sivadas, A. P.; Varghese, S.; Das, S. *J. Phys. Chem. B* **2012**, *116*, 13071–13080.

70. (a) Meier, H.; Holst, H. C.; Oehlhof, A. *Eur. J. Org. Chem.* **2003**, 4173–4180. (b) van Herrikhuyzen, J.; Jonkheijm, P.; Schenning, A. P. H. J.; Meijer, E. W. *Org. Biomol. Chem.* **2006**, *4*, 1539–1545.

71. Dierking, I. *Textures of Liquid Crystals*, Wiley-VCH, Weinheim, Germany), **2003**.

72. Kumar, S. *Chemistry of Discotic Liquid Crystals: From Monomers to Polymers*, CRC Press; Taylor & Francis Group, New York, **2010**.

73. Palmans, A. R. A.; Vekemans, J. A. J. M.; Fischer, H.; Hikmet, R. A.; Meijer, E. W. *Chem. –Eur. J.* **1997**, *3*, 300–309.

74. Chen, Z.; Lohr, A.; Saha-Möller, C. R.; Würthner, F. *Chem. Soc. Rev.* **2009**, *38*, 564–584.

75. van Gorp, J. J.; Vekemans, J. A. J. M.; Meijer, E. W. *J. Am. Chem. Soc*. **2002**, *124*, 14759-14769.

76. George, M.; Weiss, R. G. *J. Am. Chem. Soc.* **2001**, *123*, 10393–10394.

Chapter 3

(Part a)

Vapor Phase Detection of Nitroaromatic Explosives by C_3-Symmetrical Oligo(*p*-phenylenevinylene)s

3a.1. Abstract

*Trinitrotoluene (TNT) and Dinitrotoluene (DNT) are widely used as explosives in landmines and military operations that contaminate the environment. Sensing of this class of nitroaromatics in air is extremely important. Herein, a fluorescence approach is described for the sensing of nitroaromatics in the vapor phase. For this purpose, two C_3-symmetrical oligo(p-phenylenevinylenes), **C_3OPV1**, and **C_3OPV2**, have been utilized. **C_3OPV1** and **C_3OPV2** form spherical particles and interconnected fibrillar networks, respectively in both solution and surface by self-assembly. Both molecules were able to respond towards the vapors of nitroaromatic compounds by quenching the fluorophore emission. The percentage of emission quenching has been estimated using fluorescence studies. It was observed that the efficiency of fluorescence quenching is higher in the case of **C_3OPV_2** which self-assemble with a fiber morphology when compared to **C_3OPV_1**. Efficient quenching of fluorescence is observed in the case of fiber morphology than that of spherical particles even though the surface area is more for the later.*

3a.2. Introduction

The rapid detection of explosives is an important area of research because of its wide use in mine fields,[1] military applications, and homeland security applications.[2] Most of the explosives are composed of energetic chemicals and the basic principle of detection of explosives relies on the sensing of the constituent chemicals in solid or vapor states.[3,4] Even though a large number of reports are available, a simple approach for detecting explosives at extremely low concentrations still remains a challenge.[5,6] As an indirect method, metal detectors are used for sensing explosive devices that are made and packed only with metallic ingredients and thus limits their application. Another reliable approach to this purpose is the use of canines. However, high cost associated with the training and maintenance of these animals makes this technique labour intensive and expensive for the continuous monitoring of explosives.[7] Gas chromatography coupled with mass spectrometry,[8] nuclear quadrupole resonance,[9] electron capture detection,[10] surface enhanced Raman spectroscopy,[11] energy dispersive X-ray diffraction,[12] neutron activation analysis, and cyclic voltammetry,[13] are some of the other techniques used for the detection of explosives. However, because of the high cost of analysis and practical difficulties for onsite monitoring, these techniques are seldom used in real applications.

The key requirement for an efficient explosive sensor is a measurable signal in response to a trace amount of an analyte of interest.[14] Among diverse sensing methods, the most common signal transduction protocols utilize optical or electrical properties.[15] As a highly sensitive optical transduction method, fluorescence-based techniques are widely used for the detection of explosives, where analyte binding

produces a reduction (turn-off), enhancement (turn-on), or wavelength shift (ratiometric) in the emission. In the past few years, fluorescent conjugated polymers have been used extensively as sensing materials.[16,17] Recently, in addition to polymers, molecular assemblies of π-conjugated systems have been found efficient in the sensing of explosives.[18] Gels, and metal-organic frameworks (MOFs) have also been successfully used as chemosensors for the detection of explosives.[19-24]

Fluorescent π-conjugated polymers have been extensively used for the sensing of explosives. Swagar and co-workers significantly contributed in this area using a variety of poly(phenyleneethynylene) based polymers such as **1**-**3** (Chart 3a.1).[14,25] Presence of bulky groups such as pentiptycene on the polymer backbone prevents the aggregation induced fluorescence quenching and results in good fluorescent quantum yield in solid-state, which is an essential requirement for fluorescence based sensing.[14] π-Conjugated polymers show high sensitivity due to the delocalization of excitons and subsequent energy/electron transfer to the analytes.[25] Polysilols such as **4**-**7** (Chart 3a.1) were used by Troggler and co-workers for the detection of trace amount of explosives.[26-29]

The difficulties in synthesis, purification and processing of polymers hampered its progress in the area of sensing even though they had many advantages like high solid-state fluorescent quantum yield and better excited state energy delocalization.[20-24,30,31] To overcome these disadvantages of polymers, small molecules with a high solid-state quantum yield were developed as explosive sensors.[5,24] However, the sensitivity of small molecule based sensors are found to be extremely poor because of the absence of exciton migration. In this scenario, self-

assembled materials are found to be a good alternative for polymer-based explosive sensors. Compared to polymers, the synthesis, purification, and characterization of monodispersed self-assembled building blocks are much easier. Moreover, self-assembly allows the exciton migration assisted energy/electron transfer mechanism while sensing analytes and thereby enhances the sensitivity.

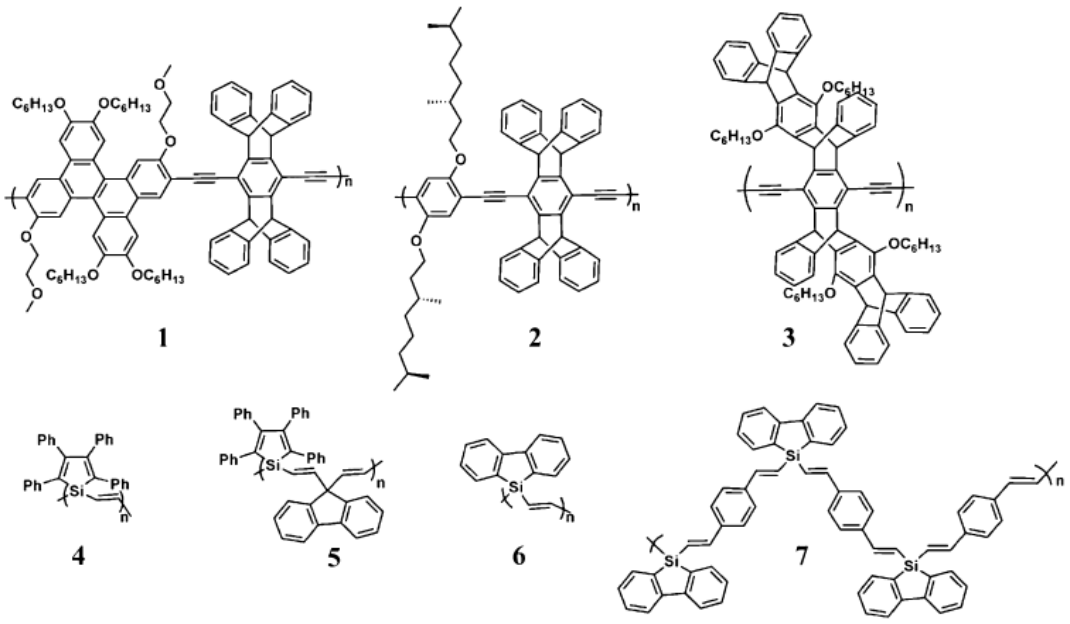

Chart 3a.1. Structures of some fluorescent polymers used for the detection of explosives.

The first report of self-assembled chemical sensor for the detection of explosives was based on oligo(tetraphenyl)silol nanoparticles.[32] The nanoparticle suspension prepared in THF/water has been used for the detection of 2,4,6-trinitrotoluene (TNT) in aqueous conditions. Moore and co-workers have prepared one-dimensional (1D) nanofibers from arylene-ethynylene-tetracycle with alkoxycarbonyl-substituted carbazoles at the corners (**8**) (Figure 3a.1a). This macrocycle showed amplified fluorescence quenching upon exposure to certain analytes such as TNT, adsorbed on the surface of the nanofiber (Figure 3a.1b).[33] The

amplified fluorescence quenching is obtained by efficient photoinduced electron transfer (PET), which is facilitated by the exciton migration along 1D structure. The long-range π–π overlap in the supramolecular assembly improves the exciton migration property. The porous nature of the film and the presence of carbazole groups that increase the overall electron donating ability of the molecule together help the efficient fluorescent quenching when exposing the film to electron deficient explosives. Micrometer long nanofibers prepared by the surface-casting techniques have been used for the sensing of explosives such as DNT and TNT.

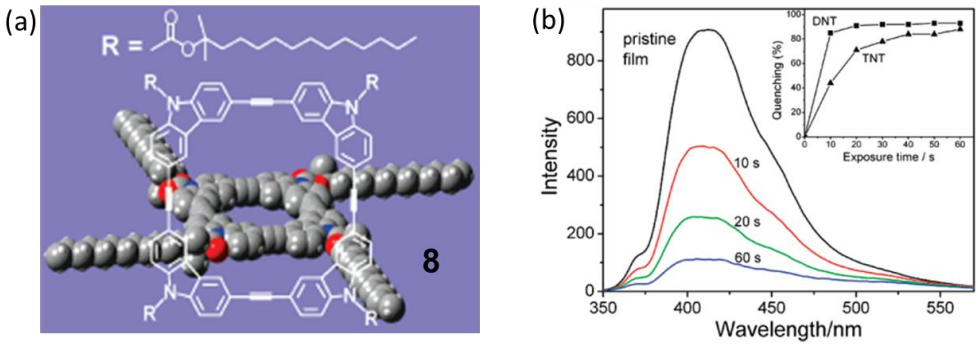

Figure 3a.1. (a) Chemical structure of **8**. (b) Fluorescence spectra of a 90 nm thick film of **8** upon exposure to saturated vapor of TNT (5 ppb) at different times. (Adapted with permission from ref. 33. Copyright 2007 American Chemical Society.)

The fluorescence of the film can be recovered either by exposure to air for a few days or by exposure to hydrazine vapor, which give fast recovery. The high efficiency of fluorescence quenching is ascribed to the presence of extended structure formed through intermolecular stacking, which in fact facilitates the efficient exciton migration. In addition the intrinsic nanoporous morphology formed within the film aids the adsorption and diffusion of gaseous analytes. The same molecule **8** is also used for the detection of 2,3-dimethyl-2,3-dinitrobutane

(DMNB).[34] Here also the fluorescence quenching is due to the exciton migration assisted electron transfer from the donor to the analyte, DMNB.

The nano morphology plays an important role in the efficiency of sensor.[35] To understand the importance of the nanostructures, three different nanostructures viz., microbelt and two flower-like nanostructures (flower A and B), were successfully fabricated using compound **9** and their sensing abilities were evaluated (Figure 3a.2). The detection speed of the DNT/TNT sensors was improved by more than 700-fold with the transformation of structure from 1D microbelts to the 3D flower-like super structures.

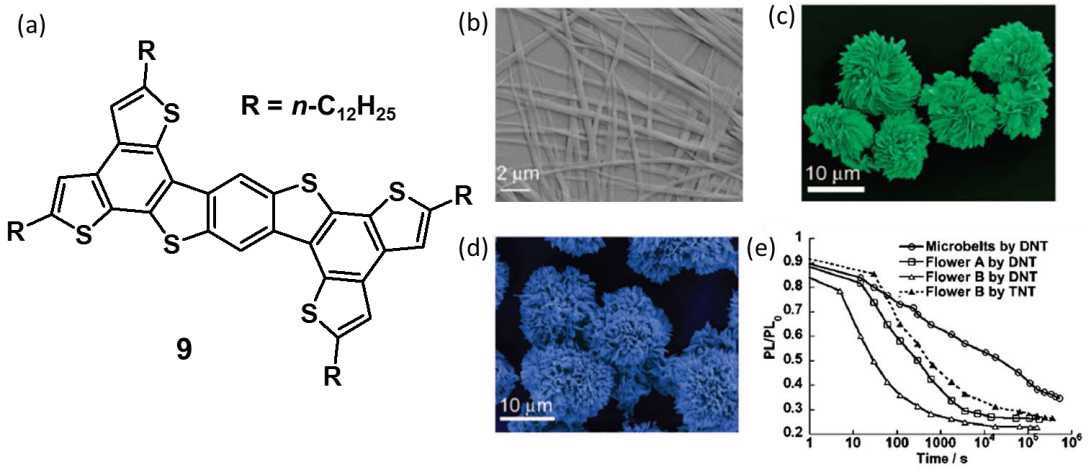

Figure 3a.2. (a) Chemical structure of **9**, (b), (c), (d) scanning electron microscopy (SEM) images of microbelt, flower A, flower B, respectively, self-assembled from 1,4-dioxane and (e) the plot of fluorescence quenching as a function of exposure time for all three nanostructures to DNT vapor and flower B's response to TNT vapor. (Adapted with permission from ref. 35. Copyright 2009 American Chemical Society.)

On exposure to DNT vapor, an abrupt decrease in the fluorescence intensity occurred within 10 seconds for flower B (Figure 3a.2e). For flower A such sharp quenching occurred in 15 seconds. On the contrary, the sensing speed of microbelts

are much slower. The high porosity and large surface area in the case of flower A and B allows faster diffusion of the analyte molecules into the superstructures, thereby increasing the detection speed.

The most widely used organic materials for the sensing applications are either zero-dimensional (spherical particles)[32,36] or the 1D nanostructures (fibers, rods, etc.).[37-39] Among these, 1D nanostructures have advantages over spherical particles, especially when the quenching mechanism is photoinduced electron transfer. In the case of 1D materials the exciton migration along the long axis, *i.e.* the π-π stacking direction enables amplified fluorescence quenching. The importance of 1D morphology is demonstrated by sensing TNT using a carbazole–fluorene molecular hybrid, **10** as the sensor (Figure 3a.3a).[40] This molecule showed different types of morphology in different solvents (Figure 3a.3b). In water, it formed nanoparticles with an average particle size of 100 nm. In methyl cyclohexane (MCH), weak gelation was observed and formed supramolecular rods of width 0.2-2 μm and length of several micrometers at a concentration range of 0.1-1 mM. Ill-defined molecular aggregates were formed in THF. Both nanoparticles and supramolecular rods showed blue fluorescence on excitation with UV light. The nanoparticles and rods showed selective vapor phase sensing of nitroaromatics. Exposure for TNT vapor over a 10 minutes time period showed a significant quenching of fluorescence by rods and only negligible changes were observed for ill-defined aggregates. In the film state, when exposed to TNT vapor for 30 seconds, 24% fluorescence quenching was observed for rods and only 15% for nanoparticles (Figure 3a.3d and 3e). However, after 5 minutes of exposure, the nanoparticles overtook the fluorescence

quenching of the rods. The ill-defined aggregates displayed no quenching in the initial 30 seconds. The better initial fluorescence quenching by the rods is due to the efficient energy migration along the 1D nanostructure, which amplifies the sensing efficiency. Figure 3a.3d shows the weight of TNT vapors adsorbed (upward) and the corresponding frequency shift (downward) of a quartz crystal microbalance (QCM) crystal coated with different nano morphologies.

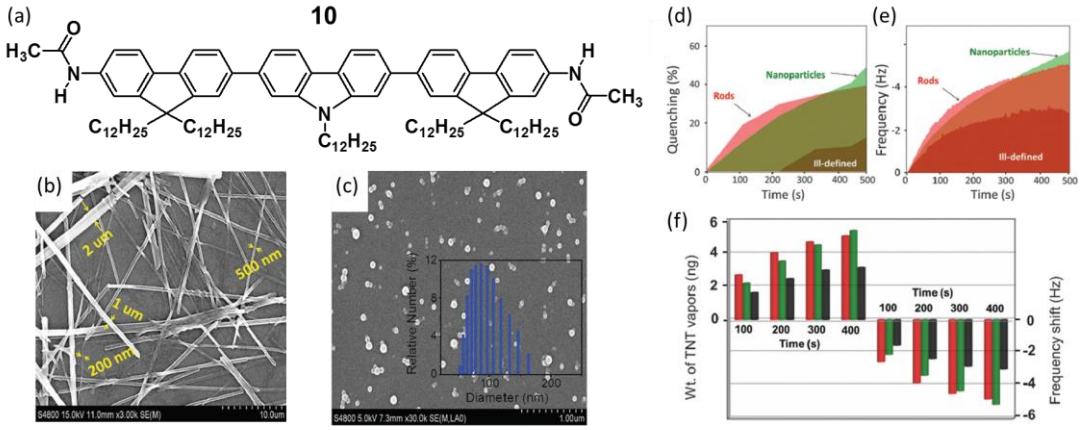

Figure 3a.3. (a) Structure of carbazole-fluorene hybrid molecule, **10**. Field emission-SEM images of (b) rods obtained from MCH solution (5 x 10^{-5} M) and (c) nanoparticle suspension in water drop cast on silicon wafer substrate (1 x 10^{-5} M). (d) A plot of fluorescence quenching percentage vs. time, (e) frequency shift of the quartz crystal vs. time and (f) weight of TNT vapors adsorbed (upward) and the corresponding frequency shift (downward) of a QCM crystal coated with rods (—), nanoparticles (—) and ill-defined molecular aggregates (—) upon exposure to TNT vapor. (Adapted with permission from ref. 40. Copyright 2014 The Royal Society of Chemistry.)

We have recently shown that an oligo(*p*-phenylenevinylene) based gelator can be used for the detection of attogram level of TNT (Figure 3a.4).[39] The molecule showed high solid-state fluorescence quantum yield due to the peculiar arene-perfluoroarene interaction. In solution state, the perfluoroarene based gelator **11** was found inefficient in sensing of TNT. However, the xerogel film prepared from

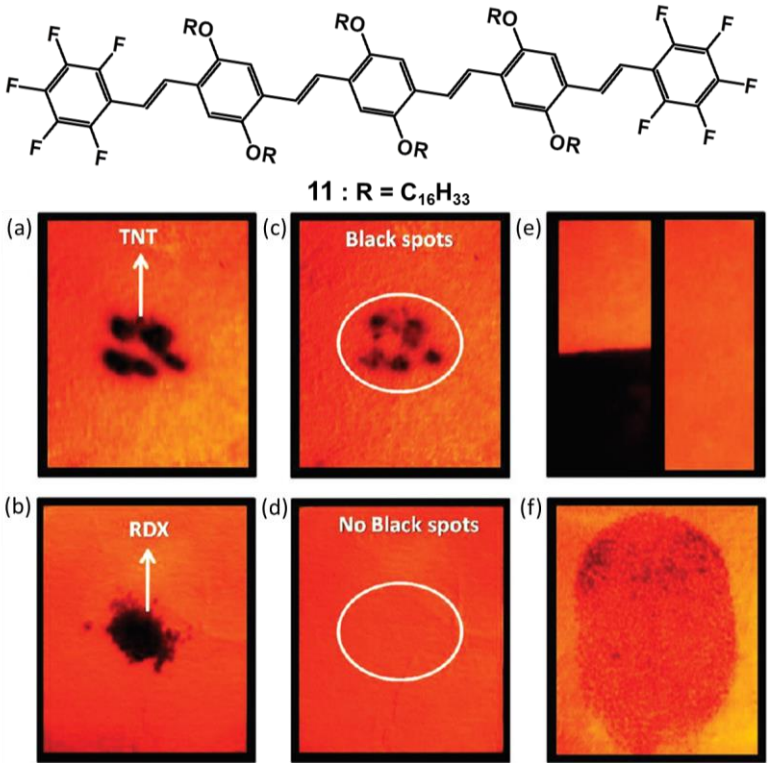

Figure 3a.4. Photographs of **11**-coated test strips under different experimental conditions. (a) TNT and (b) RDX crystals on top. (c, d) Corresponding photographs upon removal of the crystals after 5 sec. (e) After dipping into solutions of TNT (left) and RDX (right) in acetonitrile (1×10^{-3} M). (f) Thumb impression after rubbing with TNT crystals. All photographs were taken under 365 nm UV illumination. (Adapted with permission from ref. 39. Copyright 2012 American Chemical Society.)

n-decane gel of **11** showed significant quenching of fluorescence in the presence of different nitroaromatic compounds in the vapor state. The contact-mode response to TNT by the xerogel coated filter paper strips was also tested by placing TNT crystals over a test strip for 5 seconds, resulting in black spots upon illumination with a UV lamp (365 nm) (Figure 3a.4). The plausible mechanism of the fluorescence quenching with TNT in the xerogel state is depicted in Figure 3a.5. The gel fiber bundles of **11** are comprised of nanosized fibrils, which in turn are formed by self-assembled aggregates having different energy levels. Each aggregate is

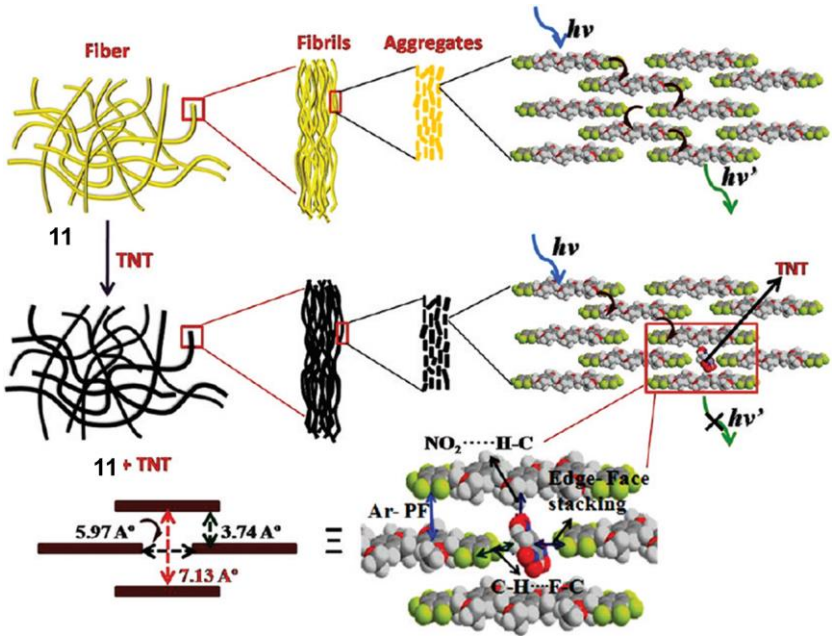

Figure 3a.5. Schematic illustration of the fluorescence quenching mechanism of the xerogel fibers of **11** in the presence of attogram levels of TNT. The bottom right picture shows various noncovalent interactions, and the bottom left picture shows the approximate distance between the gelator **11** in a brickwall-type arrangement. (Adapted with permission from ref. 39. Copyright 2012 American Chemical Society.)

formed by the brickwall-type arrangement of **11**. Since the molecular length of TNT (between the methyl group and the oppositely placed nitro group) is ~6.86 Å (Figure 3a.5), it can fit vertically into the free space through electrostatic interaction with **11** (Figure 3a.5). The fast excitation energy diffusion within the fibrils and between the fibrils facilitates efficient fluorescence quenching by possible energy and electron-transfer mechanisms, even with extremely low quantities of the quencher, resulting in attogram level detection.

Keeping in mind that OPV based molecules can be used for the detection of nitroaromatic analytes, we decide to utilize the OPV based C_3-symmetrical molecule, ***C*$_3$OPV2** (Figure 3a.6) that forms organogel in nonpolar solvents for the

detection of various nitroaromatic analytes in the xerogel state. In addition to this, we have utilized another OPV based C_3-symmetrical molecule ***C*$_3$OPV1** (Figure 3a.6) that forms nanoparticle in nonpolar solvents for the detection of nitroaromatics and compared its efficiency of sensing with respect to the nano morphology formed by the two C_3-symmetrical OPV molecules.

3a.3. Results and Discussions

3a.3.1. Synthesis

The detailed synthesis of ***C*$_3$OPV1** and ***C*$_3$OPV2** were already discussed in Chapter 2.

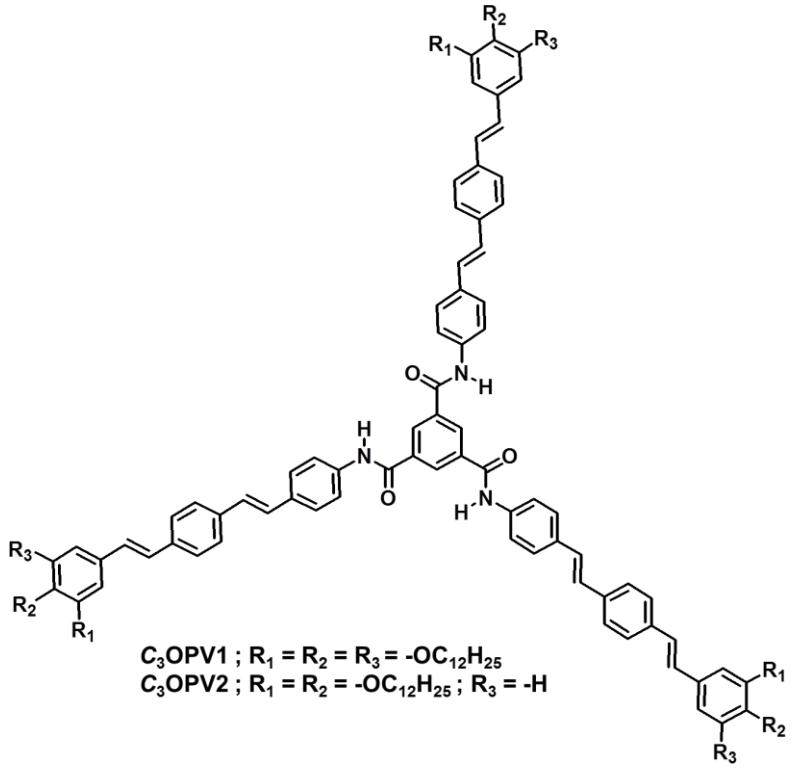

Figure 3a.6. Structure of the molecules ***C*$_3$OPV1** and ***C*$_3$OPV2**.

3a.3.2. Self-assembly of C_3OPV2

In order to understand the self-assembling properties of ***C*$_3$OPV2** in solution state, we have carried out detailed UV-Vis absorption studies in various solvents. The absorption profiles obtained in polar solvents such as tetrahydrofuran (THF) and chloroform indicate that ***C*$_3$OPV2** exists as monomer in these solvents with the absorption maximum at 380 nm (Figure 3a.7a). On the other hand, in solvents like *n*-decane, cyclohexane, toluene, etc., the absorption spectra showed a blue-shift of ~ 10 nm with the concomitant formation of an aggregation band at 425 nm (Figure 3a.7a). The blue-shift of the absorption spectrum with broadening and the presence of the aggregate band indicate the formation of supramolecular polymers in these solvents. This is further confirmed by the temperature dependent absorption studies. Upon increasing the temperature from 20 to 90 °C, the band observed at higher wavelengths completely disappeared with a concomitant red-shift of the absorption maximum (Figure 3a.7b). In order to understand the mechanism of self-assembly the absorption shoulder band at 425 nm was monitored as a function of temperature with a cooling rate of 1 K min^{-1}. No hysteresis was observed when the solution was heated again to the monomeric state, indicating that the thermodynamic self-assembly process is reversible. It is clear from the plot of the fraction of aggregates (α_{agg}) versus temperature that the molecule forms assembly through an isodesmic pathway (equal-K model) as indicated by the broad melting curve, which could be fitted with the standard isodesmic model (Figure 3a.7c). Generally, simple benzene trisamide based molecules self-assemble via cooperative mechanism. Based on our observation, we assume that the self-assembly of ***C*$_3$OPV2** is governed by π-π

stacking of OPV moieties and the contribution from intermolecular H-bonding may be weak due to the presence of sterically demanding aromatic core and the six alkyl chains at the periphery. The thermodynamic parameters are calculated by applying the isodesmic model and are summarized in Table 3a.1. The melting transition temperature (T_m, temperature at which α_{agg} = 0.50) of the assembly is found as 321.5 K (Figure 3a.7c) with an enthalpy value of -85.1 kJmol^{-1} and a binding constant of 4.7×10^4 M^{-1}.

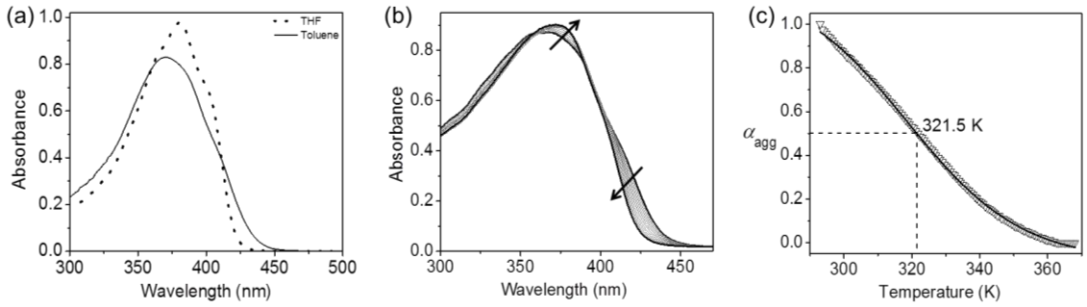

Figure 3a.7. (a) UV/Vis absorption spectra of ***C*$_3$OPV2** in THF and toluene (1×10^{-4} M), (b) temperature dependent absorption spectra of ***C*$_3$OPV2** in toluene (1×10^{-4} M) and (c) is the plot of fraction of aggregates (α_{agg}) against temperature for ***C*$_3$OPV2.** Absorbance is monitored at 425 nm and the heating rate is 1 K min^{-1}

Table 3a.1. Thermodynamic parameters calculated for the self-assembly of ***C*$_3$OPV2** using isodesmic model. Concentration is kept at 0.1 mM.

Molecule	ΔH (KJ mol^{-1})	ΔS (J mol^{-1} K^{-1})	ΔG (KJ mol^{-1})	T_m (K)	K_e (10^4 M^{-1})	DP_N
***C*$_3$OPV2**	-85.1	-194.5	-26.75	321.5	4.7	2.7

ΔH the change in enthalpy, ΔS the change in entropy, ΔG the change in free energy T_m the melting transition temperature, K_e the association constant and DP_N the degree of polymerization.

The emission spectrum of ***C*$_3$OPV2** also showed similar trend in these solvents. In polar solvents such as chloroform and THF, ***C*$_3$OPV2** displayed monomer-like emission with emission maximum centered on 430 nm (Figure 3a.8a). Whereas, in nonpolar solvent such as toluene, the emission displayed a red-shift with broadening of the spectrum (Figure 3a.8a). The temperature dependent emission studies were carried out in toluene. At lower temperature the emission spectrum was broad and as the temperature increases the emission spectrum becomes narrow and undergoes a blue shift that corresponds to the monomer emission (Figure 3a.8b).

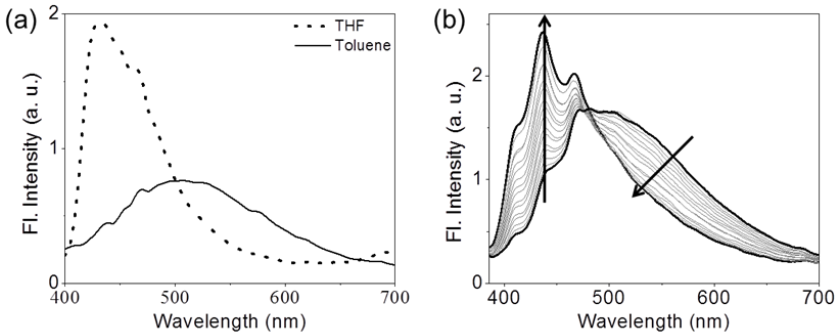

Figure 3a.8. (a) The emission spectrum of ***C*$_3$OPV2** in THF and toluene. (b) Temperature dependent (20 to 90 ˚C) emission spectra of ***C*$_3$OPV2** in toluene. In all the studies concentration of the solution is kept at 1×10^{-4} M, (λ_{ex} = 370 nm).

At higher concentrations, in less polar solvents such as *n*-decane, cyclohexane, toluene, etc. ***C*$_3$OPV2** was able to prevent the flow of solvents by forming a supramolecular network-like structure. However, usually benzene trisamide derivatives require high concentration for the formation of gel. For ***C*$_3$OPV2** to form gel in toluene, about 10 mg/mL of the molecule is required. The molecule could form a 3D assembly only at higher concentrations. At lower concentrations, the molecule stacks one over the other to form unidirectional supramolecular polymers.

As the concentration increases many such unidirectional polymers were formed, which then interact side wise via van der Waal interactions to form 3D packing. This requires higher concentration of the molecule.

Morphological features of ***C*$_3$OPV2** gels and assemblies were studied using atomic force microscopy (AFM), transmission electron microscopy (TEM) and scanning electron microscopy (SEM). To understand the morphology of the assemblies formed in the solution, a 10^{-4} M toluene solution was drop cast on mica substrate and imaged. The AFM analysis of the sample prepared on freshly cleaved mica surface revealed the formation of micrometer long fibers with width varying from 100-200 nm and height in the range of 10-20 nm (Figure 3a.9a and b). Similar kind of fiber morphology was also observed by other electron microscopic techniques such as TEM and SEM when samples were prepared on a carbon coated copper grid and mica respectively (Figure 3a.9c and d).

3a.3.3. Sensing of Explosives using *C*$_3$OPV2

Gels based on fluorescent molecules are suitable candidates for the sensing of various analytes. For example, fluorescent nanofibers obtained by molecular self-assembly are reported to be useful for the sensing of nitroaromatics. We have already reported that an OPV based molecule can sense TNT in attogram scale.[39] Therefore, we decided to check the suitability of ***C*$_3$OPV2** molecule for the sensing of nitroaromatics. Initially, response of ***C*$_3$OPV2** molecule in presence of nitroaromatics was tested in the solution state. The sensing of nitroaromatics using ***C*$_3$OPV2** solution in chloroform (1×10^{-4} M) was not successful. In the solution state, a very week fluorescence quenching was observed in the presence of TNT

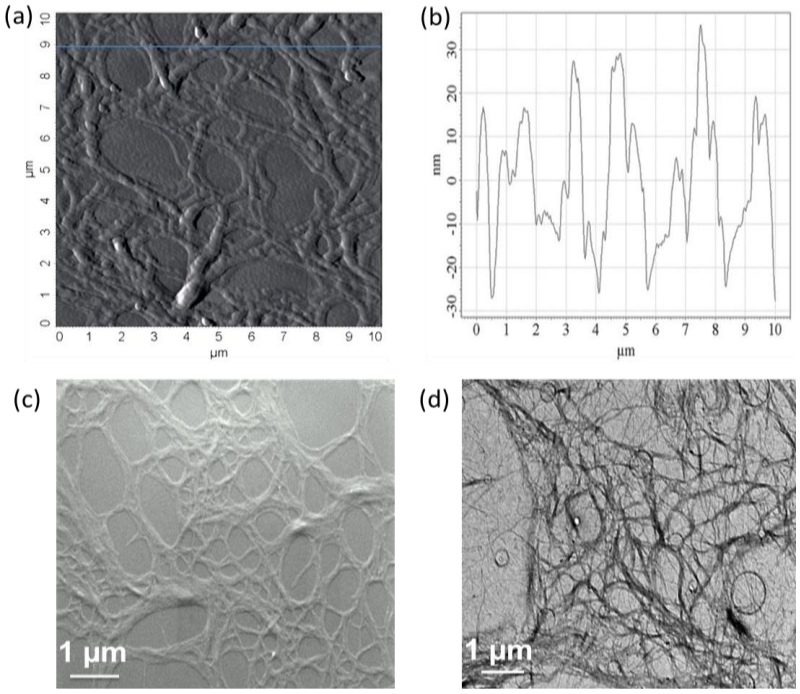

Figure 3a.9. (a) AFM, (b) AFM height profile (c)SEM, and (d) TEM images of ***C*$_3$OPV2** assemblies from toluene (4 x 10^{-4} M).

(Figure 3a.10). This observation implies that TNT is not an efficient quencher for ***C*$_3$OPV2** in the isotropic solution and hence is not suitable for the detection of TNT.

We then carried out the quenching studies in the film state. For this purpose, films were prepared on a glass slide by drop casting 20 µL of 1 x 10^{-4} M toluene solution. The film was then dried under vacuum and used for further studies. The molecule coated glass slide was then placed in a vial containing different nitroaromatics at room temperature. The emission spectra were then measured after exposing the film to the analytes for specific time intervals. Surprisingly, significant quenching of the fluorescence was observed upon exposure of the film to DNT vapors (Figure 3a.11a). The film when viewed under fluorescence microscope, we found that the green emissive fibers of the ***C*$_3$OPV2** assembly (Figure 3a.11b)

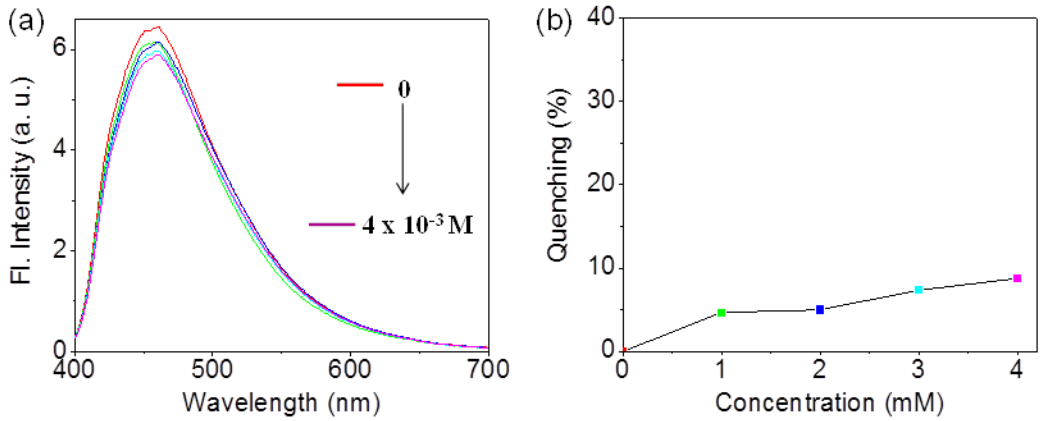

Figure 3a.10. (a) Emission spectra of ***C*$_3$OPV2** in chloroform (1 × 10^{-4} M) in the presence of different amounts of TNT. (b) Plot of quenching (%) at 456 nm vs concentration of TNT (λ_{ex} = 370 nm).

completely lost their emission within 1 minute exposure of DNT vapors (Figure 3.11c). A photograph of the film before and after the exposure of the saturated vapors of DNT is shown in Figure 3a.11e. The quenched emission of ***C*$_3$OPV2** film can be revived considerably by exposing the same film to vapors of ethanol (Figure 3a.11d).

In order to understand the excited-state behavior of the ***C*$_3$OPV2** assembly, the fluorescence lifetime decay profiles before and after exposure to DNT were recorded. The ***C*$_3$OPV2** aggregates (λ_{ex} = 375 nm) exhibited triexponential decay with lifetime values of 1.39 (51.1%), 0.405 (29.32%) and 4.84 ns (19.58%) when the emission was monitored at 530 nm (Figure 3a.12). Upon exposure to DNT vapor for 60 sec, fast triexponential decay with time constants of 0.044 (54%), 0.283 (39%) and 1.26 ns (6.24%) was observed (Figure 3a.12). The decrease in the lifetime values clearly indicates the interaction of DNT with the excited state of the of ***C*$_3$OPV2** aggregates.

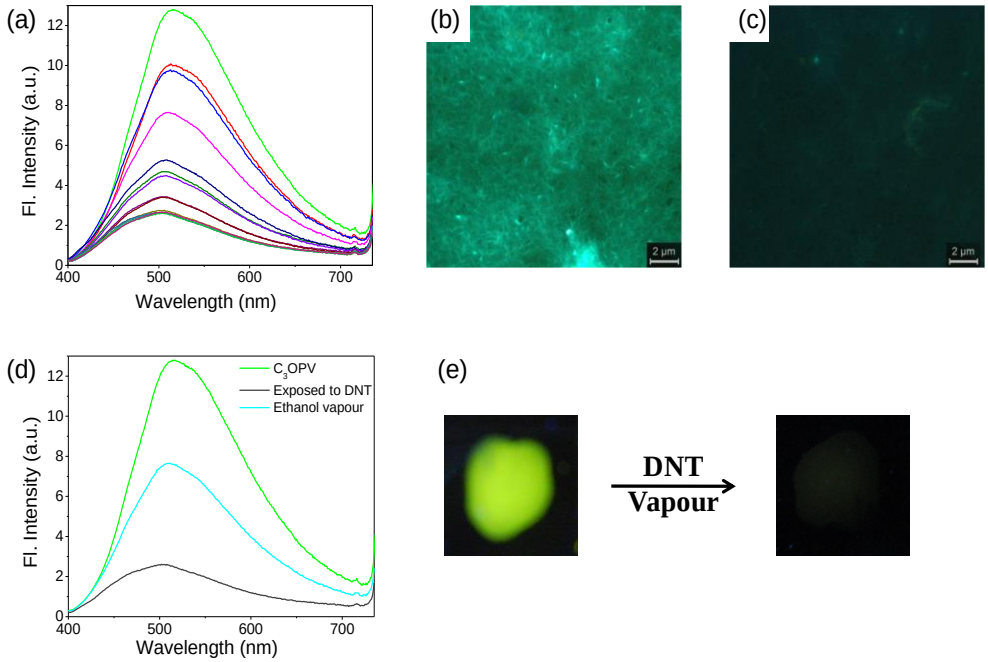

Figure 3a.11. (a) Time dependent fluorescence quenching of ***C*$_3$OPV2** assembly upon DNT vapor exposure. The fluorescence microscopy images of ***C*$_3$OPV2** film before (b) and after (c) exposing to saturated vapors of DNT for 1 minute. Spectrum (d) shows the emission revival after the film was exposed to the ethanol vapor and (e) photographs of ***C*$_3$OPV2** film before and after exposing to the DNT vapor up on 365 nm UV illumination.

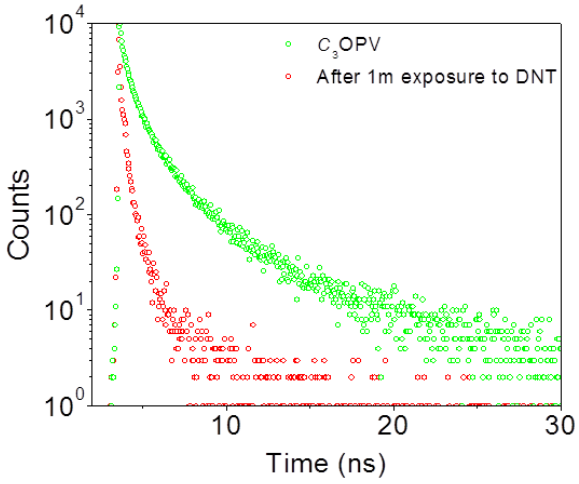

Figure 3a.12. Lifetime decay profiles (λ_{ex} = 375 nm, λ_{em} monitored at 530 nm) of ***C*$_3$OPV2** aggregates before (green circles) and after (red circles) exposure to DNT vapors for 1 minute

.

The response of ***C*$_3$OPV2** aggregates towards other nitroaromatic analytes such as nitrobenzene (NB), *o*-nitrotoluene (ONT), 2,4,6-trinitrotoluene (TNT), etc. were

carried out and the results are shown in Figure 3a.13. All these analytes respond to the ***C*$_3$OPV2** aggregates emission, but with different extent of fluorescence quenching. For the first 20 sec of exposure to different analytes, the data are shown in the form of a bar diagram in Figure 3a.13d.

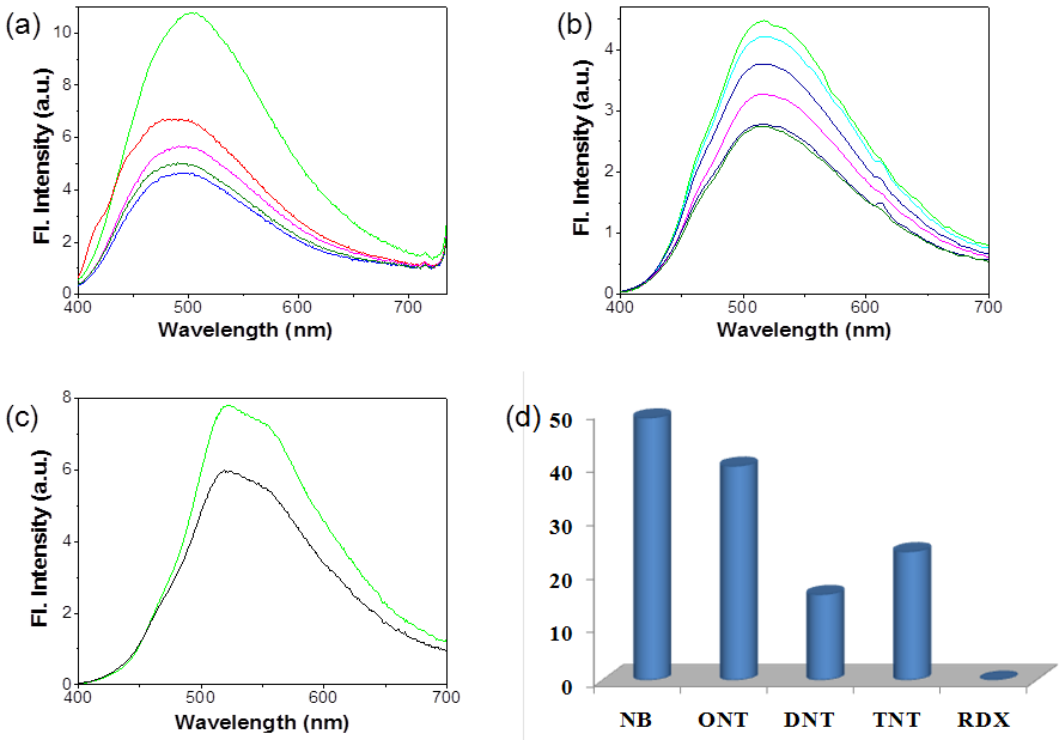

Figure 3a.13. (a) Time dependent fluorescence quenching of ***C*$_3$OPV2** assembly upon (a) nitrobenzene (NB), (b) *o*-nitrotoluene (ONT) and (c) TNT vapors exposure, (d) comparison of the fluorescence quenching efficiency of ***C*$_3$OPV2** aggregates upon exposure to saturated vapors of different analytes for 60 sec in a closed chamber (λ_{ex} = 375 nm).

Among the nitroaromatics tested, nitrobenzene showed fastest fluorescence quenching in which about 49% quenching was observed in first 20 seconds. *o*-Nitrotoluene showed almost 40% fluorescence quenching. Trinitrotoluene (TNT) showed faster response with 24% fluorescence quenching in 20 seconds than dinitrotoluene (DNT) that showed only 16 % quenching. In order to test the

specificity of the gelator for the detection of nitroaromatics, we have studied the effect of RDX, which is a non-aromatic explosive. Interestingly, the ***C*$_3$OPV2** aggregates did not show any fluorescence response when exposed to RDX vapors.

In order to understand the kinetics of fluorescence emission quenching, an experiment was carried out by continuous monitoring of the emission intensity at 525 nm as a function of time. For this purpose, 1 x 10^{-4} M solution of ***C*$_3$OPV2** was drop cast on a glass plate and was then immersed in a cuvette saturated with the analyte vapor. Immediately after dipping the glass plate, the emission intensity was monitored with time and the results obtained are shown in Figure 3a.14.

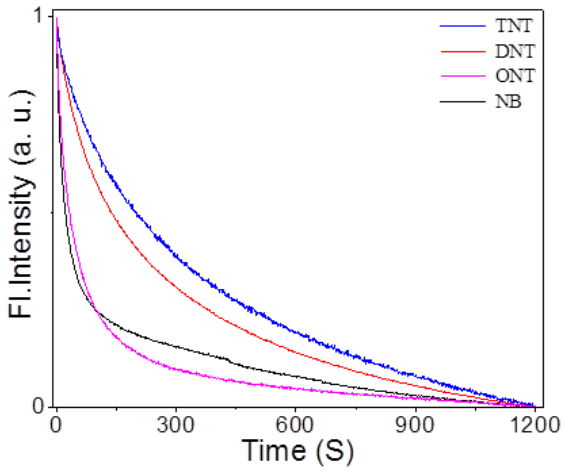

Figure 3a.14. Time dependent changes in the emission intensity at 530 nm for ***C*$_3$OPV2** aggregates on exposure to TNT (blue line), DNT (red line), ONT (magenta) and NB (black line), (λ_{ex} = 375 nm).

From this figure, it is clear that, immediately after exposure to the analyte, the fluorescence intensity decreases drastically and after a few minutes the decrease in intensity becomes almost saturated. This immediate decrease in fluorescence

intensity is due to the fast adsorption of the analyte vapor on the nanostructures and the photoinduced electron transfer from ***C*$_3$OPV2** to the adsorbed analytes.

In order to compare the quenching efficiency of ***C*$_3$OPV2** fibers to other morphologies, we have chosen another molecule ***C*$_3$OPV1** that forms nanoparticles upon self-assembly. ***C*$_3$OPV1** have almost similar structure to that of ***C*$_3$OPV2**, however, instead of two dodecyloxy chains on benzene ring of ***C*$_3$OPV2**, ***C*$_3$OPV1** has three dodecyloxy chains. When a 10^{-4} M solution of ***C*$_3$OPV1** was drop cast over a glass surface, it self-assembled to form spherical particles of size around 100 nm (Details are provided in Chapter 2). The time dependent quenching studies were carried out with both the molecules using DNT as the analyte. From the comparison graph (Figure 3a.15), it is clear that in the case of ***C*$_3$OPV2** the emission quenching is fast, while for ***C*$_3$OPV1**, the quenching is a slow process. For the first 1 minute, ***C*$_3$OPV1** showed only 2% quenching, whereas ***C*$_3$OPV2** showed quenching of about 26%. After 5 minutes also only 10% fluorescence quenching was observed for ***C*$_3$OPV1** while ***C*$_3$OPV2** displayed substantial quenching of about 57%.

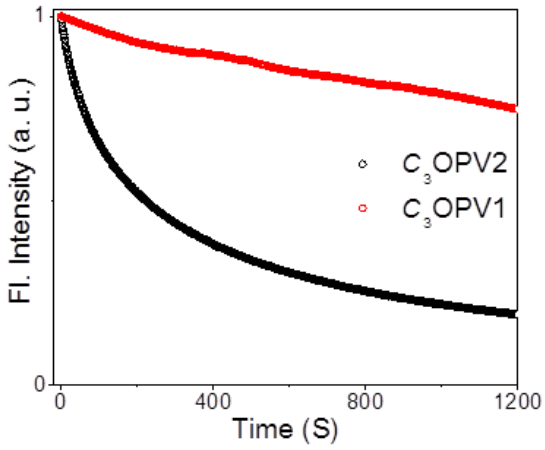

Figure 3a.15. Time dependent changes in the emission intensity at 530 nm for ***C*$_3$OPV1** and ***C*$_3$OPV2** aggregates on exposure to saturated DNT vapor, (λ_{ex} = 375 nm).

Based on the above observations, the mechanism of fluorescence quenching can be explained as follows. ***C*$_3$OPV2** molecules assemble together to form nanosized fibers. These small fibers interact to form thicker fiber bundles. The strong π-π interaction promotes the long-range molecular arrangement leading to the enhanced exciton migration via intermolecular π-electronic coupling. Once the ***C*$_3$OPV2** film is exposed to the analyte vapor such as DNT or TNT, there would be a donor-acceptor interaction. Subsequent irradiation leads to the excitation of the sensor molecule which then comes back to the ground state by transferring an electron to the nearest analyte molecule (nitroaromatics). Thus, the fluorescence of the donor molecule gets quenched. The efficiency of sensing depends upon the electron donating ability of fluorophore and the electron accepting ability of the acceptor, which in turn depends upon the HOMO-LUMO energy gap of both donor and acceptor. Since most of the nitroaromatics are strong electron accepters, the electron rich ***C*$_3$OPV2** facilitates electron transfer fluorescence quenching. The difference in quenching efficiency of the ***C*$_3$OPV2** towards the vapors of the various aromatic analytes depends on two factors: the electron accepting ability of the analyte and the vapor pressure of the analyte. The electron accepting ability of the aromatic analyte depends on the number of electron-withdrawing groups and electron-donating groups present in the molecule. Among the different nitroaromatics analyzed, nitrobenzene showed maximum fluorescence quenching with fastest response time. Even though nitrobenzene has only one nitro group, the vapor pressure is very high (0.15 mm Hg). The vapor pressure of *o*-nitrotoluene is about 0.285 mm Hg, but it shows less fluorescence quenching when compared to

nitrobenzene. The reason for this difference is due to the presence of methyl group in *o*-nitrotoluene. Methyl group ortho- to the nitro group reduces the electron accepting ability of the molecule. Both DNT and TNT have very low vapor pressure when compared to the other two analytes and are 6 x 10^{-5} and 12 x 10^{-5} mm Hg, respectively. Therefore, they show less fluorescence quenching when compared to nitrobenzene and nitrotoluene.

The morphology also plays an important role in determining the efficiency of fluorescence quenching. Due to large surface area, the amount of analytes adsorbed on the nanoparticles will be more than that adsorbed on the nanofibers, however, the nanofibers showed better fluorescence quenching than the nanoparticles. It is known that the excited state energy migration assisted electron transfer (amplified quenching[41]) in self-assembled materials enhances the sensing efficiency.[39,42] This kind of changes in the morphological features of the self-assembly processes can cause significant changes in the fluorescence properties. Better excited state energy migration is observed in the case of 1D nanofibres over spherical particles. Therefore, ***C*$_3$OPV2**, which forms fiber morphology, shows efficient fluorescence quenching when compared to ***C*$_3$OPV1**, which forms spherical particles.

3a.4. Conclusions

In summary, we have developed a C_3-symmetrical OPV derivative, ***C*$_3$OPV2**, which self- assembled to form organogel from toluene, *n*-decane, and can be utilized as a sensor for detecting nitroaromatic compounds. The molecule is emissive in both aggregated solution and film states. The fluorescence of the molecule in the film state was quenched upon exposure to the vapors of nitroaromatic compounds.

Photoinduced electron transfer (PET) from the donor fluorophore to the acceptor analyte molecule could be responsible for the fluorescence quenching. Detection of analytes in the film state is influenced by the vapor pressure of the analytes. Among different nitroaromatics analyzed, nitrobenzene showed maximum fluorescence quenching, because of its high vapor pressure and better electron accepting ability. Other electron deficient explosive such as RDX does not show any response towards fluorophore. When compared to the spherical particles formed by ***C*$_3$OPV1**, the 1D nanofiber formed by ***C*$_3$OPV2** showed faster and higher fluorescence quenching response towards nitroaromatics.

3a.5. Materials and Methods

3a.5.1. General

Synthesis and characterizations of ***C*$_3$OPV1** and ***C*$_3$OPV2** are described in the previous chapters.

TNT and RDX were obtained from High Energy Materials Research Laboratory, Pune, and recrystallized from ethanol.

3a.5.2. Instrumentation

UV/Vis absorption spectrophotometer, spectrofluorimeter, and AFM instruments are described in the experimental section (Section 2.5.2) of Chapter 2. Fluorescence lifetimes were measured using an IBH (FluoroCube) time-correlated picosecond single photon counting (TCSPC) system. Solutions were excited with a pulsed diode laser (<100 ps pulse duration) at a wavelength of 375 nm (NanoLED-11) with a repetition rate of 1 MHz. The detection system consists of a microchannel plate

photomultiplier (5000U-09B, Hamamatsu) with a 38.6 ps response time coupled to a monochromator (5000M) and TCSPC electronics (DataStation Hub including Hub-NL, NanoLED controller and preinstalled Fluorescence Measurement and Analysis Studio (FMAS) software). The fluorescence lifetime values were determined by deconvoluting the instrument response function with biexponential decay using DAS6 decay analysis software. The quality of the fit has been judged by the fitting parameters such as χ^2 (< 1.2) as well as the visual inspection of the residuals. All measurements were carried out using a front face sample holder (5000U-04). SEM images were taken on a JEOL 5600 LV scanning electron microscope with an accelerating voltage of 12−15 kV after sputtering with gold. TEM measurements were carried out in FEI-300kV HRTEM operated at 100 kV.

3a.6. References

1. Rouhi, A. M. *Chem. Eng. News* **1997**, *75*, 14–22.
2. Fainberg, A. *Science* **1992**, *255*, 1531–1537.
3. Yinon, J. *Forensic and Environmental Detection of Explosives*; John Wiley & Sons Ltd: Chichester, **1999**.
4. Steinfeld, J. I.; Wormhoudt, J. *Annu. Rev. Phys. Chem.* **1998**, *49*, 203–232.
5. Salinas, Y.; Martinez-Manez, R.; Marcos, M. D.; Sancenon, F.; Costero, A. M.; Parra, M.; Gil, S. *Chem. Soc. Rev.* **2012**, *41*, 1261–1296.
6. Germain, M. E.; Knapp, M. J. *Chem. Soc. Rev.* **2009**, *38*, 2543–2555.
7. Czarnik, A. W. *Nature* **1998**, *394*, 417–418.
8. Hakansson, K.; Coorey, R. V.; Zubarev, R. A.; Talrose, V. L.; Hakansson, P. *J. Mass Spectrom.* **2000**, *35*, 337–346.

9. Anferov, V. P.; Mozjoukhine, G. V.; Fisher, R. *Rev. Sci. Instrum.* **2000**, *71*, 1656–1659.

10. Rouhi, A. M. *Chem. Eng. News*, **1997**, *75*, 13.

11. Sylvia, J. M.; Janni, J. A.; Klein, J. D.; Spencer, K. M. *Anal. Chem.* **2000**, *72*, 5834–5840.

12. Luggar, R. D.; Farquharson, M. J.; Horrocks, J. A.; Lacey, R. J. *J. X-Ray Spectrom.* **1998**, *27*, 87–94.

13. Krausa, M.; Schorb, K. *J. Electroanal. Chem.* **1999**, *461*, 10–13.

14. Swager, T. M.; Wosnick, J. H. *MRS Bull.* **2002**, *27*, 446–450.

15. Salinas, Y.; Martinez-Manez, R.; Marcos, M. D.; Sancenon, F.; Costero, A. M.; Parra, M.; Gil, S. *Chem. Soc. Rev.* **2012**, *41*, 1261–1296.

16. Thomas, S. W.; Joly, G. D.; Swager, T. M. *Chem. Rev.* **2007**, *107*, 1339–1386.

17. McQuade, D. T.; Pullen, A. E.; Swager, T. M. *Chem. Rev.* **2000**, *100*, 2537–2574.

18. Palmer, L. C.; Stupp, S. I. *Acc. Chem. Res.* **2008**, *41*, 1674–1684.

19. Banerjee, D.; Hu, Z.; Li, J. *Dalton Trans.* **2014**, *43*, 10668–10685.

20. Zang, L.; Che, Y.; Moore, J. S. *Acc. Chem. Res.* **2008**, *41*, 1596–1608.

21. Gole, B.; Bar, A. K.; Mukherjee, P. S. *Chem. Commun.* **2011**, *47*, 12137–12139.

22. Nagarkar, S. S.; Joarder, B.; Chaudhari, A. K.; Mukherjee, S.; Ghosh, S. K. *Angew. Chem., Int. Ed.* **2013**, *52*, 2881–2885.

23. Gole, B.; Bar, A. K.; Mukherjee, P. S. *Chem. –Eur. J.* **2014**, *20*, 2276–2291.

24. Hu, Z.; Deibert, B. J.; Li, J. *Chem. Soc. Rev.* **2014**, *43*, 5815–5840.

25. Rose, A.; Zhu, Z. G.; Madigan, C. F.; Swager, T. M.; Bulovic, V. *Nature* **2005**, *434*, 876–879.

26. Sohn, H.; Calhoun, R. M.; Sailor, M. J.; Trogler, W. C. *Angew. Chem., Int. Ed.* **2001**, *40*, 2104–2105.

27. Toal, S. J.; Jones, K. A.; Magde, D.; Trogler, W. C. *J. Am. Chem. Soc.* **2005**, *127*, 11661–11665.

28. Content, S.; Trogler, W. C.; Sailor, M. J. *Chem. –Eur. J.* **2000**, *6*, 2205–2213.

29. Yang, J.; Aschemeyer, S.; Martinez, H. P.; Trogler, W. C. *Chem. Commun.* **2010**, *46*, 6804–6806.

30. Yang, J.-S.; Swager, T. M. *J. Am. Chem. Soc.* **1998**, *120*, 5321–5322.

31. Yang, J.-S.; Swager, T. M. *J. Am. Chem. Soc.* **1998**, *120*, 11864–11873.

32. Toal, S. J.; Magde, D.; Trogler, W. C. *Chem. Commun.* **2005**, 5465–5467.

33. Naddo, T.; Che, Y.; Zhang, W.; Balakrishnan, K.; Yang, X.; Yen, M.; Zhao, J.; Moore, J. S.; Zang, L. *J. Am. Chem. Soc.* **2007**, *129*, 6978–6979.

34. Naddo, T.; Yang, X.; Moore, J. S.; Zang, L. *Sens. Actuators B* **2008**, *134*, 287–291.

35. Wang, L.; Zhou, Y.; Yan, J.; Wang, J.; Pei, J.; Cao, Y. *Langmuir* **2009**, *25*, 1306–1310.

36. Toal, S. J.; Jones, K. A.; Magde, D.; Trogler, W. C. *J. Am. Chem. Soc.* **2005**, *127*, 11661–11665.

37. Naddo, T.; Che, Y. K.; Zhang, W.; Balakrishnan, K.; Yang, X. M.; Yen, M.; Zhao, J. C.; Moore, J. S.; Zang, L. *J. Am. Chem. Soc.* **2007**, *129*, 6978–6979.

38. Che, Y. K.; Yang, X. M.; Liu, G. L.; Yu, C.; Ji, H. W.; Zuo, J. M.; Zhao, J. C.; Zang, L. *J. Am. Chem. Soc.* **2010**, *132*, 5743–5750.

39. Kartha, K. K.; Babu, S. S.; Srinivasan, S.; Ajayaghosh, A. *J. Am. Chem. Soc.* **2012**, *134*, 4834–4841.

40. Kartha, K. K.; Sandeep, A.; Nair, V. C.; Takeuchi, M.; Ajayaghosh, A. *Phys. Chem. Chem. Phys.* **2014**, *16*, 18896–18901.

41. Thomas, S. W.; Joly, G. D.; Swager, T. M. *Chem. Rev.* **2007**, *107*, 1339–1386.

42. Zang, L.; Che, Y. K.; Moore, J. S. *Acc. Chem. Res.* **2008**, *41*, 1596–1608.

43. Che, Y. K.; Zang, L. *Chem. Commun.* **2009**, 5106–5108.

44. Che, Y. K.; Gross, D. E.; Huang, H. L.; Yang, D. J.; Yang, X. M.; Discekici, E.; Xue, Z.; Zhao, H. J.; Moore, J. S.; Zang, L. *J. Am. Chem. Soc.* **2012**, *134*, 4978–4982.

45. Huang, X.; Gu, X.; Zhang, G.; Zhang, D. *Chem. Commun.* **2012**, *48*, 12195–12197.

46. Bhalla, V.; Pramanik, S.; Kumar, M.; *Chem. Commun.* **2013**, *49*, 895–897.

47. Dey, N.; Samanta, S. K.; Bhattacharya, S. *ACS Appl. Mater. Interfaces* **2013**, *5*, 8394–8400.

Chapter 3

(Part b)

A Small Molecule Based Turn-Off Fluorescent Sensor for the Detection of Aromatic Amines

3b.1. Abstract

Development of sensors or probes that can be used to detect trace vapors of organic amines is one of the active research fields in chemistry and materials science. In this chapter, we demonstrate an organic amine sensing nanofiber material that has been fabricated from an electron deficient perylene bisimide molecule, ***C_3PBI****. The molecule was synthesized by a multistep synthetic strategy and its self-assembly properties have been studied. Drop casting of* ***C_3PBI*** *on mica surface produced entangled nanofibers with mesh like porous morphology which exhibited bright red fluorescence upon excitation at 490 nm. This porous material of* ***C_3PBI*** *assists the adsorption of amine vapors on its surface that resulted in the quenching of red emission by photoinduced electron transfer from the p-type organic amines to the n-type perylene bisimide molecule. It was also observed that the sensing response depends on the electron density and the vapor pressure of the amines.*

3b.2. Introduction

Most of the aromatics amines are toxic compounds which are extensively used as industrial chemicals.[1] Some of the amines, like hydrazine, have also been used in military operations, for example, as fuel additives in rocket and fighter jet propulsion systems.[2] As a result, these amines becomes widespread pollutants of the environment. Small scale detection of volatile organic substances such as amine, carboxylic acids or esters play an important role in diverse range of research fields from industrial and environmental monitoring[3-7] to food quality control[8-10] to medical diagnosis of certain diseases.[11-16] Fluorescent molecules that are reactive to these functional groups and exhibit switchable fluorescence response have attracted immense attention in this research area. Although, many successes have been achieved in solution state detection of amines, [17-19] the vapor phase detection still remains a challenge. Thus, developing suitable sensors for detecting amine vapors with higher sensitivity has become an intense area of research in the last few years. The key requirement for an efficient sensor is a measurable signal that could respond to trace amount of an analyte of interest. Among diverse sensing methods available, the most commonly used ones utilize optical or electrical property that changes in presence of an analyte and produce transduced signal. In this regard, optical transduction method in which the analyte binding produces a reduction (turn-off), enhancement (turn-on), or wavelength shift in the emission is considered to be a highly sensitive and useful method.

In general, fluorescent molecules which are highly emissive in the solution state usually, have very low emission quantum yield in the solid or film state.

However, for the vapor phase detection, the film containing fluorophore needs to be optimally emissive. This is one of the reasons for non-availability of suitable sensory material for vapor phase sensing.[20-22] Fluorophores containing aromatic organic molecules with large π-electron cloud are generally utilized for sensing electron deficient oxidative analyte molecules like nitro compounds.[21,23] On the contrary, amines are usually considered as a reductive analyte and it required a detection system with electron deficient functionality combined with high fluorescence quantum yield in the solid or film state. Thus, a suitable choice of functionality is very important for developing these sensors.

It is well documented that the fluorescence quenching by self-assembled systems have several advantages over polymers. Recently, Zhang et. al. have reported fluorescent nanofibril materials fabricated from triphenylamine functionalized *β*-diketone-boron difluoride which are capable of fast and efficient detection of certain organic amine vapors.[24] The electron transfer along these 1D fibers takes place more effectively which results in amplified quenching of the fluorescence emission. In this case, authors have prepared nanofibrils of triphenylamine functionalized *β*-diketone-boron difluoride **1**, which self-assembled via rapid solution dispersion on silicon wafer substrate exhibiting intense red emission (Figure 3b.1). The nanofibril-based film showed rapid and efficient fluorescence quenching upon exposure to gaseous amines (such as *n*-butylamine, dibutylamine, tributylamine, triethylamine, cyclohexylamine, hydrazine, aniline and *N*,*N*-dimethylaniline) and pyridine, while no obvious fluorescence quenching was observed for other common reagents, including *n*-hexane, toluene, methanol,

ethanol, water, acetone, acetonitrile, chloroform, tetrahydrofuran, nitrobenzene, acetic acid and anisole. Therefore, the nanofibrils based on compound **1** could selectively sense volatile organic amines and pyridine. Authors have explained that, the quenching of fluorescence of the nanofibrils of **1** in response to amine is due to the weak B-N interaction (the NH_2 group of aniline and B atom of compound **1**).

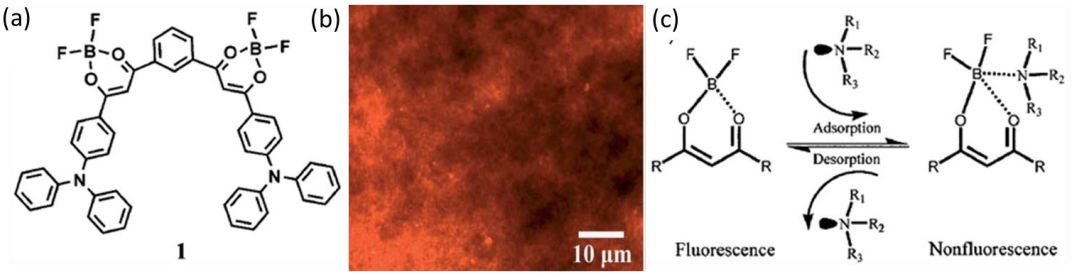

Figure 3b.1. a) Structure of the β-diketone-boron difluoride, **1**, b) fluorescence microscopy images (λ_{ex} = 510–550 nm) of the nanofibrils fabricated from compound **1** and c) proposed mechanism for the fluorescence quenching and recovery of **1** towards gaseous amines. (Adapted with permission from ref. 24. Copyright 2012 The Royal Society of Chemistry.)

Perylene bisimide (PBI) molecule, which is an *n*-type semiconductor material and is well known to form strong assembly by π-π stacking. PBI molecules have been widely used as liquid crystals, organogels, electron acceptors and also in organic electronic devices.[25-29] Applications of these molecules have been extended further to the field of solid-state optical sensing as recently reported by Zang and co-workers for vapor phase probing of organic amines.[30-31] Authors have demonstrated that self-assembled perylene bisimide (PBI) forms 1D nanofibers which have optimum fluorescent emission in the film state and can effectively respond to volatile amine substances. Nanofibrils are fabricated from an unsymmetrical perylene monoimide molecule **2** (Figure 3b.2). The extended 1D molecular

arrangement obtained for **2** is due to the π-π interaction between the perylene backbones and the hydrophobic interaction between the side chains. When prepared from hydrophilic solvents, the surfaces of the nanofibers are exposed of the anhydride moieties that are hydrophilic in nature. Such nanofibers have strong affinity for amines through H-bonding and for donor-acceptor charge transfer interactions. This mesh like fibers has high surface area and possesses porosity on a larger scale (Figure 3b.2c). Hence, upon exposure to the saturated vapors of aniline, the fluorescence of the nanofibers gets quenched in almost 100% (Figure 3b.2b). The fluorescence quenching thus observed is due to a photoinduced electron transfer process, where the electron transfer is driven by the favorable energy difference between the HOMO of the aniline and the HOMO of the molecule **2**.

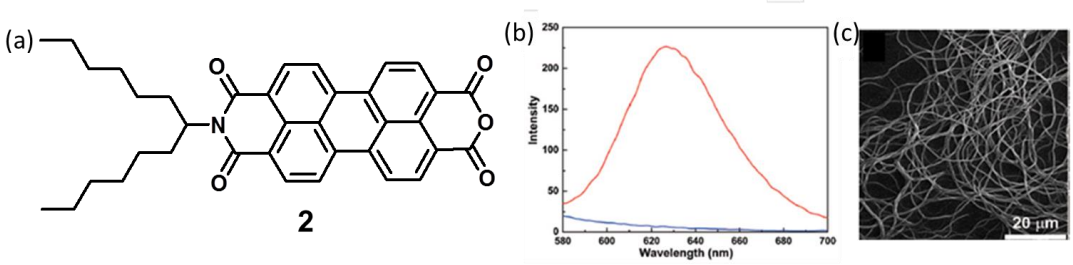

Figure 3b.2. a) Structure of **2**. b) Fluorescence spectra of a nanofibril film before (red) and after (blue) exposure to the saturated vapor of aniline (880 ppm) for 10 s. c) SEM image of a nanofibril film deposited on a glass slide. (Adapted with permission from ref. 30. Copyright 2008 American Chemical Society.)

In another report by Jiang and co-workers, supramolecular assembly from PBI and cyclodextrin conjugate (**3**) has been used for the solid-state fluorescence sensing of amine vapors. (Figure 3b.3).[32] In this case, the PBI part acts as the fluorescence probe since it has good emission quantum yield in the solid-state whereas *β*-

cyclodextrin acts as the binding site for the analytes. In presence of saturated amine vapors, the conjugate **3** embedded in poly(vinylidene difluoride) (PVDF) matrix exhibited efficient fluorescence quenching in just 10 seconds. The advantage of this solid-state fluorescence sensing system is the presence of specific binding sites for the analytes based on the cyclodextrin receptors and the gaseous molecules are accumulated into the cavities of β-cyclodextrin. The fluorescence changes are attributed to the analyte binding and the concomitant changes in the packing of the molecules. Inclusion of analytes into the cyclodextrin cavity may change the distance between the perylene backbones and thus alter the fluorescence.

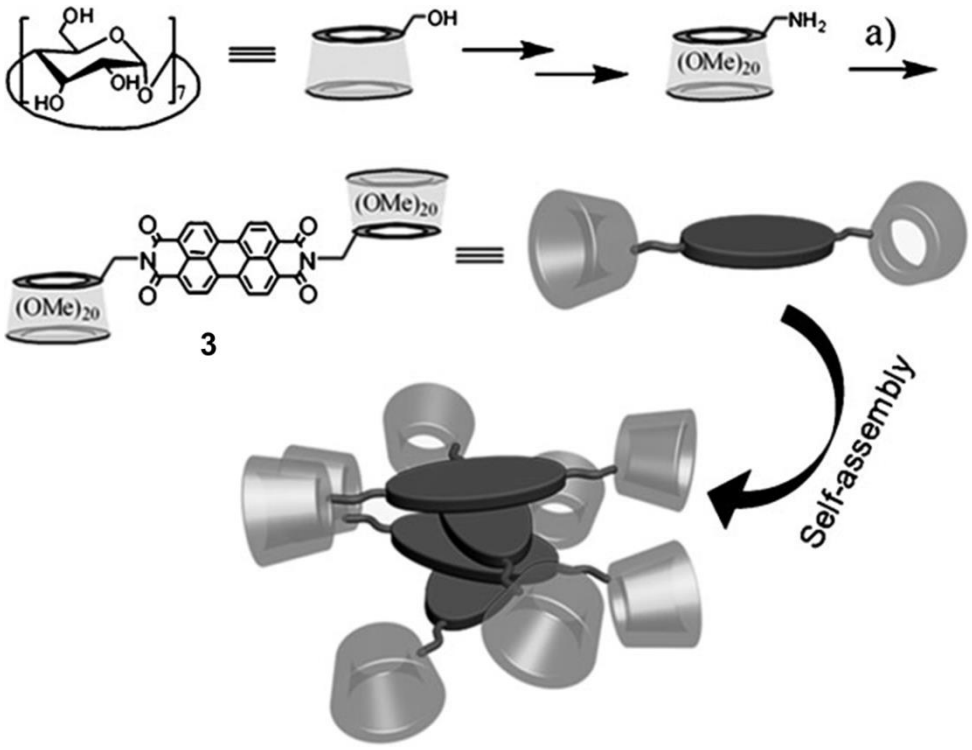

Figure 3b.3. The synthetic route and structural illustration of **3** and its self-assembly mode. Reagents: a) perylene-3,4,9,10-tetracarboxylic acid bisanhydride, zinc acetate, and pyridine, 100 °C. (Adapted with permission from ref. 32. Copyright 2009 WILEY-VCH.)

Herein, we attempted to fabricate a new type of nanofibers from an *n*-type material that could potentially be used for the efficient sensing of reductive analytes via electron transfer based fluorescence quenching mechanism. For this purpose, we have synthesized a C_3-symmetrical perylene bisimide molecule, ***C*$_3$PBI** (Figure 3b.4) through a multistep synthetic process starting from 3,4,9,10-perylene-tetracarboxylic dianhydride (Scheme 3b.1). The self-assembly properties of ***C*$_3$PBI** and its interaction with electron donating analytes such as aromatic amines were studied. PBI represent a robust class of a *n*-type organic material with strong photostability,[33-36] which is particularly desirable for being used in optical sensing or probing, with performance sustainability and reproducibility.

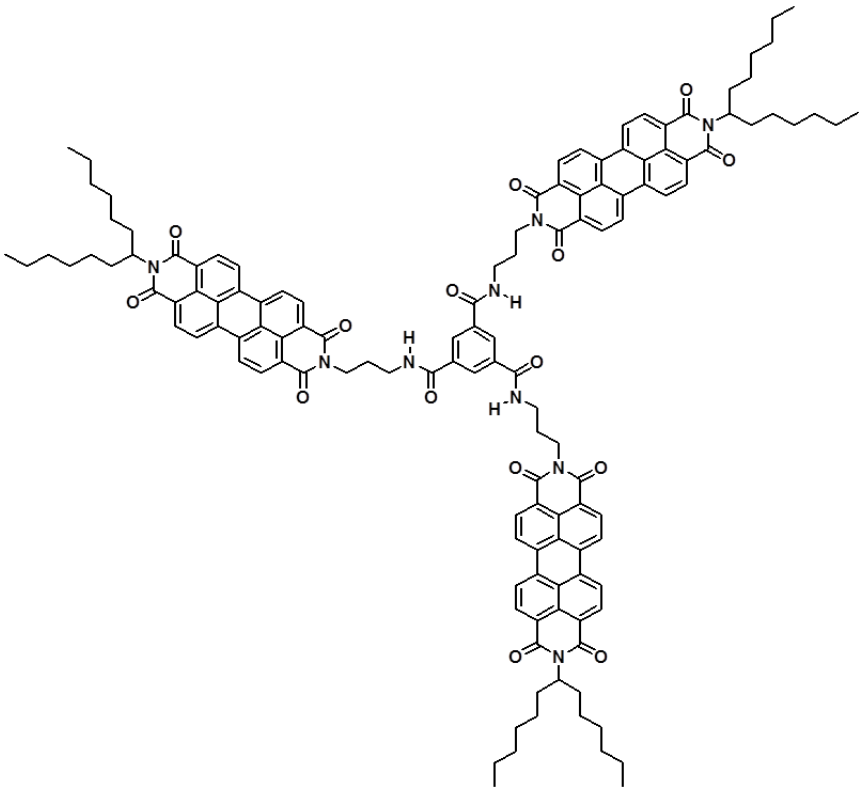

Figure 3b.4. Molecular structure of ***C*$_3$PBI** molecule.

The molecule is designed to have non-planar structure by connecting the PBI part of the molecule to the trimesic acid moiety via amide bonds using a flexible alkyl chain. The presence of this flexible alkyl chain makes the molecule non-planar. However, self-assembly of the molecule leads to planar structure which significantly enhances the fluorescence intensity. As a result, considerable emission intensity was observed in the film state. The swallow-tail connected to the periphery of the disc-like molecule improved its solubility in most of the organic solvents.

3b.3. Results and Discussion

3b.3.1. Synthesis of C_3PBI

The synthesis of ***C*$_3$PBI** is carried out by the strategy shown in the Scheme 3b.1. 1-Hexylheptyl amine[37] was treated with the perylene dianhydride **4** to get the symmetrically substituted PBI **5**, which upon partial hydrolysis with potassium hydroxide in *tert*-butanol yielded the perylene monoanhydride **6**. Subsequently, **6** was functionalized with *N*-*Boc*-1,3-propanediamine. The protected amine derivative **7** thus obtained was converted into the free amine **8** by removing the *Boc* protection with an excess of trifluoroacetic acid (TFA). The unsymmetrical PBI amine derivative **8** was then converted to ***C*$_3$PBI** by treating with trimesic acid trichloride in presence of triethyl amine at room temperature. The final product was obtained in 45% yield. The intermediates and the products are characterized using FT-IR, ^{1}H and ^{13}C NMR spectroscopies and MALDI-TOF spectrometry, after rigorous purification.

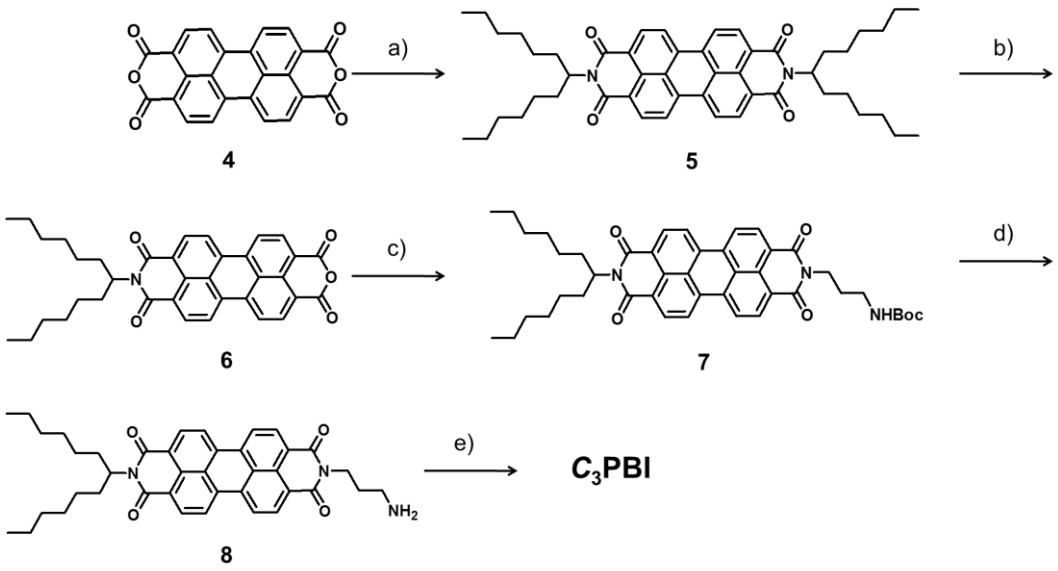

Scheme 3b.1. Synthesis of ***C*$_3$PBI**. (a) 1-Hexylheptylamine, DMF/imidazole, 110 °C, 2 h, 65%; (b) KOH, *tert*-butanol, 90 °C, 30 min, 40%; (c) *Boc*-1,3-diaminopropane, DMF/imidazole, 95 °C, 18 h, 52%; (d) TFA, CH_2Cl_2; r.t., 2 h, 77%; (e) trimesic acid trichloride, Et_3N, dry CH_2Cl_2, r.t., 8 h, 50%.

3b.3.2. Self-assembly of *C*$_3$PBI

In order to understand the self-assembly properties of ***C*$_3$PBI**, the photophysical properties of the molecule were analysed by monitoring the absorption and emission in different solvents (Figure 3b.5a). ***C*$_3$PBI** showed solubility in most of the common organic solvents. However, depending on the solvent, some differences in absorption and emission properties of ***C*$_3$PBI** were noticed. In THF, ***C*$_3$PBI** showed an absorption profile with three bands centered at 460, 490 and 523 nm (Figure 3b.5a). However, in the case of toluene, the absorption maxima were observed at 468, 497 and 535 nm, respectively (Figure 3b.5a). These absorption bands can be attributed to ($\nu_0 \rightarrow \nu_2$), ($\nu_0 \rightarrow \nu_1$) and ($\nu_0 \rightarrow \nu_0$), vibronic transitions of PBI molecule. On changing from THF to toluene, these bands underwent a red-shift with a change

in the ratio of $A^{(0\rightarrow0)}/A^{(0\rightarrow1)}$ bands. The decrease in the ratio of $A^{(0\rightarrow0)}/A^{(0\rightarrow1)}$ suggest that in toluene (0.88) and THF (0.63) ***C*$_3$PBI** exist in self-assembled and monomeric states, respectively. The formation of aggregates was further confirmed by temperature dependent absorption spectral studies of the molecule in toluene (Figure 3b.5b). On increasing the temperature from 15 to 90 °C, the absorption spectrum showed gradual changes and at 90 °C, the spectrum look almost similar to that in THF. Specifically, the band at 535 nm displayed a blue shift with increase in the absorbance through an isosbestic point at 545 nm. These observations clearly indicate that at low temperatures, ***C*$_3$PBI** exists as aggregates in toluene and gets converted into its monomeric form at higher temperatures.

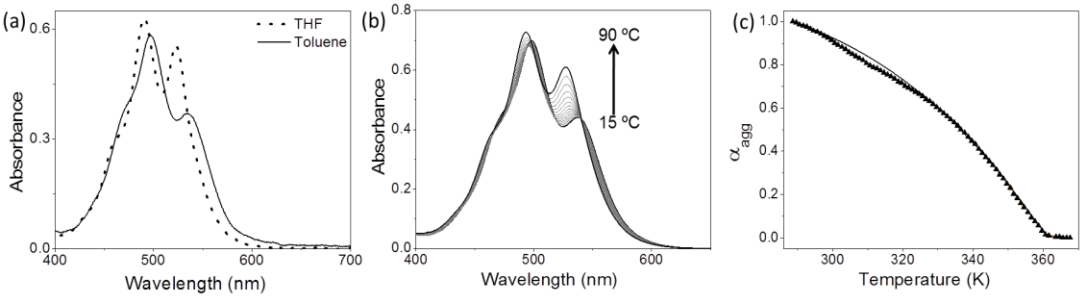

Figure 3b.5. (a) Absorption spectrum of ***C*$_3$PBI** in THF and toluene (1×10^{-4} M). (b) Temperature dependent absorption spectra of ***C*$_3$PBI** in toluene (1×10^{-4} M). (c) Plot of the fraction of aggregates (α_{agg}) against temperature (absorbance was monitored at 527 nm).

Further, to understand the mechanism of self-assembly process, we carried out the variable temperature studies of ***C*$_3$PBI** by monitoring the absorbance at 527 nm (Figure 3b.5c). For this study, the heating rate was kept constant as 1 K min^{-1}. No hysteresis was observed when the solution was heated back to the monomeric state, indicating that the thermodynamic self-assembly process is reversible. The spectrum is then normalized in order to obtain the fraction of aggregates (α_{agg}). The fraction

of aggregates is then plotted against temperature. From the plot of the fraction of aggregates against temperature, it is clear that the ***C*$_3$PBI** aggregates through a cooperative mechanism. In the case of cooperative processes, an unfavorable activation step, governed by equilibrium constant K_a, precedes chain elongation or growth with equilibrium constant K_e. If K_a « 1, the polymerization becomes cooperative which is reminiscent of an actual phase transition, implying a sharp polymerization point below which assemblies do not form in appreciable numbers.

In order to demonstrate the involvement of nucleation and growth process in the observed self-assembly of ***C*$_3$PBI**, we analyzed the curve on the basis of the model proposed by van der Schoot, Schenning and Meijer.[38,39] According to this model, in the *elongation* regime, the fraction of aggregated species (α_{agg}) can be defined by the following equation:

$$\alpha_{\mathrm{agg}} = \alpha_{\mathrm{SAT}}\left(1 - \exp\left[\frac{-h_e}{RT_e^2}(T - T_e)\right]\right) \qquad (3b.1)$$

where, ΔH_e is the enthalpy corresponding to the aggregation (elongation) process, T is the absolute temperature, T_e is the elongation temperature, and R is the ideal gas constant. α_{sat} is a parameter introduced to ensure that $\alpha_{agg}/\alpha_{sat}$ does not exceed unity. On the other hand, in the *nucleation* regime, the fraction of aggregated species (α_{agg}) can be defined by:

$$\alpha_{\mathrm{agg}} = K_a^{1/3}\exp\left[\left(2/3\,K_a^{-1/3} - 1\right)\frac{h_e}{RT_e^2}(T - T_e)\right] \qquad (3b.2)$$

where, K_a is the dimensionless equilibrium constant of the activation step at the

elongation temperature. The average length of the stack $<N_n>$ averaged over the nucleated species at the T_e is given by:

$$\langle N_n(T_e)\rangle = \frac{1}{(K_a)^{1/3}} \qquad (3b.3)$$

Here, the melting transition temperature (T_m) is found to be 336.5 K. High degree of cooperativity is observed from the small value of K_a, the equilibrium constant for the nucleation step which is determined as 10^{-6}. The other thermodynamic data for the self-assembly process are tabulated below (Table 3b.1).

Table 3b.1. Thermodynamic parameters calculated for the self-assembly of ***C*$_3$PBI** using cooperative model.

Molecule	C (M)	ΔH_e (KJ mol^{-1})	ΔS_e (J mol^{-1} K^{-1})	T_e (K)	T_m (K)	K_a
***C*$_3$PBI**	1×10^{-4}	-27.47	-140.9	360.58	336.55	10^{-6}

C the concentration, ΔH_e and ΔS_e, respectively are the change in enthalpy and entropy during elongation process, T_m the melting transition temperature, T_e the elongation temperature and K_a, the degree of cooperativity.

The emission spectrum of ***C*$_3$PBI** in toluene (1×10^{-4} M) at room temperature exhibited an enhancement in the intensity when compared to that in THF which can be attributed to aggregation of the molecule (Figure 3b.6). To verify this observation, the temperature dependent emission studies in toluene were carried out. At higher temperatures, the ***C*$_3$PBI** exists in monomeric state with less fluorescence intensity. As the temperature was lowered, the molecule starts aggregating with increase in fluorescence intensity. This result reveals that ***C*$_3$PBI** has the characteristic of aggregation induced enhanced emission (AIEE).[40, 41] As the

temperature is decreased, the molecules attain planarity due to aggregation and as a result the emission intensity increased.

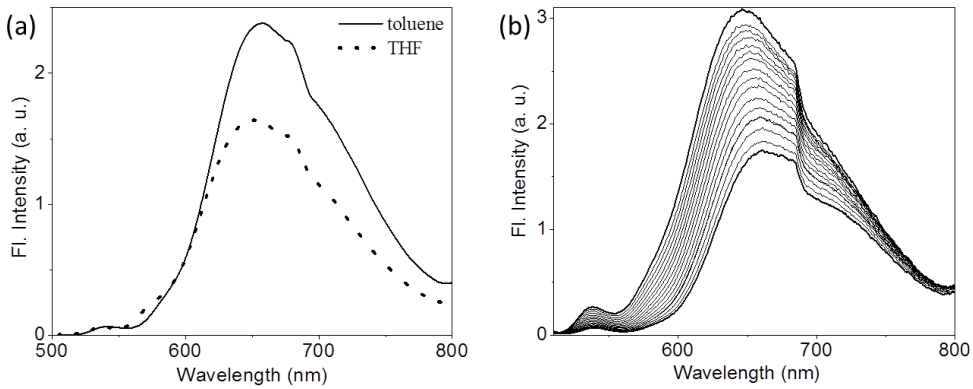

Figure 3b.6. (a) Emission spectrum of ***C*$_3$PBI** in THF and toluene (1×10^{-4} M). (b) Temperature dependent emission spectra of ***C*$_3$PBI** in toluene (1×10^{-4} M).

Subsequently, we studied the photophysical properties of the molecule in the film state. Figure 3b.7 shows the absorption and emission spectra taken after drop casting a 10^{-4} M solution of ***C*$_3$PBI** in toluene on a glass substrate. In comparison to the emission spectrum taken in solution state, the film state shows red shift in the emission maximum.

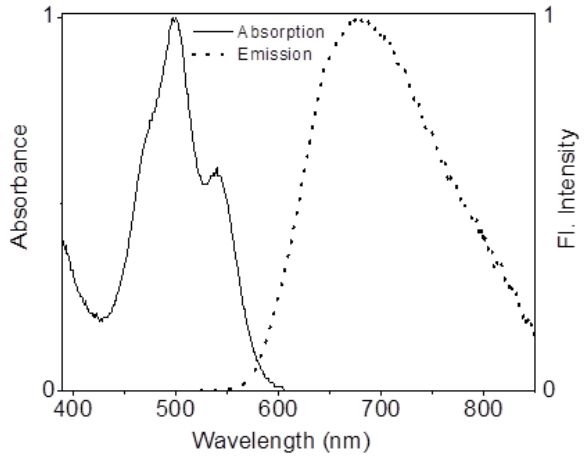

Figure 3b.7. The absorption (—) and fluorescence (····) spectra of ***C*$_3$PBI** in the film state.

The morphological study of the nanostructures formed by ***C*$_3$PBI** was then carried out. Atomic force microscopy (AFM) and scanning electron microscopy (SEM) studies show that ***C*$_3$PBI** forms nanofibers on different substrates (Figure 3b.8). The average diameter of the fiber is ~200 nm as determined by AFM section analysis. The length of the fiber extends to several micrometers. The extended 1D molecular arrangement obtained for ***C*$_3$PBI** is likely dominated by the π-π interaction between the perylene backbones. The nanofibers fabricated from ***C*$_3$PBI** show strong red fluorescence.

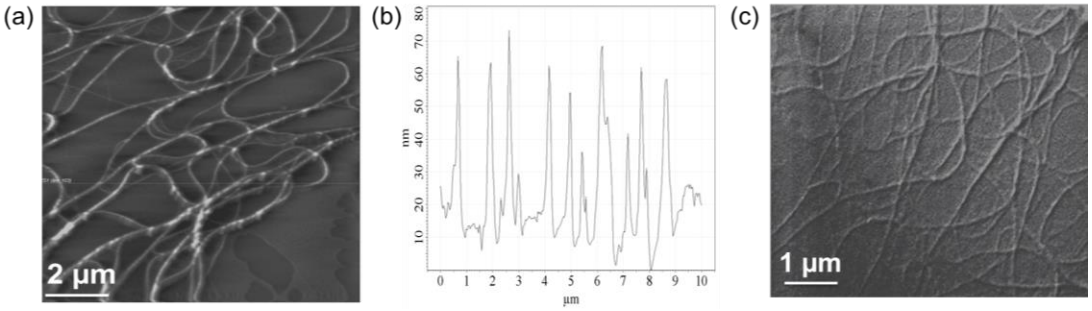

Figure 3b.8. (a) AFM (b) AFM height profile and (c) SEM images of ***C*$_3$PBI** by dropcasting 10^{-4} M solution on mica substrate.

The electronic property of the molecule in the film state was then measured and the HOMO-LUMO energy levels were calculated. A gap around 2.13 eV was calculated with HOMO at -6.4 eV and LUMO at -4.27 eV. Figure 3b.9 shows the energy levels of the ***C*$_3$PBI** and aniline (analyte), which suggests favorable electron transfer from aniline to the photoexcited ***C*$_3$PBI**. Hence, these nanofibers with red fluorescence can be used in fluorescence sensing of aromatic amines.

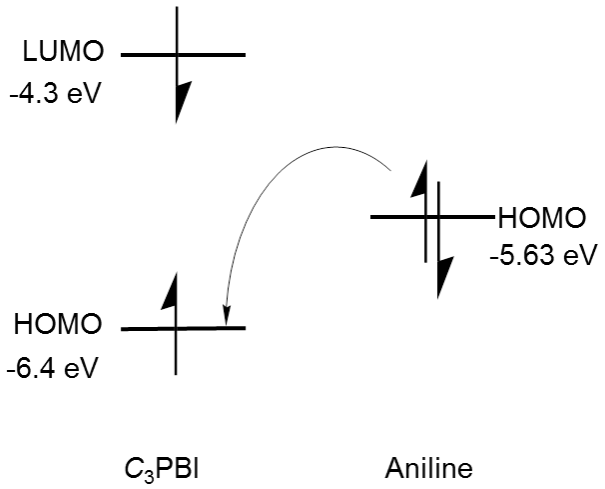

Figure 3b.9. Energy level diagram of ***C*$_3$PBI** and aniline shows favorable electron transfer from amine to the photoexcited ***C*$_3$PBI**. The same diagram applies to the other amines, while the reducing power (or the HOMO level) would be different from that of aniline.

3b.3.3. Sensing of Volatile Amines

The nanofibers deposited onto the substrate, bundle to form a film that provides a large surface area with sufficient porosity. This large surface area with porosity helps in adsorption and the expedient diffusion of gaseous analytes, which leads to efficient probing with high sensitivity and fast response. For this purpose, the nanofibers on the substrate were prepared by drop-casting 10^{-4} M solution of ***C*$_3$PBI** in toluene. It was then kept in the open air to dry the solvent and then in vacuum for overnight. The saturated vapors of amines were generated by keeping around 10 mg of the amine covered with a piece of cotton inside a vial with its top capped, and was kept overnight. The nanofiber deposited film was then placed over the vial containing saturated vapor of the analyte for a few seconds at room temperature. The fluorescence from the nanofiber was then monitored by using front-face

technique. Among the different amines analyzed, *o*-toluidine gave the fastest response when compared to the other amines.

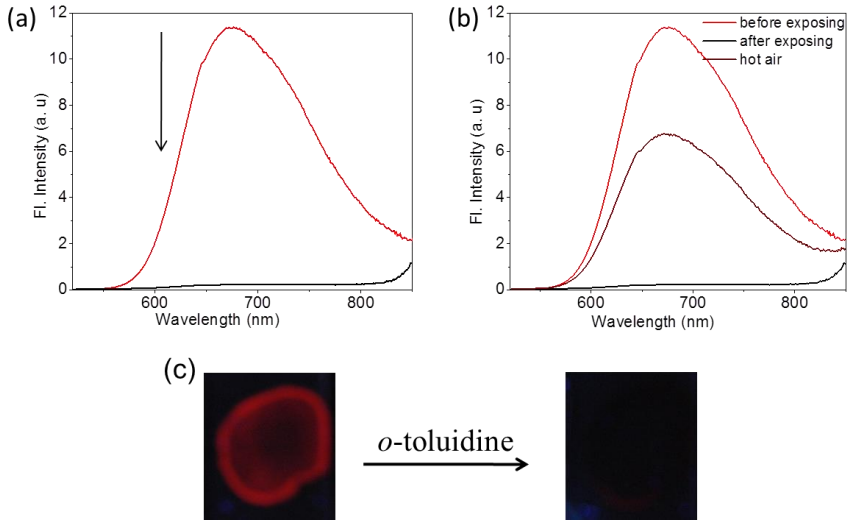

Figure 3b.10. (a) Emission spectra of ***C*$_3$PBI** films before and after exposing to vapors of *o*-toluidine. (b) Emission spectrum after exposing the film to the methanol vapor. (—) before exposing to *o*-toluidine, (—) after exposing to *o*-toluidine, (—) after exposing to the methanol vapor (λ_{ex} = 490 nm). (c) Photographs showing the fluorescence of the ***C*$_3$PBI** films before and after exposure *o*-toluidine.

Figure 3b.10 shows the emission spectrum of ***C*$_3$PBI** before and after exposure to *o*-toluidine. More than 90% quenching of the red fluorescence of the nanofiber was observed when the film was exposed to *o*-toluidine vapor for five seconds (Figure 3b.10a). The red fluorescence of the ***C*$_3$PBI** nanofiber can be recovered by exposing the film to methanol vapor (Figure 3b.10b). However, only 50% of the initial emission intensity could be recovered. Figure 3b.10c shows a photograph of a film prepared from ***C*$_3$PBI** by drop casting the toluene solution under UV light. The red emission was quenched when exposed to *o*-toluidine vapor and the film shows no emission (Figure 3b.10c). The same experiment was carried out using other

amines such as aniline, benzyl amine, phenylene diammines, hydrazine, etc. Aniline gave almost 75% quenching for the first five seconds (Figure 3b.11a). Another aromatic amine, *o*-phenylene diamine showed almost 68% quenching (Figure 3b.11b).

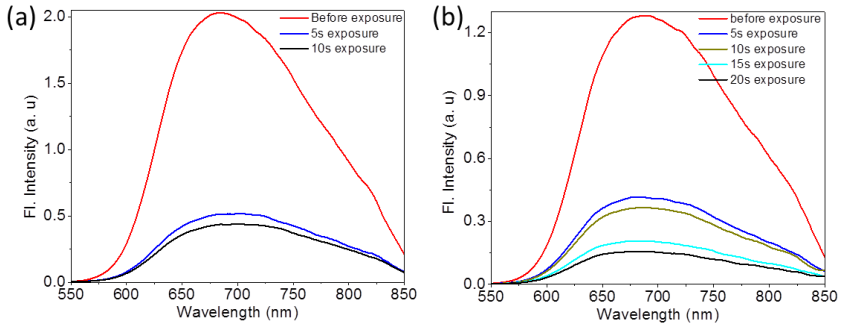

Figure 3b.11. The emission spectra of ***C*$_3$PBI** films before and after exposing to vapors of (a) aniline and (b) *o*-phenylene diamine, λ_{ex} = 490 nm.

Aamines such as benzylamine and hydrazine also could quench the red emission of the ***C*$_3$PBI** nanofiber, however with less efficiency (Figure 3b.12). Benzylamine showed 45% quenching (Figure 3b.12a) and hydrazine showed 60% quenching (Figure 3b.12b).

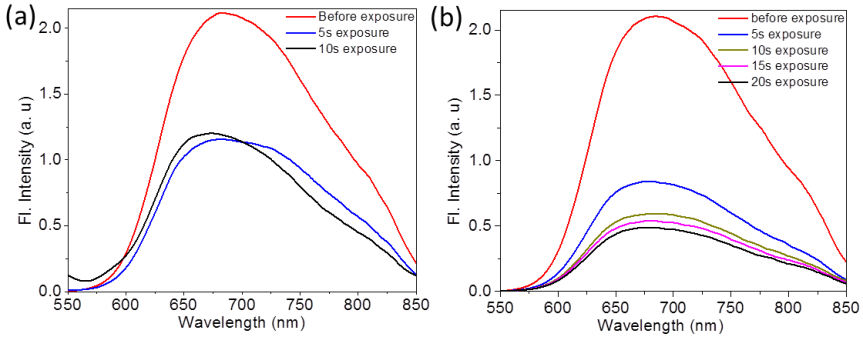

Figure 3b.12. The emission spectra of ***C*$_3$PBI** films before and after exposing to vapors of (a) benzylamine and (b) hydrazine, λ_{ex} = 490 nm.

The observed quenching of fluorescence emission is by virtue of the expedient diffusion of gaseous analyte molecules within the matrix of the mesh-like, porous film formed by the entangled ***C*$_3$PBI** nanofibers. The vapor phase probing was dominated by the morphology and topology of the obtained material and the mechanism of quenching is obviously due to photoinduced electron transfer between the electron donating analyte molecule and the electron accepting PBI molecule. The electron donation ability and the vapor pressure of the analyte are the two important factors that affect the selectivity and the sensitivity of this PBI based sensor. In the case of aromatic amines, the electron donating capability and the substituents on the aromatic ring determine the selectivity. *o*-Toluidine with a methyl substituent on the benzene ring, have more electron donation ability than aniline. When compared to aniline, *o*-toluidine shows faster response and better fluorescence quenching. *o*-Phenylenediamine, with two amino groups on benzene ring showed less quenching when compared to aniline and *o*-toluidine. Lesser quenching even in the presence of two amino groups is due to the low vapor pressure of the compound. Nonaromatic amines also cause quenching of ***C*$_3$PBI** emission but with less efficiency. Hydrazine showed 60% quenching in the first 5 seconds which can be due to its high vapor pressure.

3b.4. Conclusions

In summary, we have designed and synthesized a C_3-symmetrical PBI derivative, ***C*$_3$PBI**. The molecule which self-assembles in toluene, is emissive both in the aggregated and the film states. Self-assembled fibers of diameter around 200 nm are formed when a toluene solution is dropcast over both mica and glass surfaces. The

fluorescence of the molecule in the nanofiber state is quenched up on exposing to the vapors of amino compounds. The fluorescence quenching is due to photoinduced electron transfer from the donor analyte to the acceptor fluorophore molecule. The extend of fluorescence quenching is decided by the electron donating ability of the analytes. Since the detection is in the vapor phase, the fluorescence quenching efficiency also depends on the vapor pressure of the analytes. Among different amines analyzed, *o*-toluidine shows maximum fluorescence quenching, which is due to its high vapor pressure and electron donating ability.

3b.5. Materials and Methods

3b.5.1. General

Unless otherwise stated, all materials and reagents were purchased from commercial suppliers. The solvents and reagents were purified and dried by standard methods prior to use. Reactions were monitored using thin layer chromatography (TLC) on silica gel 60 F_{254} (0.2 mm; Merck). Visualization was accomplished using UV lamp (365 nm). Column chromatography was performed on glass columns of different sizes, hand packed with silica gel 60 (particle size 0.040–0.063 mm, Merck).

3b.5.2. Instrumentation

The details of the melting point, FT-IR, ^{1}H, ^{13}C NMR, MALD-TOF, UV/Vis absorption spectrophotometer, spectrofluorimeter, AFM, and SEM instruments are described in the experimental section (Section 2.5.2) of Chapter 2. The samples for photoelectron yield spectroscopy (PYS) were prepared on ITO coated glass plates by solution drop casting (chlorobenzene solution). Prior to the measurements, substrates were dried in a vacuum oven for 2 h at 50 °C. The PYS experiments were

done on a RIKEN Keiki Co., Ltd., model AC-3 under high vacuum (1×10^{-3} M pa). The instrument was calibrated using standard aluminium substrate.

3b.6. Synthesis and Characterization

3b.6.1. Synthesis of *N,N'*-Bis(1-hexylheptyl)-3,4,9,10-perylene dicarboxamide (5)

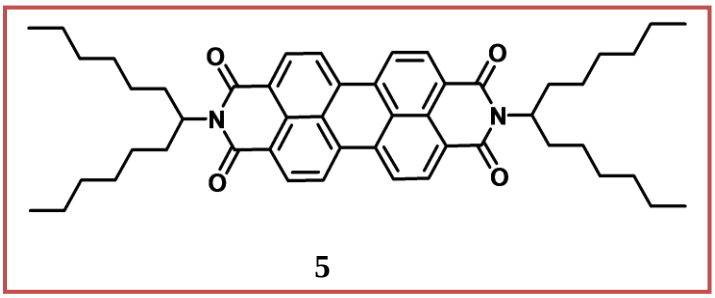

5

A mixture of perylene-3,4,9,10-tetracarboxylic dianhydride (PTCDA) (392 mg, 1 mmol), zinc acetate (164.62 mg, 0.75 mmol), imidazole (4 g, used as the solvent) and hexylheptyl amine (600 mg, 3 mmol) was vigorously stirred at 160 °C for 2 h. After cooling to room temperature, the reaction mixture was dissolved in minimum amount of THF and precipitated by adding 300 mL of 2N HCl/MeOH 2:1 v/v. The precipitate was collected by filtration, washed with water followed by methanol and dried at 80 °C in vacuum. The crude product was further purified by silica column chromatography using 50% $CHCl_3$/*n*-hexane as the eluent with 65% yield. **^{1}H NMR** (300 MHz, $CDCl_3$, TMS): δ = 8.70-8.64 (m, 8H), 5.21-5.15 (m, 2H), 2.27-2.21 (m, 4H,), 1.87-1.83 (m, 4H), 1.33-1.22 (m, 32H), 0.83-0.81 (t, 12H) ppm. **FT-IR** (KBr) υ_{max} = 1693, 1656 (O=CN), 1592 (C=C aromatic), 806, 748 (C-H aromatic), 2862, 2924, 2956 (C-H alkyl), 1344 (C-N) cm^{-1}. **MS (FAB)** (m/z): $[M+H]^+$ calculated for $C_{50}H_{62}N_2O_4$ is 756.04; found 755.23.

3b.6.2. Synthesis of *N*-(1-hexylheptyl)perylene-3,4,9,10-tetracarboxylic-3,4-anhydride-9,10-imide (6)

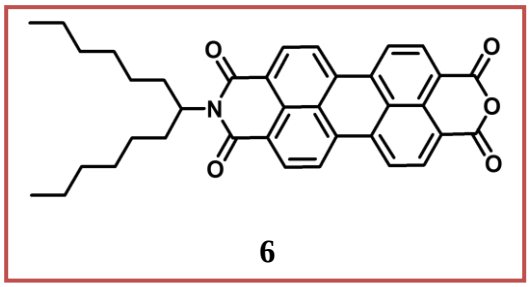

6

In a 250 mL round bottom flask, (500 mg, 0.66 mmol) of PBI was suspended in a 70 mL of *t*-BuOH and treated with (122 mg, 2.18 mmol) of 85% KOH. The reaction mixture was heated with vigorous stirring to reflux until the solution turned dark purple for approximately 30 minutes. The mixture was cooled to room temperature, treated with 80 mL acetic acid and 40 mL 2N HCl and stirred overnight. The dark red precipitate obtained was washed with water and dried at 130 °C. The solid was suspended in 150 mL 10% potassium carbonate solution and heated to reflux for approximately 30 minutes. The mixture was then cooled and filtered. The filter cake was washed with warm 10% potassium carbonate until the filtrate was clear, rinsed twice with approximately 100 mL of 2N HCl followed with water and dried at 130 °C. The solid was then suspended in 100 mL boiling water. Triethylamine was added to this suspension until a dark purple solution of the desired product was formed. Remaining starting material was filtered off and the dark filtrate was acidified with 30 mL 2N HCl and stirred overnight. The resulted dark precipitate was filtered and rinsed with water and dried. The resulting crude product was purified by silica column chromatography using chloroform as the eluent with 40% yield. **^{1}H NMR** (300 MHz, $CDCl_3$, TMS): δ = 8.73-8.67 (m, 6H), 8.01 (m, 2H), 5.21-5.15 (m, 1H), 2.27-2.21 (m, 2H), 1.87-1.83 (m, 2H), 1.33-1.22

(m, 16H), 0.83-0.81 (t, 12H) ppm. **MS (FAB)** (m/z): $[M+H]^+$ calculated for $C_{37}H_{35}NO_5$ is 574.68; found 574.10.

3b.6.3. Synthesis of the PBI 7

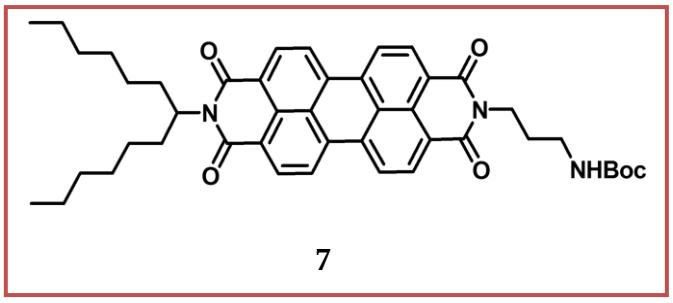

7

Under argon atmosphere, the compound **6**, (100 mg, 0.174 mmol), *N*-Boc diaminopropane (28.7 mg, 0.13 mmol), and zinc acetate (~10 mg) were dissolved in dry DMF (130 mL) and stirred at 90 °C for 18 h. After evaporation of the solvent under reduced pressure, the product was dissolved in chloroform and washed with an aqueous citric acid solution followed by brine. The organic layer was dried and evaporated in vacuo to dryness. The resulted red solid was subjected to silica column chromatography (0.5-1% MeOH in $CHCl_3$) to yield **7**, slightly contaminated with *N*,*N'*-di-Boc-1,3-propyldiamine which was in low quantities present in the starting material *N*-Boc-1,3-propyldiamine. Without further purification, PBI **7** was used to prepare the PBI **8**. **MS (FAB)** (m/z): $[M+H]^+$ calculated for $C_{45}H_{51}N_3O_6$ is 730.90; found 732.01.

3b.6.4. Synthesis of the PBI 8

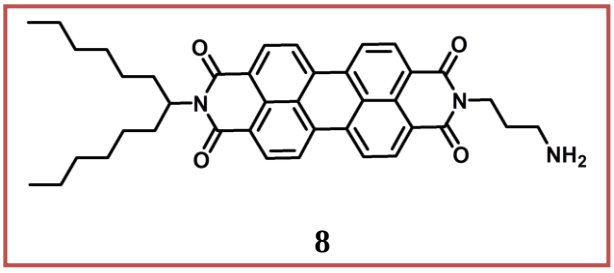

8

To a solution of the PBI **7** in dichloromethane, trifluoroacetic acid was added and the mixture was stirred for 2 h. After evaporation of the solvent in vacuum, the product was dissolved in dichloromethane and subsequently washed with an aqueous 10% sodium bicarbonate solution and

brine. The organic layer was dried using sodium sulfate and finally evaporated in vacuum to yield the PBI **11** as a red solid in an overall yield of 77% starting from **6**. **^{1}H NMR** (300 MHz, CD_3CN): δ = 8.46-8.43 (m, 6H), 8.39-8.38 (m, 2H), 5.21-5.15 (m, 1H), 4.22-4.2 (t, 2H), 3.24 (m, 2H), 2.26-2.08 (m, 4H), 1.89 (q, 2H), 1.34-1.26 (m, 16H), 0.85-0.83 (t, 6H) ppm. **FT-IR** (KBr) υ_{max} = 1693, 1656 (O=CN), 1592 (C=C aromatic), 806, 748 (C-H aromatic), 2862, 2924, 2956 (C-H alkyl), 1344 (C-N), 3341 (N-H amine) cm^{-1}. **MS (FAB)** (m/z): $[M+H]^+$ calculated for $C_{40}H_{43}N_3O_4$ is 630.79; found 630.43.

3b.6.5. Synthesis of *C*$_3$PBI

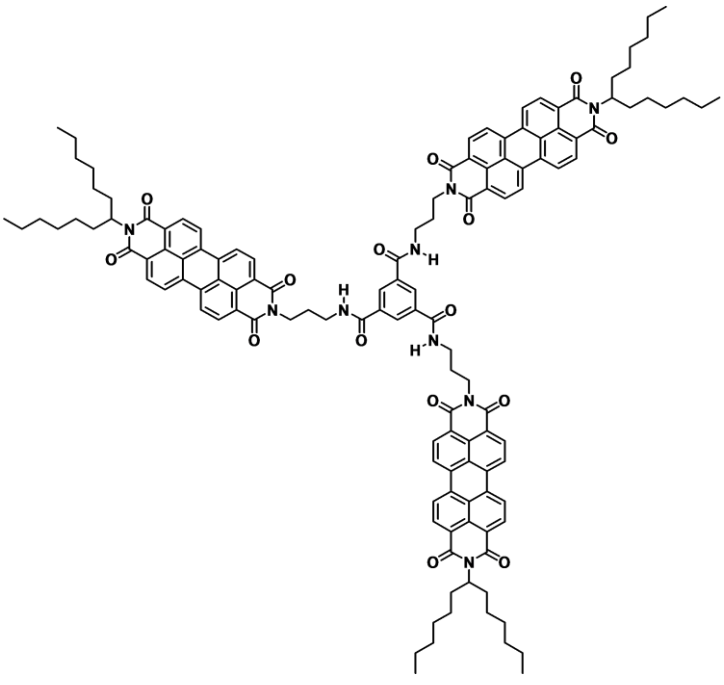

***C*$_3$PBI**

To a solution of the PBI amine, **8** (400 mg, 0.63 mmol) and triethylamine (0.5 mL) in dry dichloromethane (10 mL), a solution of 1, 3, 5- benzenetricarboxylic acid

chloride (56.2 mg, 0.21 mmol) was added dropwise. The mixture was stirred for 6 h and the solvent was evaporated in vacuum. Purification by column chromatography on silica gel (dichloromethane–*n*-hexane 3:1) and BioBeads SX-1 (dichloromethane) yielded the pure ***C*$_3$PBI** in an overall yield of 50%. **^{1}H NMR** (300 MHz, THF-d_8): δ = 8.72 (s, 3H), 8.44-8.41 (d, 12H), 8.19-8.16 (d, 12H), 7.74 (s, 3H), 5.168 (m, 3H), 4.45-4.35 (t, 6H), 3.74-3.64 (t, 6H), 1.87-1.82 (m, 6H), 1.57-1.37 (m, 62H), 0.845 (t, 18H) ppm. **FT-IR** (KBr) υ_{max} = 1693, 1656 (O=CN), 1592 (C=C aromatic), 806, 748 (C-H aromatic), 3291 (N-H amide), 2862, 2924, 2956 (C-H alkyl), 1344 (C-N) cm^{-1}. **MALDI-TOF-MS**: *m/z* calculated for $C_{129}H_{129}N_9O_{15}$ $[M+H]^+$: 2046.47, found: 2048.18. Anal. Calcd for $C_{129}H_{129}N_9O_{15}$: C, 75.75; H, 6.36; N, 6.16. Found: C, 76.01; H, 6.64; N, 6.57.

3b.7. References

1. Gao, T.; Tillman, E. S.; Lewis, N. S. *Chem. Mater.* **2005**, *17*, 2904–2911.

2. Thomas, S. W.; Swager, T. M. *Adv. Mater*. **2006**, *18*, 1047–1050.

3. Bao, B.; Yuwen, L.; Zheng, X.; Weng, L.; Zhu, X.; Zhan, X.; Wang, L. *J. Mater. Chem.* **2010**, *20*, 9628 –9634.

4. Ajayakumar, M. R.; Mukhopadhyay, P. *Chem. Commun*. **2009**, 3702 –3704.

5. Kçrsten, S.; Mohr, G. J. *Chem. –Eur. J.* **2011**, *17*, 969 –975.

6. Mohr, G. J. *Chem. –Eur. J.* **2004**, *10*, 1082 –1090.

7. Mohr, G. J.; Demuth, C.; Spichinger -Keller, U. E. *Anal. Chem*. **1998**, *70*, 3868 – 3873.

8. Onal, A. *Food Chem*., **2007**, *103*, 1475–1486.

9. Larque, E.; Sabater-Molina, M.; Zamora, S. *Nutrition*, **2007**, *23*, 87–95.

10. Reinert, S.; Mohr, G. J. *Chem. Commun*., **2008**, 2272–2274.

11. Gugliucci, A. *Clin. Chim*. *Acta*, **2004**, *344*, 23–35.

12. Ma, Y. F.; Liu, G. S.; Du, M.; Stayton, I. *Electrophoresis*, **2004**, *25*, 1473–1484.

13. Khuhawar, M. Y.; Qureshi, G. A. *J. Chromatogr. B*, **2001**, *764*, 385–407.

14. Casero, R. A.; Marton, L. J. *Nat. Rev. Drug Discovery*, **2007**, *6*, 373–390.

15. Mateva, L. V.; Petrov, S. S.; St Lozanov, V.; Elenkova, A. P.; Zacharieva, S.; Mitev, V. I. *J. Liq. Chromatogr. Relat. Technol.*, **2008**, *31*, 2128–2140.

16. Paik, M. J.; Kuon, D.; Cho, J.; Kim, K. R. *Amino Acids*, **2009**, *37*, 407–413.

17. Zhang, C.; Suslick, K. S. *J. Am. Chem. Soc.* **2005**, *127*, 11548–11549.

18. Mei, X.; Wolf, C. *J. Am. Chem. Soc.* **2006**, *128*, 13326–13327.

19. Feuster, E. K.; Glass, T. E. *J. Am. Chem. Soc.* **2003**, *125*, 16174–16175.

20. Jenekhe, S. A.; Osaheni, J. A. *Science* **1994**, *265*, 765–768.

21. Langhals, H.; Krotz, O.; Polborn, K.; Mayer, P. *Angew. Chem., Int. Ed.* **2005**, *44*, 2427–2428.

22. Samuel, I. D. W.; Turnbull, G. A. *Chem. Rev*. **2007**, *107*, 1272–1295.

23. Naddo, T.; Che, Y.; Zhang, W.; Balakrishnan, K.; Yang, X.; Yen, M.; Zhao, J.; Moore, J. S.; Zang, L. J. *Am. Chem. Soc*. **2007**, *129*, 6978–6979.

24. Zhang, X.; Liu, X.; Lu, R.; Zhang, H.; Gong, P. *J. Mater. Chem.* **2012**, *22*, 1167–1172.

25. Würthner, F. *Chem. Commun*. **2004**, 1564–1579.

26. Elemans, J. A. A. W.; van Hameren, R.; Nolte, R. J. M.; Rowan, A. E. *Adv. Mater*. **2006**, *18*, 1251–1266.

27. Wasielewski, M. R. *J. Org. Chem.* **2006**, *71*, 5051–5066.

28. Schmidt, R.; Ling, M. M.; Oh, J. H.; Winkler, M.; Könemann, M.; Bao, Z.; Würthner, F. *Adv. Mater.* **2007**, *19*, 3692–3695.

29. Ling, M. M.; Erk, P.; Gomez, M.; Koenemann, M.; Locklin, J.; Bao, Z. *Adv. Mater.* **2007**, *19*, 1123–1127.

30. Che, Y.; Yang, X.; Loser, S.; Zang, L. *Nano Lett.* **2008**, *8*, 2219–2223.

31. Che, Y.; Zang, L. *Chem. Commun.* **2009**, 5106–5108.

32. Liu, Y.; Wang, K.-R.; Guo, D.-S.; Jiang, B.-P. *Adv. Funct. Mater.* **2009**, *19*, 2230–2235.

33. Newman, C. R.; Frisbie, C. D.; da Silva Filho, D. A.; Bredas, J.-L.; Ewbank, P. C.; Mann, K. R. *Chem. Mater.* **2004**, *16*, 4436–4451.

34. Zang, L.; Che, Y.; Moore, J. S. *Acc. Chem. Soc.* **2008**, *41*, 1596–1608.

35. Würthner, F. *Chem. Commun.* **2004**, *14*, 1564–1579.

36. Langhals, H. *Helv. Chim. Acta* **2005**, *88*, 1309–1343.

37. Tadanier, J.; Hallas, R.; Martin, J. R.; Stanaszek, R. S. *Tetrahedron* **1981**, *37*, 1309–1316.

38. Smulders, M. M. J.; Nieuwenhuizen, M. M. L.; de Greef, T. F. A.; van der Schoot, P.; Schenning, A. P. H. J.; Meijer, E. W. *Chem. –Eur. J.* **2010**, *16*, 362–367.

39. Smulders, M. M. J.; Schenning, A. P. H. J.; Meijer, E. W. *J. Am. Chem. Soc.* **2008**, *130*, 606–611.

40. Lim, S.-J.; An, B.-K.; Jung, S. D.; Chung, M.-A.; Park, S. Y. *Angew. Chem., Int. Ed.* **2004**, *43*, 6346.

41. Lim, S.-J.; An, B.-K.; Park, S. Y. *Macromolecules* **2005**, *38*, 6236.

Chapter 4

Sensing of Volatile Organic Compounds by Coaxial Fibers of Self-Sorted Fluorescent Molecular Assemblies

4.1. Abstract

*Detection of different life threatening volatile organic compounds (VOCs) such as carcinogenic molecules is an active area of research. Herein, we report the use of supercoiled supramolecular polymeric fibers of self-sorted donor–acceptor molecules as "turn-off/turn-on" fluorescent sensors for the detection of carcinogenic VOCs. For this purpose, an oligo(p-phenylenevinylene) based C_3-symmetrical donor molecule, **C_3OPV2**, and a perylene bisimide based acceptor molecule, **C_3PBI**, have been utilized. When these two molecules were mixed together in toluene, in contrast to the usual charge transfer (CT) stacking, supramolecular fibers of self-sorted stacks were formed at the molecular level, primarily driven by their distinct self-assembly pathways. However, CT interaction at the macroscopic level allows these fibers to bundle together to form supercoiled ropes. An interfacial photoinduced electron transfer (PET) process from the donor to the acceptor fibers leads to an initial fluorescence quenching, which could be reactivated by exposure to strong donor or acceptor type VOCs to regenerate the respective fluorescence of the individual molecular stacks. Thus, strong donors could regenerate the green fluorescence of **C_3OPV2** stacks and strong acceptors could reactivate the red fluorescence of **C_3PBI** stacks. These supercoiled supramolecular ropes of self-sorted donor–acceptor stacks provide a simple tool for the detection of donor- or acceptor-type VOCs of biological relevance, using a "turn-off/turn-on" fluorescence mechanism as demonstrated by the sensing of o-toluidine, which has been reported as a lung cancer marker.*

4.2. Introduction

Early detection of deadly diseases such as cancer can save the life of millions of people across the globe and hence a prime concern of scientists and clinicians. At the onset of certain diseases, the metabolism of the human body changes to produce several volatile organic molecules in small quantities, some of which can be designated as disease markers.[1-5] Detection of cancer markers and carcinogenic VOCs such as *o*-toluidine, aromatic amines, nitroaromatics etc. are important since tobacco smoke contains a large number of them, which are known to cause bladder cancer.[6] *o*-Toluidine has also been detected in the exhaled air of lung cancer patients.[7] Similarly, detection of electron deficient molecules such as nitroaromatics are important since they are not only considered as explosives but also toxic to living organisms by contaminating air and water.[8-13]

Considering the social relevance of the detection of carcinogenic VOCs, intense research is needed for further development in this area. These considerations have prompted us to explore the potential of fluorescent donor-acceptor assemblies which are designed based on the principles of nanoarchitectonics[14] for sensing of volatile analytes. A number of reports are available for the sensing of VOCs such as aromatic amines[15-20] and nitroaromatics[8-13, 21-27] that generally cause fluorescence quenching of a probe. In this context, self-sorted supramolecular assemblies[28-39] is an ideal platform for the sensing of VOCs. We have earlier shown that fluorescent π-gelators are powerful tools for the attogram level sensing of trinitrotoluene (TNT) on a contact mode[25] and thought of the immense scope for expanding this idea to the

sensing of VOCs of metabolic origin, if the principles of molecular self-assembly and self-sorting are combined.

The application of π-gelators in the detection of nitroaromatics is already discussed in Chapter 3a. Derivatives of perylene bisimide are extensively used for the sensing of aromatic amines[15,16,17,40-42] and is discussed in Chapter 3b.

Usually, when donor and acceptor monomers are mixed, CT induced supramolecular polymers are formed.[43,44] A supramolecular control on the polymerization is difficult in such cases.[45-48] However, suitably functionalized π-systems[35-39] such as oligo(thiophenes) (OTs), oligo(*p*-phenylenevinylene) (OPVs) and perylene bisimides (PBIs) are known to form self-sorted supramolecular polymeric stacks when mixed, in which the emission is quenched due to PET from the electron rich OTs or OPVs to the electron deficient PBIs.[35,36] Recently, it has been reported that weak interfacial charge transfer interactions[49] facilitates the formation of self-sorted supramolecular assemblies of thienylenevinylenes and PBIs that form coaxial fibres.[38] Authors selected a trithienylenevinylene derivative (TTV), **1** as the donor (p-type) and a structurally dissimilar perylene bisimide (PBI), **2** as the acceptor (n-type) (Figure 4.1a and b). In the case of **1**, because of the presence of the amide bond resulted in directional H-bonding and H-type aggregation leading to the formation of 1D self-assembly. On the other hand large π surface-induced stacking in the case of **2** leads to the formation of J-type aggregates. The mixing of the p-type gelator, **1** with the n-type semiconductor, **2** results in the formation of self-sorted fibers, which are coaxially aligned to form interfacial p–n heterojunctions (Figure 4.1c). This coaxially aligned interfacial p-n heterojunctions

affect the photoconductivity of this PBI/TTV mixed assembly. The unidirectional alignment and the coaxial organization of donors and acceptors facilitate charge separation and results in high photoconducticity.

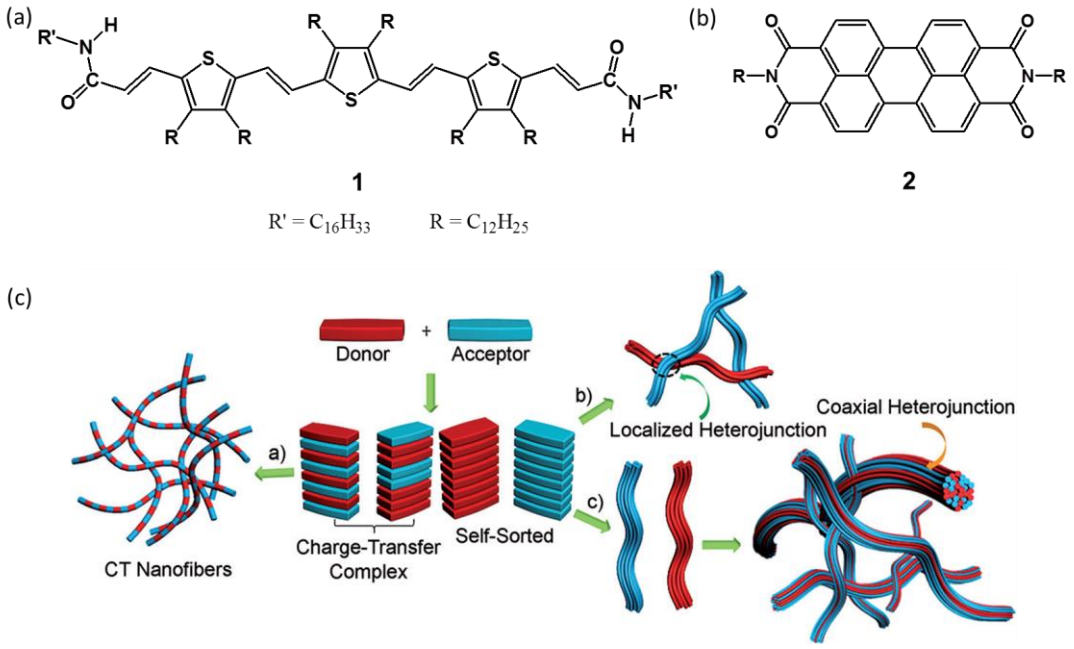

Figure 4.1. Chemical structure of a) TTV (p-type molecule) and b) PBI (n-type molecule). (c) The conceptual representation showing the possible interactions between a p-type donor and an n-type acceptor leading to different possible hierarchical structures. (Adapted with permission from ref. 38 Copyright 2015 WILEY-VCH.)

The importance of interfacial charge transfer interaction is demonstrated using small molecules such as π-extended tetrathiafulvalene (exTTF), **3**, as electron-donor and perylene-bisimide (PBI), **4a** and **4b**, as electron-acceptors, endowed with complementary groups, namely carboxylic acid and guanidinium or quaternary ammonium salts (Figure 4.2).[49b] High value of photoconductivity is observed in this case by the controlled alignment of p/n-materials by the electrostatic co-assembly of complementary self-assembling nanofibers.

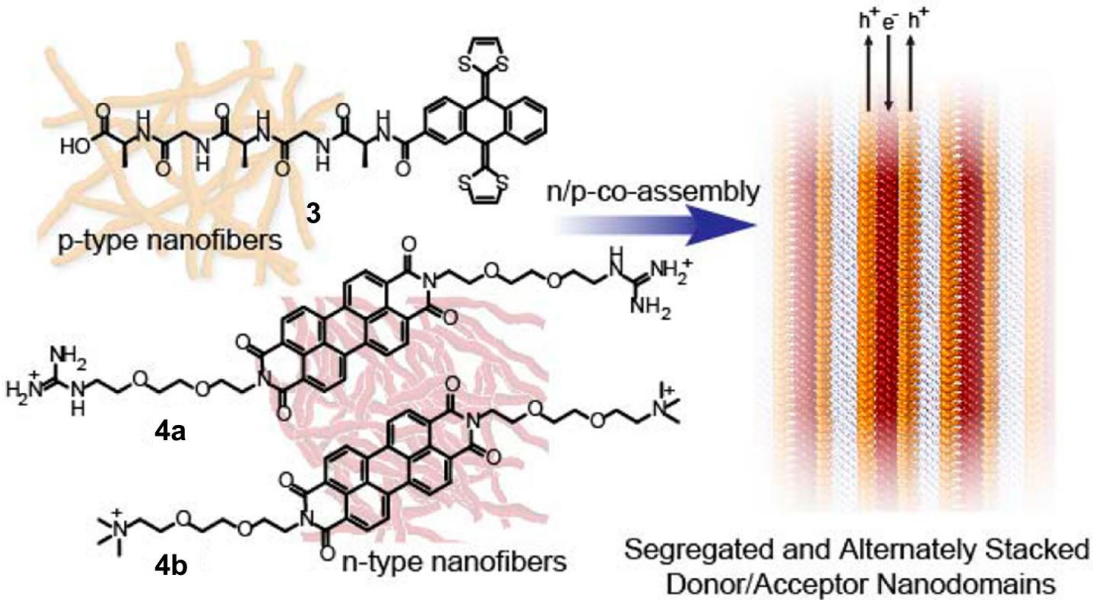

Figure 4.2. (Left) Molecular structures of exTTF derivative **3** and PBI derivatives **4a**,**b**. (Right) Schematic representation of the n/p-material obtained by the coassembly of previously self-assembled molecules. (Adapted with permission from ref. 49b. Copyright 2015 American Chemical Society.)

Based on these findings, we hypothesized that suitably designed C_3-symmetrical systems of OPVs and PBIs may form supramolecular polymers of self-sorted donor and acceptor fibers with quenched fluorescence. In such a case, the weak interfacial donor-acceptor interaction in the supercoiled fibers at supramolecular level can be perturbed by exposure to a strong donor or acceptor molecular vapors, which may results in a "turn-on" fluorescence with distinct color variation. As a proof-of-concept to this hypothesis, we illustrate that a combination of a C_3-symmetrical OPV, ***C*$_3$OPV2** and a C_3-symmetrical PBI, ***C*$_3$PBI**, form supercoiled fibers of self-sorted donor-acceptor stacks, which resulted in a "turn-off/turn-on" fluorescence sensor for the detection of different aromatic VOCs.

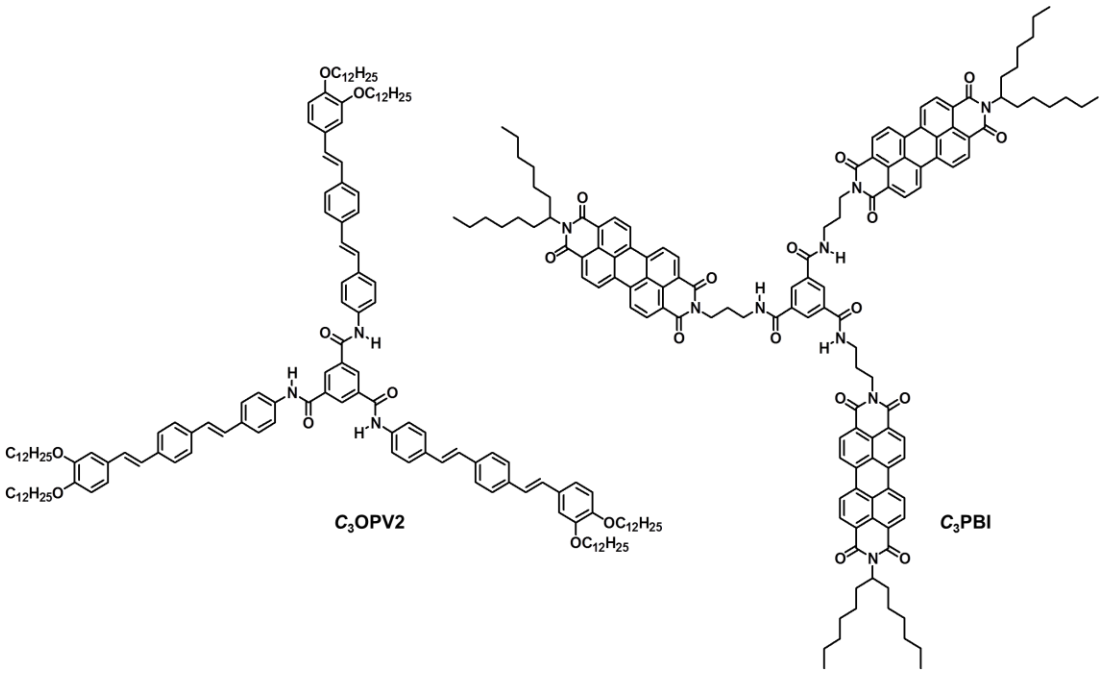

Figure 4.3. Chemical structures of ***C*$_3$OPV2** and ***C*$_3$PBI**.

4.3. Results and Discussion

4.3.1. Synthesis of *C*$_3$OPV2 and *C*$_3$PBI

Synthesis of ***C*$_3$OPV2** is described in Chapter 2 and the synthesis of ***C*$_3$PBI** is reported in Chapter 3b.

4.3.2. Self-assembly of *C*$_3$OPV2 and *C*$_3$PBI

Having these molecules in the pure form, our next objective was to get a clear idea of the mechanistic pathway of the individual assembly of ***C*$_3$OPV2** and ***C*$_3$PBI**. Detailed UV/Vis absorption studies in different solvents revealed that these molecules self-assemble in toluene at a concentration below 10^{-5} M (Figure 4.4). Further understanding of the self-assembly mechanism is achieved by the temperature-dependent absorption studies. For this purpose, in the case of ***C*$_3$OPV2**,

the absorption shoulder band at 425 nm is monitored as a function of temperature with a cooling rate of 1 K min^{-1} (Figure 4.4b and Figure 4.5a).

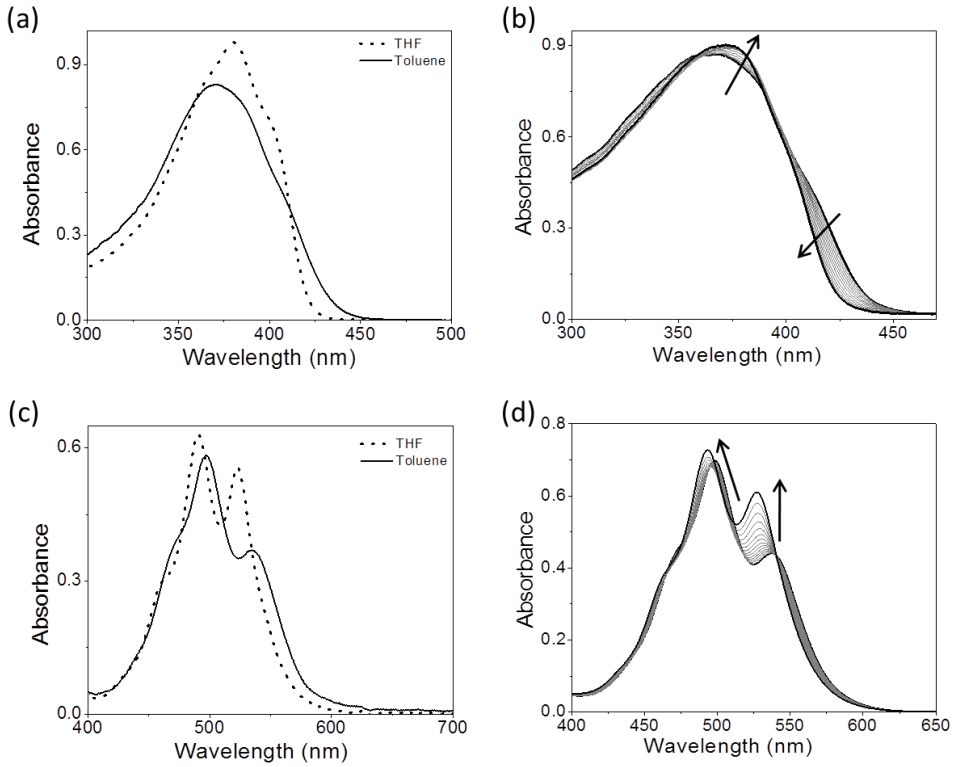

Figure 4.4. UV/Vis absorption spectra of (a) ***C*$_3$OPV2** and (c) ***C*$_3$PBI** in THF and toluene (1×10^{-4} M). Temperature dependent absorption spectra of (b) ***C*$_3$OPV2** and (d) ***C*$_3$PBI**, in toluene (1×10^{-4} M). Arrows indicate relative changes in absorption with increase in temperature from 20 to 90 °C.

No hysteresis was observed when the solution was heated again to the monomeric state, indicating that the thermodynamic self-assembly process is reversible. It is clear from the plot of the fraction of aggregates (α_{agg}) versus temperature that the molecule forms assembly through an isodesmic pathway (equal-K model) as indicated by the broad melting curve, which could be fitted with the standard isodesmic model (Figure 4.5a).[51-53] This observation is quite surprising, especially in the scenario that most of the C_3-symmetrical benzene trisamide derivatives are

known to self-assemble through a co-operative nucleation-elongation mechanism.[54-56] The isodesmic self-assembly of ***C*$_3$OPV2** presumably is governed by π-π stacking of OPV moieties. The contribution from directional intermolecular H-bonding may be weak due to the presence of sterically demanding aromatic core and the six alkyl chains at the periphery.[54-58]

The temperature dependent absorption spectrum of ***C*$_3$OPV2** is fitted with isodesmic or equal-K model in which the binding constant for each addition of monomer to the growing assembly is the same. Standard isodesmic model is used for analyzing the data.[51] The details of the standard Isodesmic model is described in Chapter 2. The thermodynamic parameters are calculated and are summarized in Table 4.1. The melting transition temperature (T_m, temperature at which α_{agg} = 0.50) of the assembly is found as 321.5 K (Figure 4.7a) with an enthalpy value of -85.1 kJmol^{-1} and a binding constant of 4.7×10^4 M^{-1} (Table 4.1).

Absorption spectrum of ***C*$_3$PBI** in toluene is shown in Figure 4.4c. To probe the self-assembly pathway of ***C*$_3$PBI**, the absorption changes at 527 nm is monitored as a function of temperature with a cooling rate of 1 K min^{-1} (Figure 4.4d and Figure 4.5b). The plot of α_{agg} with temperature showed a non-sigmoidal transition characteristic of a co-operative pathway, which could be fitted with the nucleation-elongation model (Figure 4.5b).[53,54,59-65] In order to demonstrate the involvement of nucleation and growth processes in the observed self-assembly of ***C*$_3$PBI**, we have attempted to analyze the curve on the basis of the model proposed by van der Schoot, Schenning and Meijer[54] and is already described in Chapter 3b. By applying this model, the elongation temperature (T_e) is determined as 360.5 K and the

release upon elongation (H_e) is calculated as -27.5 kJ mol^{-1} (Table 4.2). High degree of cooperativity is inferred from the small value of the equilibrium constant for the nucleation step (K_a), which is determined as 10^{-6}.

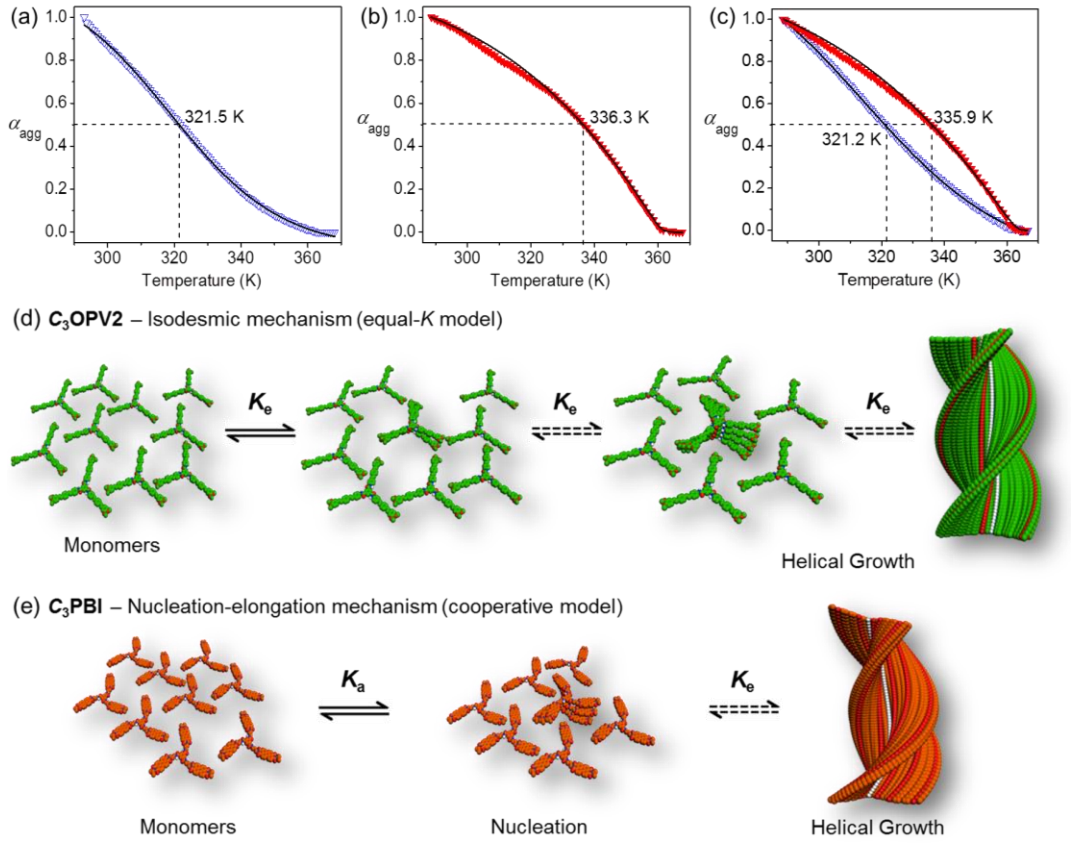

Figure 4.5. Plots of fraction of aggregates (α_{agg}) against temperature for (a) ***C*$_3$OPV2** and (b) ***C*$_3$PBI** individual assemblies and (c) for ***C*$_3$OPV2** and ***C*$_3$PBI** in the 1:1 mixture in toluene (1×10^{-4} M). ***C*$_3$OPV2** (Δ), ***C*$_3$PBI** (▼) and fit (—). Absorbance was monitored at 425 and 527 nm for ***C*$_3$OPV2** and ***C*$_3$PBI**, respectively with a rate of cooling of 1 K min^{-1}. Schematic illustration of the self-assembly pathway of (d) ***C*$_3$OPV2** (e) ***C*$_3$PBI**. K_e is the association constant and K_a is the activation constant expressing the degree of cooperativity.

After having an idea of the individual assembly of ***C*$_3$OPV2** and ***C*$_3$PBI** in toluene, we studied the effect of mixing both molecules at a 1:1 ratio by monitoring the changes in the absorption spectrum under identical experimental conditions used for the individual assemblies. The resultant spectrum is found to be a sum of the

absorption spectrum of the individual constituents (Figure 4.6a). Furthermore, the absence of a CT band in the absorption spectrum excludes the possibility of a molecular level donor-acceptor interaction (Figure 4.6a). As in the case of individual assemblies in toluene, the solution of 1:1 mixture was also cooled down slowly with a rate of 1 K min^{-1} (Figure 4.6b). Variable temperature absorption spectral change of the 1:1 mixture monitored at 425 and 527 nm exhibited the melting of the individual aggregates without much variation from their respective melting transition curves observed in the individual assemblies (Figure 4.5c). Like in the individual assemblies, the transition curves obtained from the plot of α_{agg} versus temperature could be fitted with the isodesmic model and the nucleation-elongation model for ***C*$_3$OPV2** and ***C*$_3$PBI**, respectively (Figure 4.5c).

The thermodynamic parameters calculated for the mixture from the fit are in good agreement with that of the individual assemblies. The melting transition temperature, T_m, of ***C*$_3$OPV2** in the mixture was 321.2 K, which is close to that of the ***C*$_3$OPV2** self-assembly (321.5 K). Similarly, T_m of the ***C*$_3$PBI** assembly in the mixture is 335.9 K and matches to that observed for the individual assembly of the ***C*$_3$PBI** (336.3 K). The other thermodynamic parameters such as enthalpy and entropy changes also match with that of the individual assemblies (Table 4.1 and 4.2). These results imply that both ***C*$_3$OPV2** and ***C*$_3$PBI** form self-sorted stacks when they are mixed.

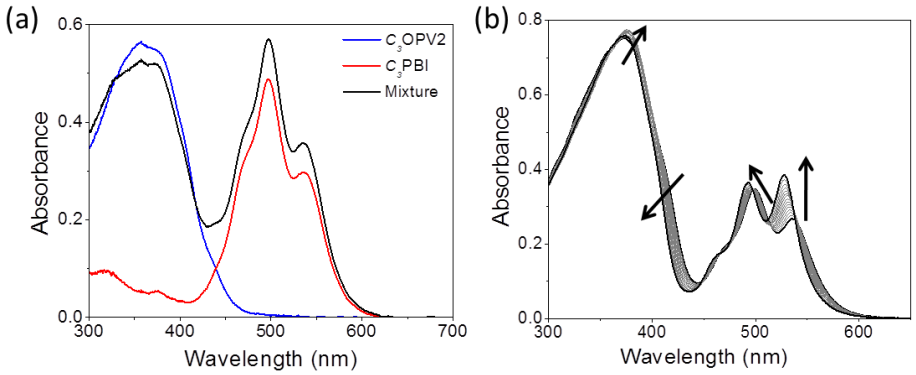

Figure 4.6. (a) Comparison of the absorption spectra of ***C*$_3$OPV2**, ***C*$_3$PBI** and 1:1 mixture and (b) temperature dependent absorption spectra of 1:1 mixture of ***C*$_3$OPV2** and ***C*$_3$PBI** in toluene (1×10^{-4} M).

Other important parameters in support of the formation of self-sorted assembly are the association constant (K_e) in the case of ***C*$_3$OPV2** and the degree of cooperativity (K_a) in the case of ***C*$_3$PBI** (Table 1 and 2). The association constant for the addition of individual monomer to the growing assembly of ***C*$_3$OPV2** in the mixture is 3.7×10^4 M^{-1}, which almost matches with the value for the individual assembly of ***C*$_3$OPV2** (4.7×10^4 M^{-1}). For the cooperative self-assembly of ***C*$_3$PBI**, the degree of cooperativity is in the range of 10^{-6}, similar to that of the individual assembly.

Table 4.1. Thermodynamic parameters calculated for the self-assembly of ***C*$_3$OPV2** using isodesmic model.

***C*$_3$OPV2**	C (mM)	ΔH (kJ mol^{-1})	ΔS (J mol^{-1} K^{-1})	T_m (K)	K_e (10^4 M^{-1})	DP_N
Alone	0.1	-85.1	-194.5	321.5	4.7	2.7
In mixture	0.1	-73.6	-158.0	321.2	3.7	2.5

C the concentration; ΔH the change in enthalpy; ΔS the change in entropy; T_m, the melting transition temperature; K_e, the association constant and DP_N, the degree of polymerization.

Table 4.2. Thermodynamic parameters calculated for the self-assembly of **C_3PBI** using nucleation-elongation model.

C_3PBI	C (mM)	ΔH_e (kJ mol^{-1})	ΔS_e (J mol^{-1} K^{-1})	T_m (K)	T_e (K)	K_a
Alone	0.1	-27.4	-140.9	336.3	360.5	10^{-6}
In mixture	0.1	-27.5	-132.6	335.9	362.4	10^{-6}

C, the concentration; ΔH_e and ΔS_e, respectively are the change in enthalpy and entropy during elongation process; T_m, the melting transition temperature; T_e, the elongation temperature and K_a, the degree of cooperativity.

After understanding the self-assembly mechanism of **C_3OPV2** and **C_3PBI** in the individual assembly as well as in the mixture, we probed their emission properties. In toluene (1×10^{-4} M) at room temperature, **C_3OPV2** emission maximum is red-shifted with quenching which implies the formation of aggregated species (Figure 4.7a), whereas **C_3PBI** showed an enhancement in emission as a result of aggregation (Figure 4.7b).

Atomic force microscopic (AFM) images of **C_3OPV2** drop cast from 1×10^{-4} M toluene solution on a freshly cleaved mica surface revealed the formation of micrometer long helical fibers of diameter 200-250 nm (Figure 4.8a). **C_3PBI** also

displayed the formation of helical fibres with diameter varying from 100-150 nm and length extended to several micrometers (Figure 4.8b).

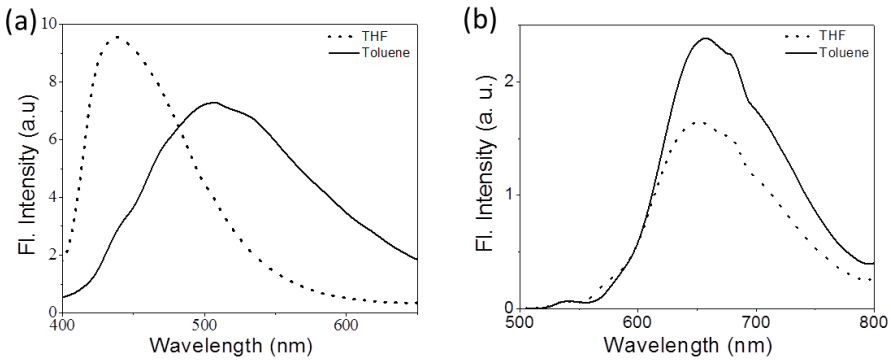

Figure 4.7. Emission spectra of (a) ***C*$_3$OPV2** and (b) ***C*$_3$PBI** in THF and toluene (1×10^{-4} M, *l* = 1 mm λ_{ex} = 375 nm).

For the 1:1 mixed assembly, the fiber-like morphology is retained; however, the formation of super coiled helical ropes with increased diameter (400-500 nm) is observed (Figure 4.8c). The scanning electron microscopy (SEM) images also support the formation of helical fibers and supercoiled ropes (Figure 4.8d-f). These observations are in analogy to the previous reports on the self-assembly of C_3-symmetrical *N*,*N*',*N*''-trialkyl benzene-1,3,5-tricarboxamide in which the amide functionality is involved in a three-fold helical array of intermolecular hydrogen bonding.[66-68] From the mechanistic studies and the morphological features, it is inferred that the self-sorted donor and acceptor fibers are formed initially which enter into weak interfacial charge transfer interaction at the supramolecular level resulting in supercoiled ropes.[38,46]

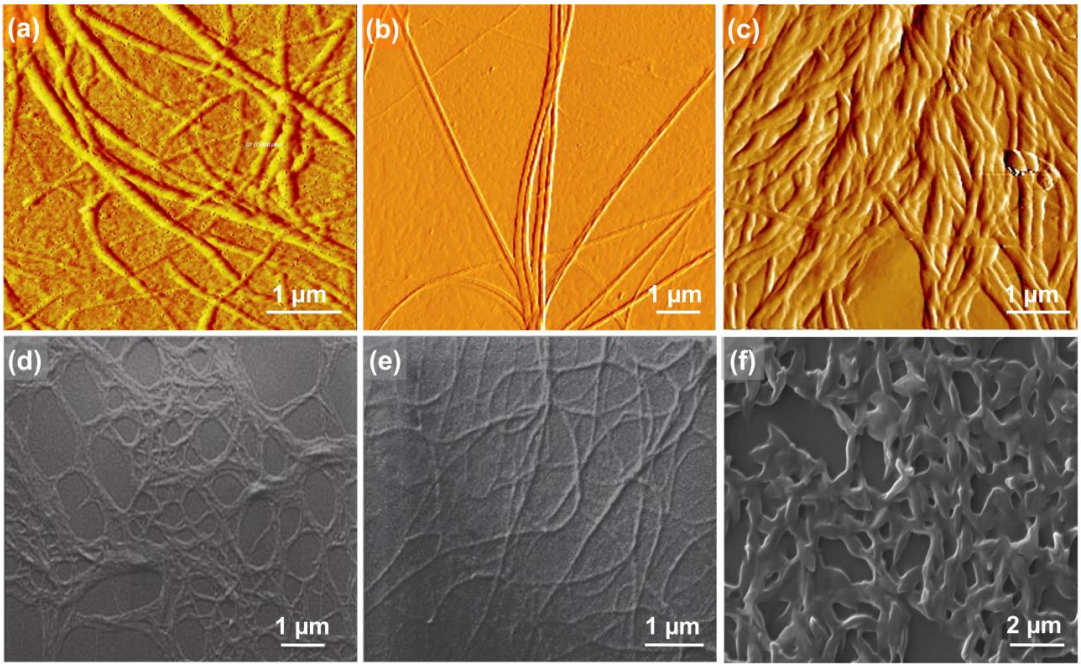

Figure 4.8. AFM (a), (b) (c) and SEM (d), (e), (f) images of ***C*$_3$OPV2**, ***C*$_3$PBI,** 1:1 mixture, respectively.

The absorption spectra of a 1:1 mixture of ***C*$_3$OPV2** and ***C*$_3$PBI** in the solution (toluene, 1×10^{-4} M, Figure 4.6a) and film states (Figure 4.9a) did not show any CT band, indicating the absence of a molecular level donor-acceptor interaction. However, significant quenching of the individual emission of ***C*$_3$OPV2** and ***C*$_3$PBI** was observed in the solution and the film states (Figure 4.10 and Figure 4.9b). These observations could be ascribed to a possible PET from the donor OPV to the acceptor PBI.

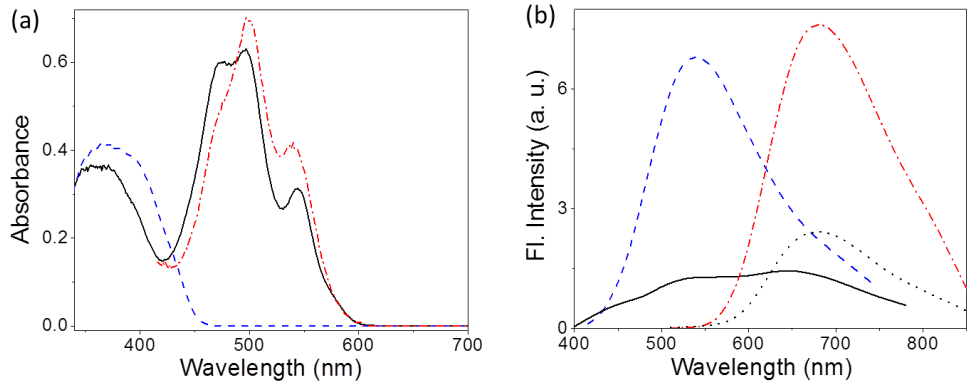

Figure 4.9. (a) Absorption spectra of ***C*$_3$OPV2** (---), ***C*$_3$PBI** (-•-), and 1:1 mixture of ***C*$_3$OPV2** and ***C*$_3$PBI** (—) in the film state. (b) Emission spectra of ***C*$_3$OPV2** (---) λ_{ex} = 375 nm, ***C*$_3$PBI** (-•-) λ_{ex} = 500 nm, and 1:1 mixture of ***C*$_3$OPV2** and ***C*$_3$PBI** (—) λ_{ex} = 375 nm and (····) λ_{ex} = 500 nm in the film state.

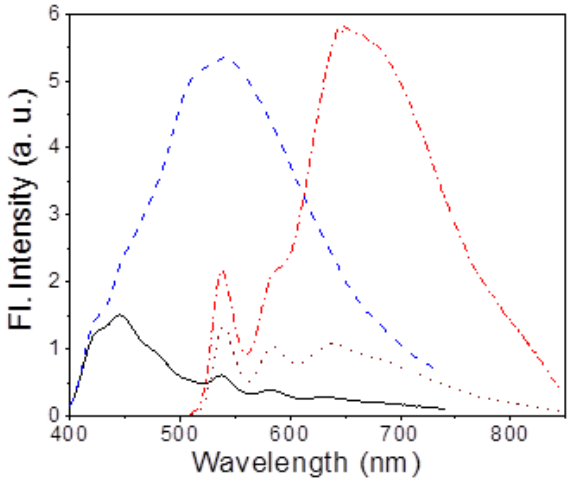

Figure 4.10. Emission spectra of ***C*$_3$OPV2** (---) λ_{ex} = 375 nm, ***C*$_3$PBI** (-•-) λ_{ex} = 500 nm, and 1:1 mixture of ***C*$_3$OPV2** and ***C*$_3$PBI** (—) λ_{ex} = 375 nm and (····) λ_{ex} = 500 nm in toluene (1×10^{-4} M).

The PET process between ***C*$_3$OPV2** and ***C*$_3$PBI** was investigated using femtosecond pump-probe spectroscopy. When a solution containing 1:1 mixture of ***C*$_3$OPV2** and ***C*$_3$PBI** was excited at 380 nm where mainly ***C*$_3$OPV2** absorbs, transient absorption spectra showed the formation of radical anion of

***C*$_3$PBI** absorbing broadly around 630 nm with decay time of around 728 ps (Figure 4.11a), which indicates PET from the OPV to the PBI.[69]

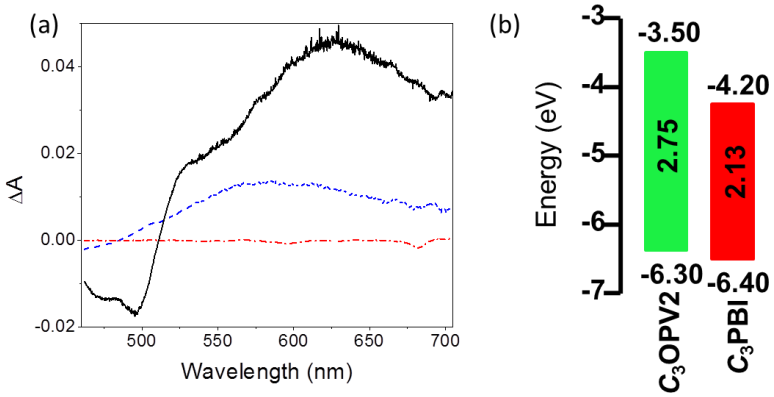

Figure 4.11. (a) Transient absorption spectra of ***C*$_3$OPV2** (---), ***C*$_3$PBI** (-•-) and 1:1 mixture (—) in toluene (1×10^{-4} M) recorded at 1.9 ps, λ_{ex} = 380 nm. (b) The energy level diagram for ***C*$_3$OPV2** and ***C*$_3$PBI**.

The feasibility of PET between these molecules is further established by photoelectron yield spectroscopic studies (Figure 4.12). From the value of HOMO and the optical band gap (E_g) obtained from the film state absorption spectrum (Figure 4.12), LUMO of both ***C*$_3$OPV2** and ***C*$_3$PBI** were calculated.

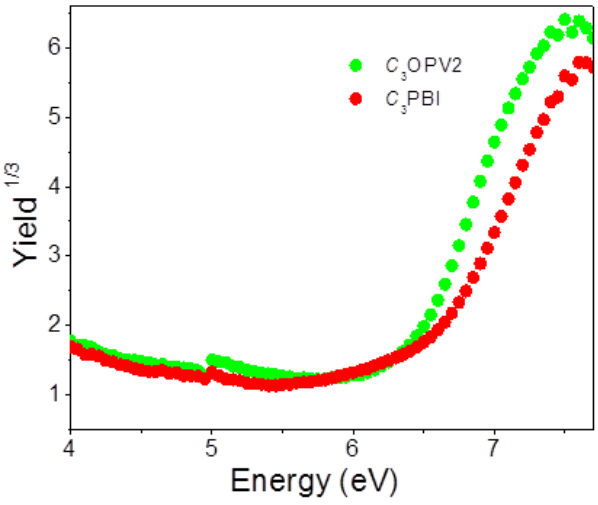

Figure 4.12. Photoelectron yield spectra in air for ***C*$_3$OPV2** and ***C*$_3$PBI** films over an ITO coated glass plates drop cast from toluene solutions of concentration 1×10^{-4} M.

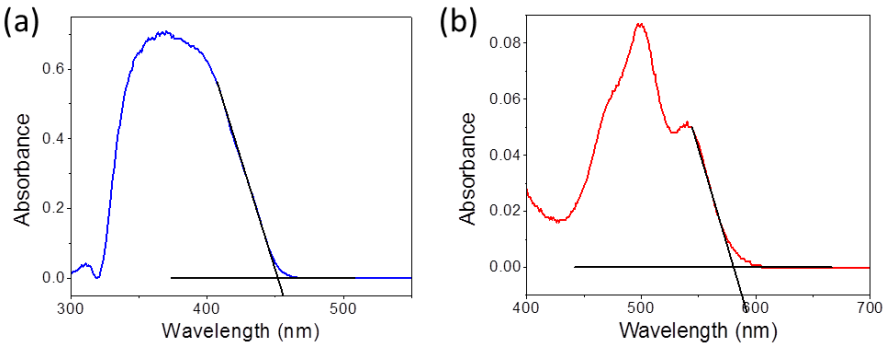

Figure 4.13. Absorption spectra of (a) ***C*$_3$OPV2** and (b) ***C*$_3$PBI** in the film state. The tangents are drawn in order to get the onset value (λ_{onset} for ***C*$_3$OPV2** = 452 nm, λ_{onset} for ***C*$_3$PBI** = 581 nm).

***C*$_3$PBI** showed a slightly deeper LUMO (-4.20 eV) when compared to that of ***C*$_3$OPV2** (-3.50 eV) (Figure 4.13b). Since ***C*$_3$PBI** is an electron accepting molecule when compared to ***C*$_3$OPV2**, the HOMO level of the former is lower than that of ***C*$_3$OPV2** (Figure 4.11b). Therefore, upon photoexcitation, electrons are transferred from ***C*$_3$OPV2** to ***C*$_3$PBI** leading to the quenching of the emission.

4.3.3. Sensing of Volatile Organic Compounds

Since OPVs are known to interact with electron deficient aromatic nitro compounds[12,25] and PBIs with electron rich aromatic amines,[15-17,70-71] we thought that the quenched emission of the supercoiled ***C*$_3$OPV2** and ***C*$_3$PBI** fibres could be "turned on" when comes in contact with a better donor or an acceptor molecule. In order to prove this hypothesis, a toluene solution of a 1:1 mixture of ***C*$_3$OPV2** and ***C*$_3$PBI** (20 µL of 10^{-3} M) was drop cast on glass substrates and exposed to various analytes. The film that was exposed to

aromatic amines such as *o*-toluidine displayed a greenish-yellow emission (Figure 4.14a and 4.14c).

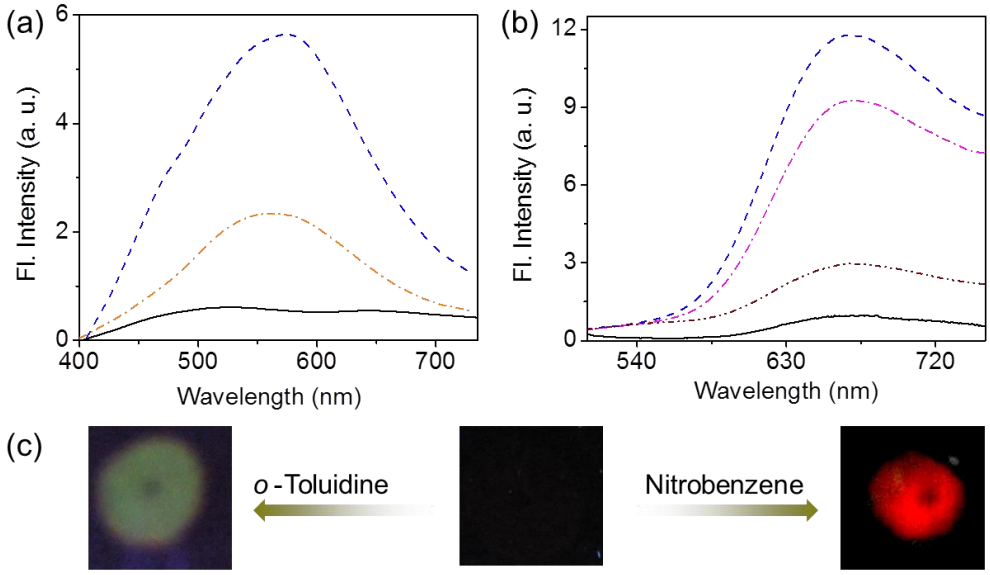

Figure 4.14 The emission spectra of a 1:1 mixture of ***C*$_3$OPV2** and ***C*$_3$PBI** films before and after exposing to vapours of different (a) aromatic amines [(---) o-toluidine, (-•-) aniline and (– –) blank)] λ_{ex} = 375 nm and (b) nitroaromatics [(---) nitrobenzene, (-•-) 2-nitrotoluene, (-••-) 2,4-dinitrotoluene and (—) blank] λ_{ex} = 500 nm. (c) Photographs showing the fluorescence of the 1:1 mixture of ***C*$_3$OPV2** and ***C*$_3$PBI** films before and after exposure to different volatile aromatic compounds.

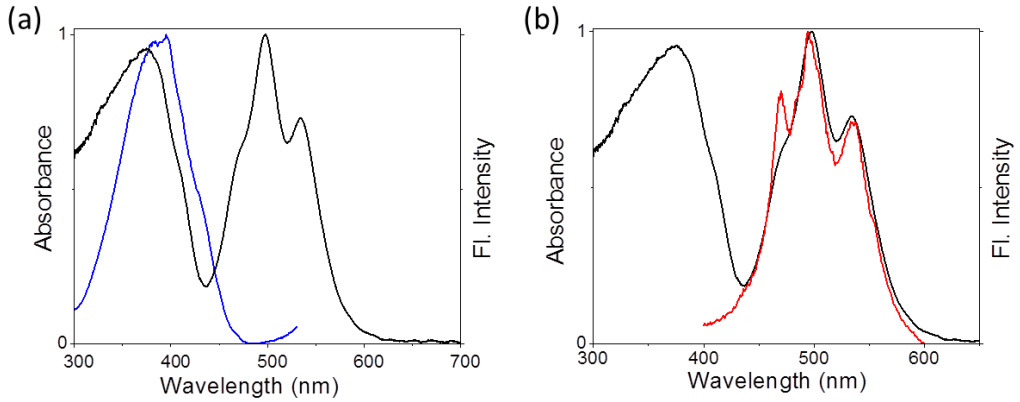

Figure 4.15. Comparison of (a) absorption spectrum of ***C*$_3$OPV2** (—) and the excitation spectrum (—) of 1:1 mixture of ***C*$_3$OPV2** and ***C*$_3$PBI** and (b) absorption

spectrum of C_3PBI (—) in toluene and the excitation spectrum (—) of 1:1 mixture of ***C*$_3$OPV2** and ***C*$_3$PBI** (emission monitored at 540 nm for ***C*$_3$OPV2** and 650 nm for ***C*$_3$PBI**).

Comparison of the absorption spectrum of ***C*$_3$OPV2** and the excitation spectrum obtained upon monitoring the emission at 540 nm in the 1:1 mixture of ***C*$_3$OPV2** and ***C*$_3$PBI** revealed that the emission originates from ***C*$_3$OPV2** molecule in the mixture (Figure 4.15a). On the other hand, a red emission was obtained when the film was exposed to nitrobenzene vapors (Figure 4.14b and 4.14c). Excitation spectrum of the 1:1 mixture when monitored at 650 nm showed a resemblance to the absorption spectrum of ***C*$_3$PBI** individual assembly (Figure 4.15b), which proves that the red emission is from the self-assembled ***C*$_3$PBI** molecule. Similar experiments were conducted for other aromatic amines such as 2-aminophenol, aniline, *m*-toluidine, etc. and nitroaromatics such as TNT, dinitrotoluene (DNT), *o*-nitrotoluene, etc. and the results are summarized in Figure 4.16.

The observed "turn-on" emission of the mixed 1:1 ***C*$_3$OPV2** and ***C*$_3$PBI** films in presence of analytes is explained as follows. Electron rich aromatic amines facilitate strong CT interaction with the electron deficient ***C*$_3$PBI** fibers, which in turn prevent the weak interfacial PET from the ***C*$_3$OPV2** fibers to ***C*$_3$PBI** fibers, thus activating the ***C*$_3$OPV2** emission upon excitation at 375 nm. Emission intensity revival monitored at 550 nm with time is found to depend upon the electron donating ability of the amines used (Figure 4.17a). For the first 120 seconds of exposure, around 5-fold increase in the

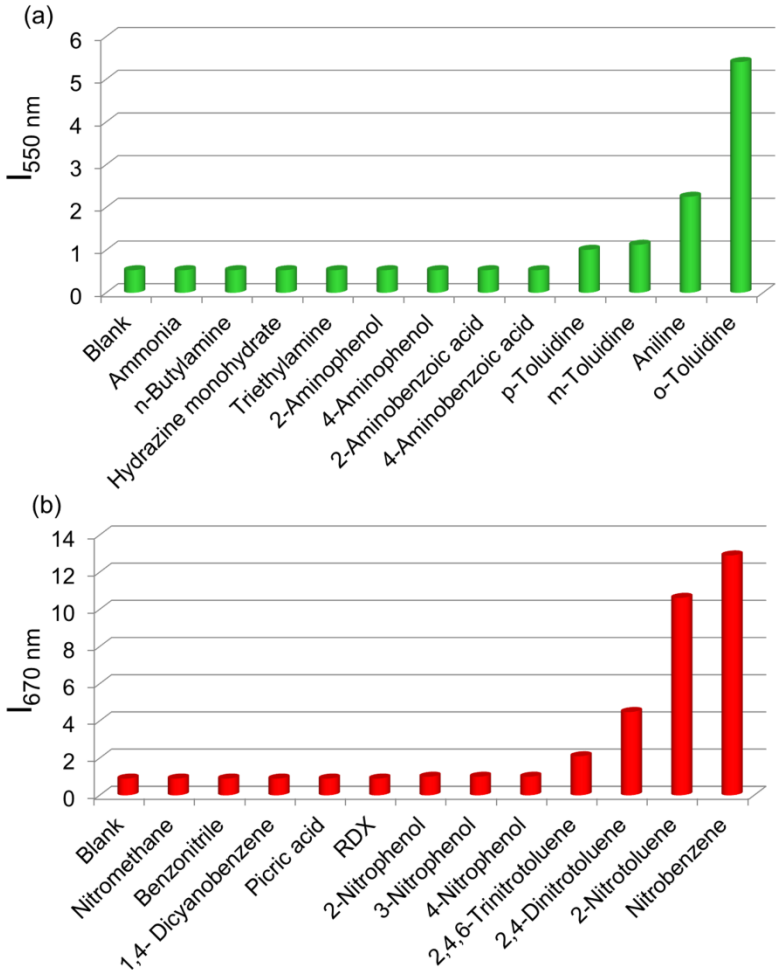

Figure 4.16. The selectivity plot for the vapor phase detection of different volatile (a) amines and (b) nitro compounds using a film prepared from 1:1 mixture of ***C*$_3$OPV2** and ***C*$_3$PBI**.

emission intensity for *o*-toluidine is observed, while only a 2-fold increase is noticed for aniline. The inductive effect of the electron donating methyl group in *o*-toluidine makes it a better donor than aniline. The inductive effect decreases in the case of *m*-toluidine as the methyl group is far from the amino group. Not only the electron donating ability of different amines but also the vapor pressure of the different amines plays an important role to the selective detection of *o*-toluidine. The vapor pressure of *o*-toluidine at 25 °C is around

200 Pa and those of aniline and *m*-toluidine are around 89 and 17 Pa, respectively. This high value of vapor pressure for *o*-toluidine and the electron donating positive inductive effect of methyl group make it fast responsive upon interaction with the film of the mixed assembly.

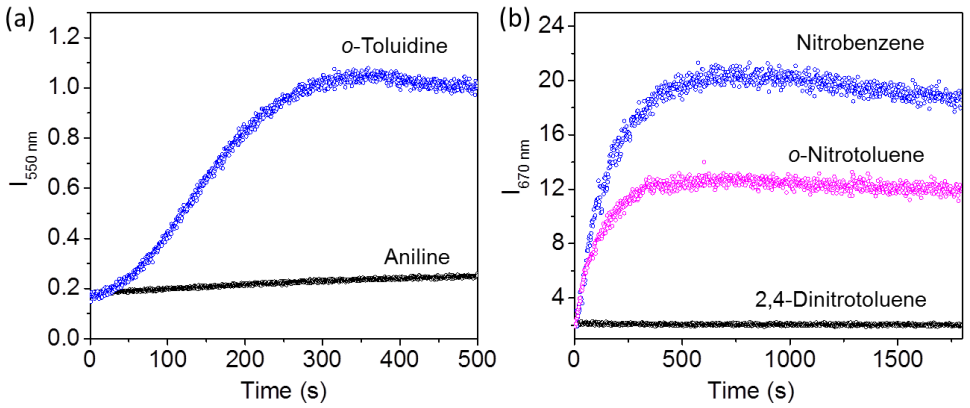

Figure 4.17. (a) Plots of emission intensity at 550 nm (λ_{ex} = 375 nm) and (b) at 670 nm (λ_{ex} = 500 nm) as a function of time after exposing a film prepared from 1:1 mixture of ***C*$_3$OPV2** and ***C*$_3$PBI** to the vapors of aromatic amines and nitroaromatics, respectively.

When vapors of nitroaromatic compounds such as nitrobenzene and nitrotoluene are exposed to the supercoiled fibers of ***C*$_3$OPV2** and ***C*$_3$PBI**, a red emission was observed. Electron deficient nitroaromatics can have strong CT interaction with electron rich ***C*$_3$OPV2** fibres thereby inhibiting the weak interfacial PET from ***C*$_3$OPV2** fibers to ***C*$_3$PBI** fibers upon excitation of the latter at 500 nm. Hence the interaction between the ***C*$_3$OPV2** and ***C*$_3$PBI** stacks becomes weaker, thereby activating the ***C*$_3$PBI** emission by favoring more energetically feasible PET from ***C*$_3$OPV2** to the electron accepting nitroaromatic compounds. In this case also, the sensitivity depends upon both the electron accepting ability and the vapour pressure of the nitro compounds. This is evident from the plot of the emission intensity monitored at 670 nm

with time of exposure (Figure 4.17b). It is observed that for the first one minute of exposure, nitrobenzene and 2-nitrotoluene showed almost equal amount of emission recovery. However, upon extended exposure, nitrobenzene gave more emission revival than the nitrotoluene because of its high vapor pressure (20 Pa) and electron accepting ability. When compared to nitrobenzene, the presence of electron donating methyl group reduces the electron accepting ability of *o*-nitrotoluene. At the same time, molecules such as DNT and TNT, which are more electron deficient than nitrobenzene showed less response with the film. This observation is explained on the basis of the difference in vapour pressure of these nitroaromatics. The vapor pressure of TNT and DNT are 0.0165 and 0.0079 Pa, respectively, which is much less than the vapor pressure of nitrobenzene (20 Pa) and 2-nitrotoluene (38 Pa).

The overall processes in the sensing of VOCs by the supercoiled self-stack of ***C*$_3$OPV2** and ***C*$_3$PBI** are schematically shown in Figure 4.18. *C*$_3$-symmetrical OPV and PBI prefer to form columnar helical assemblies of self-sorted stacks. The ***C*$_3$OPV2** stacks (green) and the ***C*$_3$PBI** stacks (red), due to weak interfacial CT interaction, bundles to form supercoiled fibers (black) in which the fluorescence is quenched by PET between the donor-acceptor self-sorted fibres. The PET process is subsequently perturbed by exposing the fibers to strong donor or acceptor molecules, resulting in respective fluorescence signals of the ***C*$_3$OPV2** or ***C*$_3$PBI**.

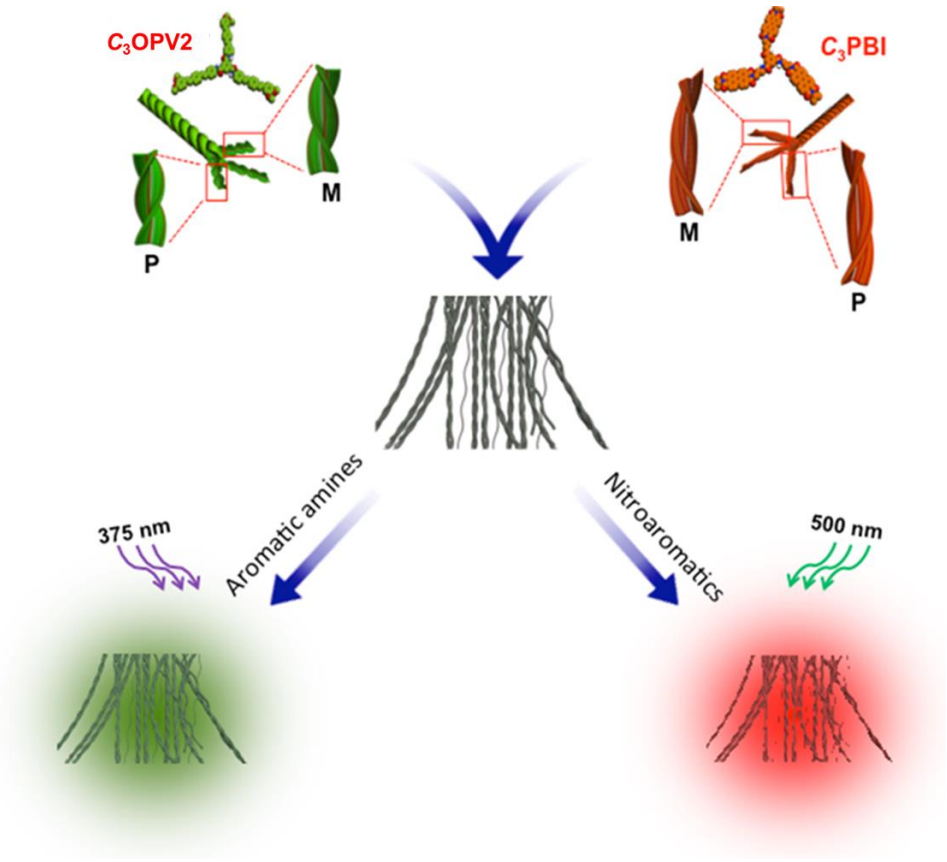

Figure 4.18. Schematic illustration of fluorescence 'turn-off/turn-on' mechanism of the self-sorted fibers of 1:1 mixture of ***C*$_3$OPV2** and ***C*$_3$PBI** on exposing to different VOCs.

4.4. Conclusions

By taking advantage of self-sorting at molecular level and electronic interaction at macroscopic level, we could design nonfluorescent supercoiled fibers of ***C*$_3$OPV2** and ***C*$_3$PBI** molecules. The self-sorting is facilitated by the difference in the self-assembly pathway of the individual molecules wherein ***C*$_3$OPV2** followed an isodesmic model and ***C*$_3$PBI** preferred a cooperative mechanism. Interfacial PET between the self-sorted fibers resulted in the quenching of the initial fluorescence of the molecules, which could be perturbed by exposure to VOCs, especially electron rich compounds such as

aromatic amines and electron deficient compounds such as nitroaromatics. Thus, the green emission of ***C*$_3$OPV2** appeared when exposed to *o*-toluidine and the red emission of ***C*$_3$PBI** by exposing the film to nitroaromatic vapours. Extend of emission revival depends on the electron donating ability of aromatic amines and the electron withdrawing ability of nitro aromatics in addition to the vapour pressure of the molecules. The fluorescence "turn-off-turn-on" features of the supercoiled supramolecular fibers of the self-sorted donor-acceptor system described here has the ability to detect *o*-toluidine of metabolic origin which is a known lung cancer marker.

4.5. Materials and Methods

4.5.1. General

Unless otherwise stated, all starting materials and reagents were purchased from commercial suppliers and used without further purification. Solvents were purified and dried by standard methods prior to use. Reactions were monitored using thin layer chromatography (TLC) on silica gel 60 F_{254} (0.2 mm; Merck). Visualization was accomplished using UV lamp (365 nm). Column chromatography was performed on glass columns of different sizes hand packed with silica gel 60 (particle size 0.040–0.063 mm, Merck). Molecules ***C*$_3$OPV2** and ***C*$_3$PBI** were synthesized according to Scheme S1 and S2 based on standard protocols.

4.5.2. Instrumentation

NMR spectra were measured on a 300 or 500 MHz Bruker Avance DPX spectrometer. Chemical shifts are reported in parts per million (ppm) using

tetramethylsilane (TMS) (δ_H = 0 ppm) as an internal reference. The resonance multiplicity is described as s (singlet), d (doublet), t (triplet) and m (multiplet). FT-IR spectra were recorded on a Shimadzu IRPrestige-21 Fourier Transform Infrared Spectrophotometer using KBr pellet method. Mass spectra (MS) were recorded on a JEOLJSM 600 fast atom bombardment (FAB) high-resolution mass spectrometer. Matrix-assisted laser desorption ionization time-of-flight (MALDI-TOF) mass spectra were obtained on a Shimadzu AXIMA-CFR PLUS spectrometer using α-cyano-4-hydroxycinnamic acid as the matrix. The electronic absorption spectra were recorded on a Shimadzu UV-3101 UV-Vis-NIR scanning spectrophotometer. The fluorescence spectra were recorded on a SPEX-Fluorolog F112X spectrofluorimeter. AFM imaging was carried out under ambient conditions using a NTEGRA (NT-MDT) operating with a tapping mode regime. Micro-fabricated TiN cantilever tips (NSG10) with a resonance frequency of 299 kHz and a spring constant of S8 20-80 Nm^{-1} was used. Samples for the imaging were prepared by drop casting toluene solution (1×10^{-4} M) of the molecules on freshly cleaved mica surface after drying in vacuum. SEM images were taken on a Zeiss EVO 18 cryo SEM Special Edn with variable pressure detector working at 20–30 kV after sputtering with gold. Samples were prepared by drop casting the aggregates of ***C*$_3$OPV2**, ***C*$_3$PBI** and 1:1 mixture of both in toluene on freshly cleaved mica substrate. It was kept for overnight to allow slow evaporation of the solvent and then further dried in a vacuum desiccator for 12 h. In order to carry out the sensing studies in vapor phase, the self-assembled solution were drop cast over glass plates and dried under vacuum. The film was placed in a chamber containing saturated vapor of the analytes. Emission spectra

were collected in a front face geometry using a film sample holder. The samples for photoelectron yield spectroscopy (PYS) were prepared on ITO coated glass plates by solution drop casting (chlorobenzene solution). Prior to the measurements, substrates were dried in a vacuum oven for 2 h at 50 °C. The PYS experiments were done on a RIKEN Keiki Co., Ltd., model AC-3 under high vacuum (1×10^{-3} M pa). The instrument was calibrated using standard aluminium substrate.

4.6. References

1. Buszewski, B.; Kesy, M.; Ligor, T.; Amann, A. *Biomed. Chromatogr.* **2007**, *21*, 553–566.

2. Boots, A.W.; van Berkel, J. J.; Dallinga, J.W.; Smolinska, A.; Wouters, E. F.; van Schooten, F. J. *J. Breath Res.* **2012**, *6*, 027108.

3. Hakim, M.; Broza, Y. Y.; Barash, O.; Peled, N.; Phillips, M.; Amann, A.; Haick, H. *Chem. Rev.* **2012**, *112*, 5949–5966.

4. Broza, Y. Y.; Haick, H. *Nanomedicine* **2013**, *8*, 785–806.

5. Konvalina, G.; Haick, H. *Acc. Chem. Res.* **2014**, *47*, 66–76.

6. Riedel, K.; Scherer, G.; Engl, J.; Hagedorn, H.-W.; Tricker, A. R. *J. Anal. Toxicol.* **2006**, *30*, 187–195.

7. Preti, G.; Labows, J. N.; Kostelc, J. G.; Aldinger, S.; Daniele, R. *J. Chromatogr. B: Biomed. Sci. Appl.* **1988**, *432*, 1–11.

8. Swager, T. M.; Wosnick, J. H. *MRS Bulletin* **2002**, *27*, 446–450.

9. Toal, S. J.; Trogler, W. C. *J. Mater. Chem.* **2006**, *16*, 2871–2883.

10. Sakakibara, K.; Hill, J. P.; Ariga, K. *Small*, **2011**, *7*, 1288–1308.

11. Hu, Z.; Deibert, B. J.; Li, J. *Chem. Soc. Rev.* **2014**, *43*, 5815–5840.

12. Kartha, K. K.; Sandeep, A.; Praveen, V. K.; Ajayaghosh, A. *Chem. Rec.* **2015**, *15*, 252–265.

13. Shanmugaraju, S.; Mukherjee, P. S. *Chem. −Eur. J.* **2015**, *21*, 6656–6666.

14. Nanoarchitectonics deal with interaction and organization of nanoscale nanoscale structures that cause emergence of new functionality, for details see: (a) Ishihara, S.; Labuta, J.; Van Rossom, W.; Ishikawa, D.; Minami, K.; Hill, J. P.; Ariga, K. *Phys. Chem. Chem. Phys.* **2014**, *16*, 9713–9746; (b) Ariga, K.; Ji, Q.; Nakanishi, W.; Hill, J. P.; Aono, M. *Mater. Horiz.* **2015**, *2*, 406–413; (c) Aono, M.; Ariga, K. *Adv. Mater*. **2016**, *28*, 989–992; (d) Ariga, K.; Li, J.; Fei, J.; Ji, Q.; Hill, J. P. *Adv. Mater*. **2016**, *28*, 1251–1286.

15. Che, Y.; Yang, X.; Loser, S.; Zang, L. *Nano Lett.* **2008**, *8*, 2219– 2223.

16. Liu, Y.; Wang, K.-R.; Guo, D.-S.; Jiang, B.-P. *Adv. Funct. Mater.* **2009**, *19*, 2230–2235.

17. Peng, H.; Ding, L.; Liu, T.; Chen, X.; Li, L.; Yin, S.; Fang, Y. *Chem. –Asian J.* **2012**, *7*, 1576–1582.

18. Kumpf, J.; Freudenberg, J.; Schwaebel, S. T.; Bunz, U. H. F. M*acromolecules* **2014**, *47*, 2569–2573.

19. Rochat, S.; Swager, T. M. *Angew. Chem., Int. Ed.* **2014**, *53*, 9792–9796.

20. Mallick, A.; Garai, B.; Addicoat, M. A.; Petkov, P. S.; Heine, T.; Banerjee, R. *Chem. Sci*. **2015**, *6*, 1420–1425.

21. Rose, A.; Zhu, Z.; Madigan, C. F.; Swager, T. M.; Bulović, V. *Nature* **2005**, *434*, 876–879.

22. Che, Y.; Gross, D. E.; Huang, H.; Yang, D.; Yang, X.; Discekici, E.; Xue, Z.; Zhao, H.; Moore, J. S.; Zang, L. *J. Am. Chem. Soc.* **2012**, *134*, 4978–4982.

23. Zhu, W.; Li, W.; Wang, C.; Cui, J.; Yang, H.; Jiang, Y.; Li, G. *Chem. Sci.* **2013**, *4*, 3583–3590.

24. Kartha, K. K.; Sandeep, A.; Nair, V. C.; Takeuchi, M.; Ajayaghosh, A. *Phys. Chem. Chem. Phys.* **2014**, ***16***, 18896–18901.

25. Kartha, K. K.; Babu, S. S.; Srinivasan, S.; Ajayaghosh, A. *J. Am. Chem. Soc.* **2012**, *134*, 4834−4841.

26. Bhalla, V.; Arora, H.; Singh, H.; Kumar, M. *Dalton Trans.* **2013**, *42*, 969–997.

27. Hong, G.; Sun, J.; Qian, C.; Xue, P.; Gong, P.; Zhang, Z.; Lu, R. *J. Mater. Chem. C* **2015**, *3*, 2371–2379.

28. Safont-Sempere, M. M.; Fernández, G.; Würthner, F. *Chem. Rev.* **2011**, *111*, 5784–5814.

29. Osowska, K.; Miljanić, O. *Synlett* **2011**, *12*, 1643–1648.

30. Rest, C.; Mayoral, M.; Fernández, G. *Int. J. Mol. Sci.* **2013**, *14*, 1541–1565.

31. Moffat, J. R.; Smith, D. K. *Chem. Commun.* **2009**, 316–318.

32. Pal, A.; Besenius, P.; Sijbesma, R. P. *J. Am. Chem. Soc.* **2011**, *133*, 12987–12989.

33. Morris, K. L.; Chen, L.; Raeburn, J.; Sellick, O. R.; Cotanda, P.; Paul, A.; Griffiths, P. C.; King, S. M.; Reilly, R. K. O. R.; Serpell, L. C.; Adams, D. J. *Nat. Commun.* **2013**, *4*, 1480.

34. Sato, K.; Itoh, Y.; Aida, T. *Chem. Sci.* **2014**, *5*, 136–140.

35. van Herrikhuyzen, J.; Syamakumari, A.; Schenning, A. P. H. J.; Meijer, E. W. *J. Am. Chem. Soc.* **2004**, *126*, 10021–10027.

36. Sugiyasu, K.; Kawano, S.; Fujita, N.; Shinkai, S. *Chem. Mater.* **2008**, *20*, 2863–2865.

37. Das, A.; Ghosh, S. *Chem. Commun.* **2011**, *47*, 8922–8924.

38. Prasanthkumar, S.; Ghosh, S.; Nair, V. C.; Saeki, A.; Seki, S.; Ajayaghosh, A. *Angew. Chem., Int. Ed.* **2015**, *54*, 946–950.

39. Narayan, B.; Bejagam, K. K.; Balasubramanian, S.; George, S. J. *Angew. Chem., Int. Ed.* **2015**, *54*, 13245–13249.

40. Che, Y.; Zang, L. *Chem. Commun*. **2009**, 5106–5108

41. Jiang, B.-P.; Guo, D.-S.; Liu, Y. *J. Org. Chem.* **2010**, *75*, 7258–7264.

42. Jiang, B.-P.; Guo, D.-S.; Liu. Y. *J. Org. Chem*. **2011**, *76*, 6101–6107.

43. Kumar, M.; Venkata Rao, K.; George, S. J. *Phys. Chem. Chem. Phys.* **2014**, *16*, 1300–1313.

44. Das, A.; Ghosh, S. *Angew. Chem., Int. Ed.* **2014**, *53*, 2038–2054.

45. Aida, T.; Meijer, E. W.; Stupp, S. I. *Science* **2012**, *335*, 813–817.

46. Maggini, L.; Bonifazi, D. *Chem. Soc. Rev.* **2012**, *41*, 211–241.

47. Kulkarni, C.; Balasubramanian, S.; George, S. J. *ChemPhysChem* **2013**, *14*, 661–673.

48. Mukhopadhyay, R. D.; Ajayaghosh, A. *Science* **2015**, *349*, 241–242.

49. For interfacial charge transfer in co-assembly, see: (*a*) Zang, L. *Acc. Chem. Res.* **2015**, *48*, 2705–2714; (*b*) López-Andarias, J.; Rodriguez, M. J.; Atienza, C.; López, J. L.; Mikie, T.; Casado, S.; Seki, S.; Carrascosa, J. L.; Martín, N. *J. Am. Chem. Soc.* **2015**, *137*, 893–897.

50. Xiao, T.; Feng, X.; Wang, Q.; Lin, C.; Wang, L.; Pan, Y. *Chem. Commun.* **2013**, *49*, 8329–8331.

51. Chen, Z.; Lohr, A.; Saha-Möller, C. R.; Würthner, F. *Chem. Soc. Rev.* **2009**, *38*, 564–584.

52. de Greef, T. F. A.; Smulders, M. M. J.; Wolffs, M.; Schenning, A. P. H. J.; Sijbesma, R. P.; Meijer, E. W. *Chem. Rev.* **2009**, *109*, 5687–5754.

53. Smulders, M. M. J.; Nieuwenhuizen, M. M. L.; de Greef, T. F. A.; van der Schoot, P.; Schenning, A. P. H. J.; Meijer, E. W. *Chem. –Eur. J.* **2010**, *16*, 362–367.

54. Smulders, M. M. J.; Schenning, A. P. H. J.; Meijer, E. W. *J. Am. Chem. Soc.* **2008**, *130*, 606–611.

55. Cantekin, S.; de Greef, T. F. A.; Palmans, A. R. A. *Chem. Soc. Rev.* **2012**, *41*, 6125–6137.

56. Narayan, B.; Kulkarni, C.; George, S. J. *J. Mater. Chem. C* **2013**, *1*, 626–629.

57. van Herrikhuyzen, J.; Jonkheijm, P.; Schenning, A. P. H. J.; Meijer, E. W. *Org. Biomol. Chem.* **2006**, *4*, 1539–1545.

58. Filot, I. A. W.; Palmans, A. R. A.; Hilbers, P. A. J.; van Santen, R. A.; Pidko, E. A.; de Greef, T. F. A. *J. Phys. Chem. B* **2010**, *114*, 13667–13674.

59. Korevaar, P. A.; de Greef, T. F. A.; Meijer, E. W.; *Chem. Mater*. **2014**, *26*, 576−586.

60. Rest, C.; Kandanelli, R.; Fernández, G. *Chem. Soc. Rev.* **2015**, *44*, 2543–2572.

61. García, F.; Sánchez, L. *J. Am. Chem. Soc.* **2012**, *134*, 734–742.

62. Mayerhöffer, U.; Würthner, F. *Chem. Sci.* **2012**, *3*, 1215–1220.

63. Malicka, J. M.; Sandeep, A.; Monti, F.; Bandini, E.; Gazzano, M.; Ranjith, C.; Praveen, V. K.; Ajayaghosh, A.; Armaroli, N. *Chem. –Eur. J.* **2013**, *19*, 12991–13001.

64. Kulkarni, C.; Bejagam, K. K.; Senanayak, S. P.; Narayan, K. S.; Balasubramanian, S.; George, S. J. *J. Am. Chem. Soc.* **2015**, *137*, 3924–3932.

65. Nucleation-elongation model is proposed for PBI dyes linked to *tris*(dodecyloxy)benzamide with ethyl, propyl and pentyl spacer groups. This study demonstrates the importance of alkyl spacer length on determining self-assembly pathways of H-bonded PBI dyes. For details, see: (*a*) Ogi, S.; Stepanenko, V.; Sugiyasu, K.; Takeuchi, M.; Würthner, F. *J. Am. Chem. Soc.* **2015**, *137*, 3300–3307; (*b*) Ogi, S.; Stepanenko, V.; Thein, J.; Würthner, F. *J. Am. Chem. Soc.* **2016**, *138*, 670–678.

66. Lightfoot, M. P.; Mair, F. S.; Pritchard, R. G.; Warren, J. E. C*hem. Commun.* **1999**, 1945–1946.

67. Yasuda, Y.; Iishi, E.; Inada, H.; Shirota, Y. *Chem. Lett*. **1996**, 575–576.

68. Stals, P. J. M.; Everts, J. C.; de Bruijn, R.; Filot, I. A. W.; Smulders, M. M. J.; Martín-Rapún, R.; Pidko, E. A.; de Greef, T. F. A.; Palmans, A. R. A.; Meijer, E. W. *Chem. –Eur. J.* **2010**, *16,* 810–821.

69. Rybtchinski, B.; Sinks, L. E.; Wasielewski, M. R. *J. Phys. Chem. A* **2004**, *108,* 7497–7505.

70. Che, Y.; Zang, L. *Chem. Commun.* **2009**, 5106–5108.

71. Jiang, B.-P.; Guo, D.-S.; Liu, Y. *J. Org. Chem.* **2010**, *75,* 7258–7264.

List of Publications

1. Ultrasound Stimulated Nucleation and Growth of a Dye Assembly into Extended Gel Nanostructures, Malicka, J. M.; **Sandeep, A**.; Monti, F.; Bandini, E.; Gazzano, M.; Ranjith, C.; Praveen, V. K.; Ajayaghosh, A.; Armaroli, N. *Chem. −Eur. J.* **2013**, *19*, 12991–13001.

2. A carbazole–fluorene molecular hybrid for quantitative detection of TNT using a combined fluorescenceand quartz crystal microbalance method, Kartha, K, K.; **Sandeep, A**.; Vijayakumar, C. N.; Takeuchi, M.; Ajayaghosh, A. *Phys. Chem. Chem. Phys*., **2014**, *16*, 18896–18901.

3. Detection of Nitroaromatic Explosives with Fluorescent Molecular Assemblies and π-Gels, Kartha, K. K.; **Sandeep, A**.; Praveen, V. K. Ajayaghosh, A. *Chem. Rec.* **2015,** *15***,** 252–265.

4. Supercoiled fibers of self-sorted donor–acceptor stacks: a turn-off/turn-on platform for sensing volatile aromatic compounds, **Sandeep, A**.; Praveen, V. K.; Kartha, K. K.; Karunakaran, V.; Ajayaghosh, A. *Chem. Sci.*, **2016**, *7*, 4460–4467.

5. A Knockout Approach that Transforms a C_3- Symmetrical Liquid Crystal to a π-Gelator, **Sandeep, A**.; Praveen, V. K.; Shankar Rao, D. S.; Prasad, S. K.; Ajayaghosh, A. (Submitted to *Chem. Asian J.*).

List of Posters Presented in Conferences

1. **Sandeep, A.**, Ajayaghosh, A. Self-Sorted Donor- Acceptor Stacks as "Turn-on" Fluorescent Sensor for Discriminating Electron Rich and Electron Deficient Analytes. *Bilateral Indo-US Workshop on Bio-inspired Supramolecular and Polymer Assembly,* December 15-17, **2013**, Trivandrum, India.

2. **Sandeep, A.**, Ajayaghosh, A. Self-Sorted Donor-Acceptor Stacks as "Turn-on" Fluorescent Sensor for Multiple Volatile Organic Compounds. *10th JNC Research Conference on Chemistry of Materials,* October 11-13, **2014**, Trivandrum, India.